Development of Hybrid Molecular Catalysts Tethered to Functional Groups: Applications to Fuel Production

山本, 啓也

Development of Hybrid Molecular Catalysts Tethered to Functional Groups: Applications to Fuel Production

Keiya Yamamoto

March 2019

Department of Chemistry

Graduate School of Science

Kyushu University

Contents

General Introduction

Background

Before the 19th century, human societies totally depended on the annual cycle of plant photosynthesis. However, after the Industrial Revolution in the 18th and 19th centuries, energy consumption by human being significantly increased and exceeded energy supplied by natural systems. Actually, while annual energy consumption in England and Wales was 520000 MJ in the beginning of the 19th century, this value increased to 1830000 MJ in the middle of this century, where the main energy source was fossil fuels.[1] Upon now, energy demands by people have been increasing year by year with increasing the world population and advancing the science technologies. As a result, in the beginning of 21st century, worldwide primary energy consumption reached extraordinary value, 425×10^{18} J, where 86 % of this energy was made from fossil fuels.[2] Indeed, the modern society faces serious worldwide problems, such as shortage of natural resources, environmental pollution, and climate change, which are caused by the consumption of enormous amount of fossil fuels. In order to solve these serious problems, utilization of the alternative energies instead of fossil fuels has been intensively desired.

Solar light is considered as one of the most promising alternative energies because it is clean and renewable energy. In this context, artificial photosynthetic systems, which can directly convert the solar energy into solar fuels, have attracted much attention compared with photovoltaics, which can make electricity from solar light, since the storage of solar fuels is much easier than that of electricity.[2] Until now, some artificial photosynthetic systems such as solar-driven water splitting (eq. 1) and solar-driven CO_2 reduction (eq. 2) have been extensively studied by many researchers.[3,4]

$$2H_2O \xrightarrow{h\nu} O_2 + H_2 \quad (1)$$

$$CO_2 + 2H_2O \xrightarrow{h\nu} O_2 + CO, HCOOH, CH_3OH, CH_4, \text{etc.} \quad (2)$$

H_2 gas can be obtained by solar-driven water splitting (eq. 1), which is utilized for fuel cells and many industrial chemical processes. On the other hand, solar-driven CO_2 reduction (eq. 2) can contribute not only to make fuels, such as CH_3OH, CH_4, but also to decrease CO_2 emission. In order to obtain solar fuels by these two reactions, water oxidation reaction (eq. 3), which can abstract electrons from water, should be incorporated with these two reactions because both H_2 production and CO_2 reduction require electrons.

$$2H_2O \longrightarrow O_2 + 4H^+ + 4e^- \quad (3)$$

Therefore, extensive studies have been thus far carried out to develop efficient electro- and photocatalysts not only for H_2 production[5] and CO_2 reduction[6] but also for water oxidation reaction.[7]

Natural Enzymes for Water Splitting and CO_2 Reduction

In this context, researchers have paid attention to the properties of natural enzymes to obtain important insights for achieving artificial photosynthetic systems, such as water oxidation,[8] H_2 evolution,[9] conversion of CO_2 to CO.[10] In active centers of these enzymes, some transition metals actually conduct catalytic reactions, however, other functional sites surrounding active sites act as important roles for high efficiencies of enzymes. For example, [FeFe]-hydrogenase, which shows high activity for H_2 evolution and oxidation,[9a] has a sophisticated catalytic active center (see Figure 1a).[9a] In this case, the pendant amine (see Figure 1a red circle) group is well known to serve as both a proton reservoir and donor site, and the presence of this functional group relates drastically the much high catalytic performance of [FeFe]-hydrogenase.[9a] Moreover, a cuboidal [4Fe-4S] cluster (see Figure 1a green circle) locates very close to the [2Fe] core enabling effective electron transfer to the [2Fe] core.

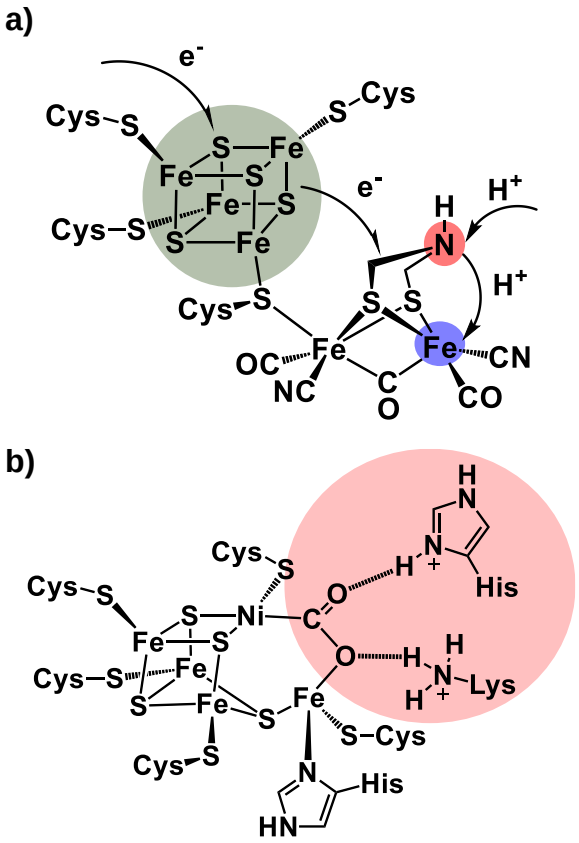

Figure 1. Structures of catalytic active centers of a) [FeFe]-hydrogenase and b) CO_2-bound CO-dehydrogenase.

On the other hand, CO-dehydrogenase converting reversibly CO_2 to CO also has an unique feature.[10] In this case, protonated histidine and protonated lysine residues, which locate very close to the [NiFe] center, are known to form hydrogen-bonds with the CO_2-bound [NiFe] center (see Figure 1b red circle), and the formation of hydrogen bonds with these functional groups effectively stabilizes the intermediate leading to achieve highly efficient reversible conversion of CO_2 to CO.[10a]

Hybrid Molecular Catalysts for Artificial Photosynthesis

In the area of artificial photosynthesis, studies on the functional groups, such as an electron relay (**ER**),[11,12] a proton relay,[13,14] and a co-catalyst,[15] which assist the catalytic reaction driven by the molecular catalysts have been thus far carried out. On the other hand, many efforts have been thus far made to develop *hybrid* molecular catalysts having covalently linked functional groups aiming for achieving highly efficient catalytic reactions comparable to the natural enzymes.[16-20] In these systems, suitable functional residues can be fixed onto suitable positions for the substrate binding sites like catalytic active sites in natural enzymes. For example, hydrogen evolving molecular catalysts having a covalently linked photosensitizing unit as a functional group have been paid attention as hybrid molecular catalysts (i.e., photo-hydrogen-evolving molecular devices; **PHEMD**s).[16a-e] The first example of such **PHEMD**s consists of the $Ru(bpy)_3^{2+}$ (bpy = 2,2'-bipyridine) derivative as a photosensitizing unit and $Pt(bpy)Cl_2$ derivative as an H_2 evolution catalyst unit (**[Ru-Pt]$^{2+}$** in Figure 2a), and can promote H_2 evolution from water in the presence of sacrificial electron donor (**SE**) upon visible light irradiation(see Figure 2b).[16a] In this system, intramolecular electron transfer from the $Ru(bpy)_3^{2+}$ derivative unit to the $Pt(bpy)Cl_2$ derivative unit is considered to be trigger for photochemical H_2 evolution. Later studies revealed that $Pt(tpy)Cl^+$ (tpy = 2,2':6',2''-terpyridine) derivatives also serve as **PHEMD**s even though these compounds do not have a covalently linked photosensitizing unit. In these systems, $Pt(tpy)Cl^+$ core can serve as both a photosensitizing unit and a catalyst unit, therefore, photochemical H_2 evolution occurs only in the presence of **SE** upon visible light irradiation.[16f-i] In the research area of CO_2 reduction, similar single-molecular catalytic systems have been developed by some researchers (e.g., **[Ru_Re]$^{2+}$** in Figure 2c).[19a-c]

On the other hand, the other example of hybrid molecular catalysts is hydrogen evolving molecular catalysts having a proton relay site.[16j-l] One of the most famous such hybrid molecular catalysts is a Ni complex H_2 evolution electrocatalyst having two pendant amine sites close to the Ni atom mimicking the catalytic center of [FeFe]-hydrogenase as mentioned above (e.g., **[Ni(P_2N_2)$_2$]$^{2+}$** in Figure 2d).[16j] Due to the presence of these functional groups at the suitable positon, this Ni complex shows extremely higher catalytic performance compared to the other molecular electrocatalysts without having pendant amine groups. Similarly, catalytic activity for CO_2 reduction molecular catalyst is reported to be largely enhanced by introducing the functional groups having a dissociated proton such as hydroxyl group (e.g., **Fe-(OH)$_8$** in Figure 2e), which form hydrogen bonds with CO_2 molecule as mentioned above (see Figure 2e).[19d-f] These studies well demonstrate that introduction of functional groups at the suitable position is an effective method to improve the catalytic performance of the

molecular catalysts, and thus many hybrid molecular catalysts having various kinds of functional groups have been thus far synthesized to achieve efficient artificial photosynthesis.

In this context, many interesting functions have been recently reported about metal complexes introduced cationic functional moieties.[17,20] Some studies focus on introduction of organic cationic **ER**s, such as methylviologen (MV^{2+} in Figure 3a),[17] which play important roles in the photochemical H_2-evolving system mentioned in the latter part.[12] In these studies, it was reported that metal complexes having MV^{2+} moieties as electron acceptor sites can intramolecularly conduct photo-driven electron transfer processes involving H_2 evolution and show some unique functions, such as multi-electron storage within single molecular architecture.[17] On the other hand, some studies introduced organic cationic co-catalysts such as 1-ethyl-3-methylimidazolium ($[EMIM]^+$ in Figure 7a),[20] which enhance catalytic efficiency of electrocatalytic CO_2 reduction catalyzed by metal electrodes.[15] In these studies, introduction of organic cation sites results in enhancement of catalytic activity due to stabilization of CO_2-bound intermediates by intramolecular interactions.[20] In the latter parts, details of these studies are mentioned.

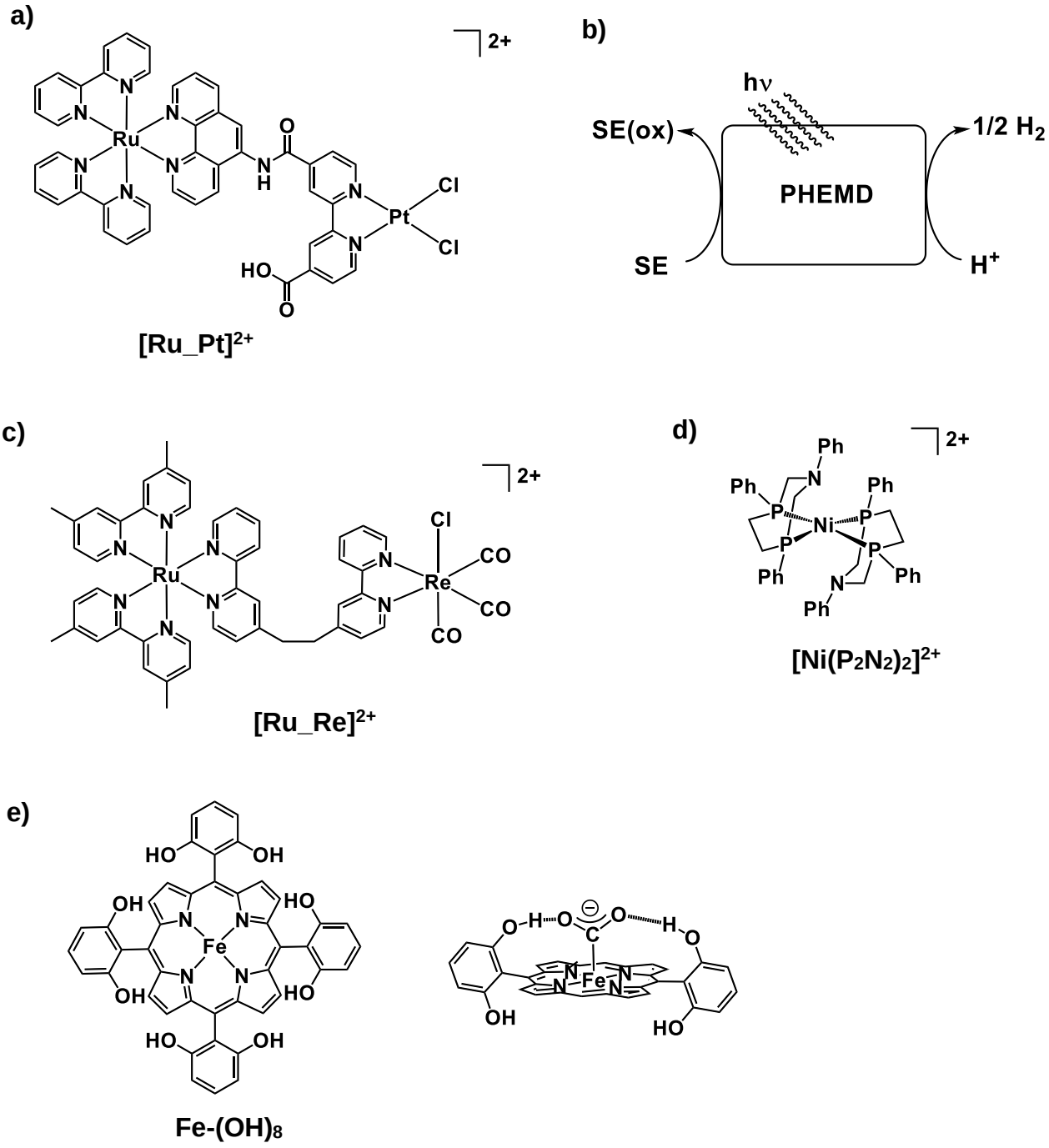

Figure 2. a) Molecular structure of **[Ru_Pt]**$^{2+}$. b) The reaction scheme of photochemical H_2 evolution using **PHEMD**s. c) Molecular structure of **[Ru_Re]**$^{2+}$. d) Molecular structure of **[Ni(P$_2$N$_2$)$_2$]**$^{2+}$. e) Molecular structure of **Fe-(OH)$_8$** and schematic representation for intramolecular charge interactions in CO_2-bound **Fe-(OH)$_8$**. Two 2',6'-dihydroxyphenyl groups are omitted for clarity.

Metal Complexes Linked with Methylviologen Moieties for H_2 evolution

Since a pioneering study on the utilization of MV^{2+} (see Figure 3a) as an **ER** was reported by Grätzel et al. in 1978,[12a] various kinds of organic molecules have been thus far employed as **ER**s for H_2 evolution reaction.[12] For example, some MV^{2+} derivatives shown in Figure 3a have been used as **ER**s in a well-known photochemical H_2 evolution system consisting of $[Ru(bpy)_3]^{2+}$, **ER**, and H_2 evolving catalyst (Figure 3b). In this photosystem, oxidative quenching of the photoexcited $[Ru(bpy)_3]^{2+}$ by **ER** results in the formation of one-electron oxidized species of $[Ru(bpy)_3]^{2+}$ ($[Ru(bpy)_3]^{3+}$) and a radical species of **ER** (**ER**$^{-\bullet}$). Then, H_2 evolution reaction is promoted by a catalyst in the presence of **ER**$^{-\bullet}$, and $[Ru(bpy)_3]^{3+}$ is reduced by **SE** yielding the original species ($[Ru(bpy)_3]^{2+}$). After the first report of MV^{2+} by Grätzel, Amouyal et al. employed an organic **ER** (e.g., DQ^{2+} in Figure 3a) showing the first reduction potential much more negative (-0.70 V vs. NHE) compared to that of MV^{2+} (-0.44 V vs. NHE) in above mentioned photochemical H_2 evolution system.[12c,d] Sakai et al. reported that catalytic rate of photochemical H_2 evolution promoted by a Co complex is drastically improved by using DQ^{2+} instead of MV^{2+}.[21] This result is reasonably understood that catalytic activity increases as increasing the driving force for H_2 evolution, which is determined by the potential difference between the first reduction potential of **ER** and the standard water reduction potential. Recently, He, et al. reported a novel organic **ER** (S-BnV^{2+} in Figure 3a) for H_2 evolution reaction. S-BnV^{2+} is reported to act as both a photosensitizer and a ER, therefore, upon visible light irradiation, H_2 evolution reaction proceeds even in the absence of a photosensitizer in a photochemical H_2 evolution system.[12e]

a)

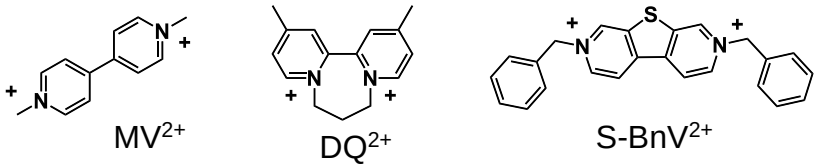

b)

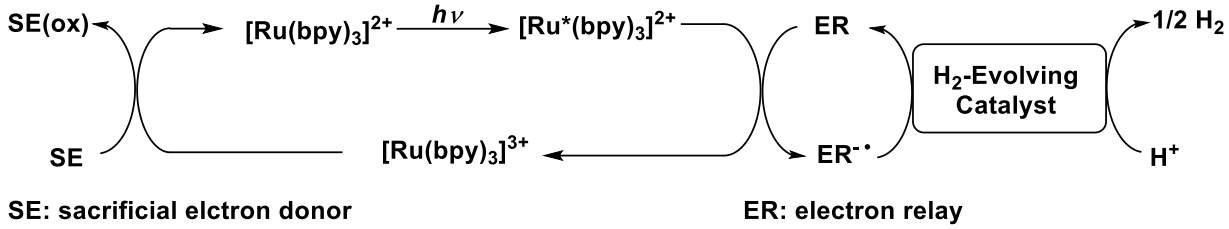

Figure 3. a) Structures of some selected **ER**s. b) The reaction scheme of photochemical H_2 evolution with **ER**s.

On the other hand, efforts have been made to develop $Ru(bpy)_3^{2+}$ derivatives having a covalently linked MV^{2+} unit because effective intramolecular electron transfer from the $Ru(bpy)_3^{2+}$ unit to the MV^{2+} unit is expected to improve the catalytic performance for photochemical H_2 evolution reaction (see Figure 4a). In this context, Okura, et al., synthesized a $Ru(bpy)_3^{2+}$ derivative having a single MV^{2+} moiety (**$[Ru(bpy)_2(bpyMV1)]^{4+}$** in Figure 4b), and demonstrated that photocatalytic H_2 evolution proceeds using this compound as both a photosensitizer and an **ER** in the presence of **SE** and hydrogenase.[17a] Sakai et al. synthesized $Ru(bpy)_3^{2+}$ derivatives having covalently linked multiple MV^{2+} units (e.g., **$[Ru(bpy)_2(5,5'\text{-}aspMV4)]^{10+}$** in Figure 4b), and demonstrated that photocatalytic H_2 evolution proceeds using this compound as both a photosensitizer and an **ER** in the presence of EDTA (ethylenediaminetetraacetic acid disodium salt) as **SE** and a Pt complex H_2 evolving molecular catalyst.[17b] On the other hand, Sakai et al. also reported that $Ru(bpy)_3^{2+}$ derivatives having covalently linked multiple MV^{2+} units (e.g., **$[Ru(4,4'\text{-}aspMV4)_3]^{26+}$** in Figure 5) show multi-electron storage behavior within a single molecule as photo-charge-separators (**PCS**s) in the presence of EDTA.[17c,d] In this system, upon visible light irradiation, consecutive multi-electron transfer from the $Ru(bpy)_3^{2+}$ chromophore to the MV^{2+} unit occurs, leading to the storage of ca. 7 electrons within a single molecule (see Figure 5). Importantly, almost all the reduced MV^{2+} radicals ($MV^{+\bullet}$) form diamagnetic π-dimers $(MV^+)_2$. This behavior, single-pigment driven multi-electron transfer and storage, finely mimics the electron storage system in the light dependent reaction of natural photosynthesis.[22] Furthermore, catalytic performance for H_2 evolution is also evaluated using **$[Ru(4,4'\text{-}aspMV4)_3]^{26+}$** as both a photosensitizer and an **ER** in the presence of EDTA and colloidal Pt as a catalyst.[17c,d]

a)

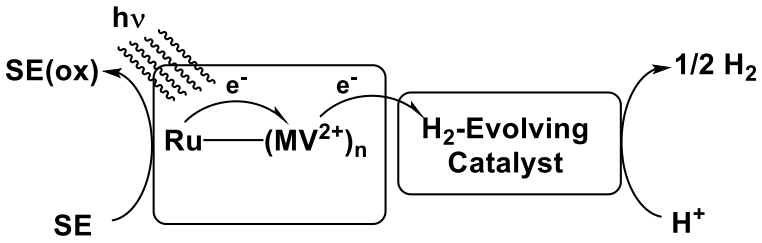

b)

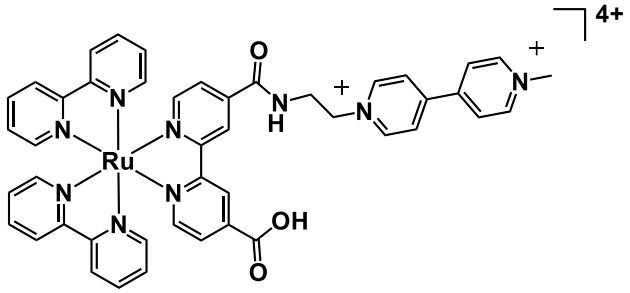

[Ru(bpy)$_2$(bpyMV1)]$^{4+}$

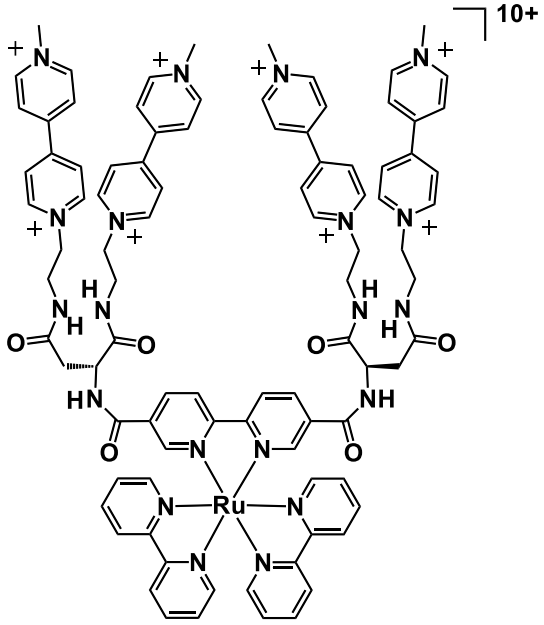

[Ru(bpy)$_2$(5,5'-aspMV4)]$^{10+}$

Figure 4. a) The reaction scheme of photochemical H_2 evolution using $Ru(bpy)_3^{2+}$ derivatives covalently linked with MV^{2+} moieties. b) Molecular structures of **[Ru(bpy)$_2$(bpyMV1)]$^{4+}$** and **[Ru(bpy)$_2$(5,5'-aspMV4)]$^{10+}$**.

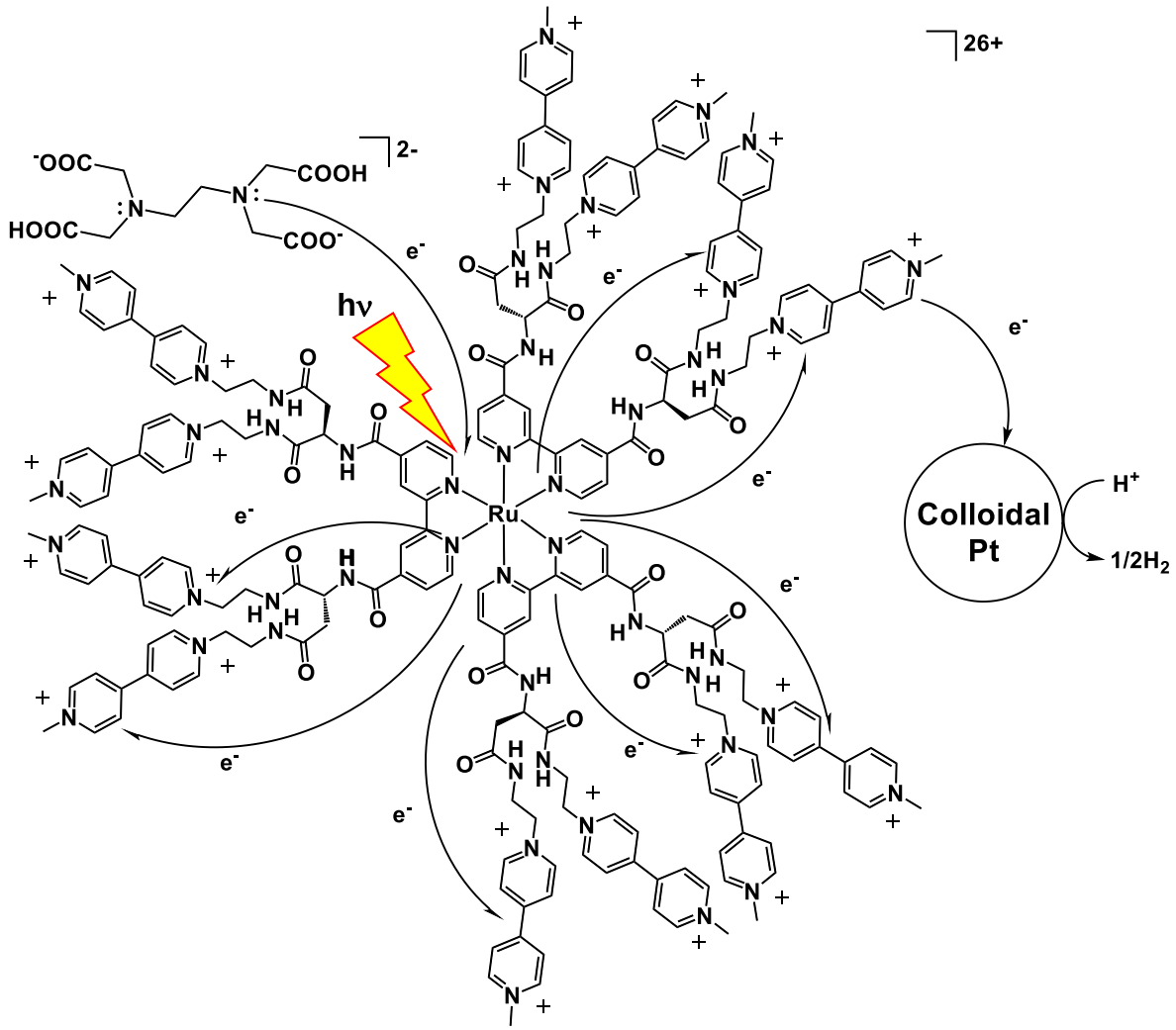

Figure 5. Molecular structure of **[Ru(4,4'-aspMV4)$_3$]$^{26+}$** and schematic representation for photo-driven multi-electron storage leading to H_2 evolution.

On the other hand, mononuclear Pt complexes having covalently linked MV^{2+} units also show a very unique feature when they are utilized as **PHEMD**s.[17e,f,g] For example, Pt(bpy)Cl_2-derivatves having covalently linked multiple MV^{2+} units (e.g., **[Pt(4,4'-aspMV4)Cl_2]$^{8+}$** in Figure 6) showing the electron storage capability can promote photocatalytic H_2 evolution only in the presence of EDTA although structural analogue compounds showing no electron storage capability, such as Pt(dcbpy)Cl_2 (dcpby = 4,4'-dicarboxy-2,2'-bipyridine), cannot promote H_2 evolution under the same conditions.[17e] In addition, catalytic activity of Pt(tpy)Cl-based PHEMD is drastically enhanced by introducing the MV^{2+} residue as an electron reservoir site (e.g., **[Pt(L-C1-MV1)Cl]$^{4+}$** in Figure 6).[17g] These results clearly indicate that electron storage capability largely contributes to enhance the catalytic performance of Pt-based **PHEMD**s.

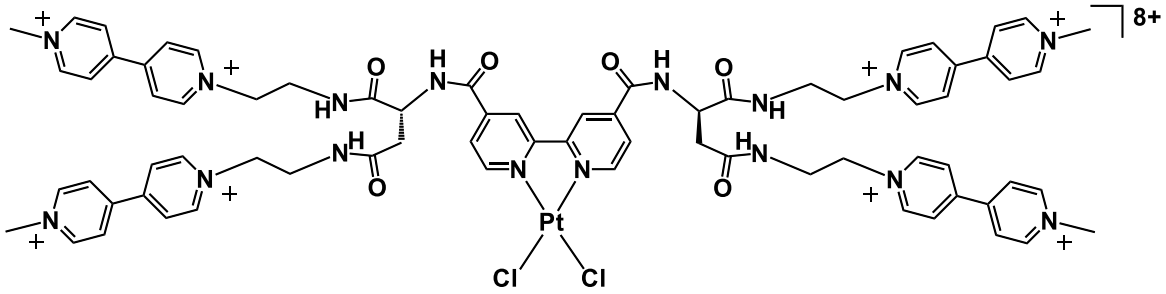

[Pt(4,4'-aspMV4)Cl$_2$]$^{8+}$

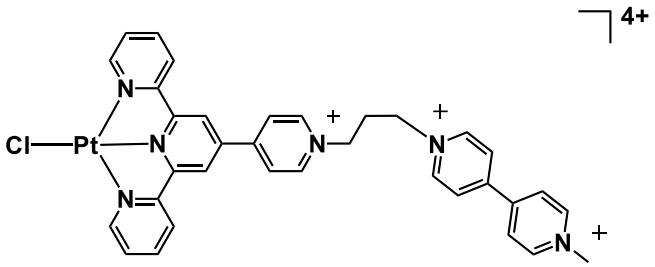

[Pt(L-C1-MV1)Cl]$^{4+}$

Figure 6. Molecular structures of **[Pt(4,4'-aspMV4)Cl$_2$]$^{8+}$** and **[Pt(L-C1-MV1)Cl]$^{4+}$**.

Metal Complexes Linked with Organic Cations for CO_2 Reduction

The pioneering study on organic cations as co-catalysts for CO_2 reduction was reported by Masel et al. in 2011.[15a] In the study, an imidazolium-based ionic liquid [EMIM][BF_4] (see Figure 7a) is employed as a co-catalyst for electrochemical CO_2 reduction by an Ag electrode in an aqueous electrolyte solution, and is found to lower the overpotential for CO_2 reduction and to improve the selectivity for CO production versus H_2 production. On the other hand, the other ionic liquids, such as ammonium cations (e.g., 1-hexyl-1,4-diazabicyclo[2.2.2]octanium bis(trifluoromethane)sulfonimide: [C_6DABCO][TFSI] and tetrabutylammonium tetrafluoroborate: [n-Bu_4N][BF_4] in Figure 7a), are also reported to enhance the catalytic activity of an Ag electrode for CO_2 reduction.[15d] The detailed mechanism of CO_2 reduction in the presence of these ionic liquid co-catalysts still remains unclear, however, these ionic liquid co-catalysts are considered to stabilize the one-electron-reduced species of CO_2 (i.e., $CO_2^{-\bullet}$) at the surface of the Ag electrode. In addition to these studies, $[EMIM]^+$ has been applied for homogeneous electrocatalytic systems for CO_2 reduction using *fac*-ReCl(bpy)$(CO)_3$.[15e,f] In this case, the overpotential also decreases by adding $[EMIM]^+$ into the system, clearly indicating that an ionic liquid can also serve as a co-catalyst for CO_2 reduction catalyzed by molecular catalysts. The role of ionic liquids in this system is considered as the stabilization CO_2-bound catalyst by hydrogen bonds during the catalytic reaction (see Figure 7b). [15f]

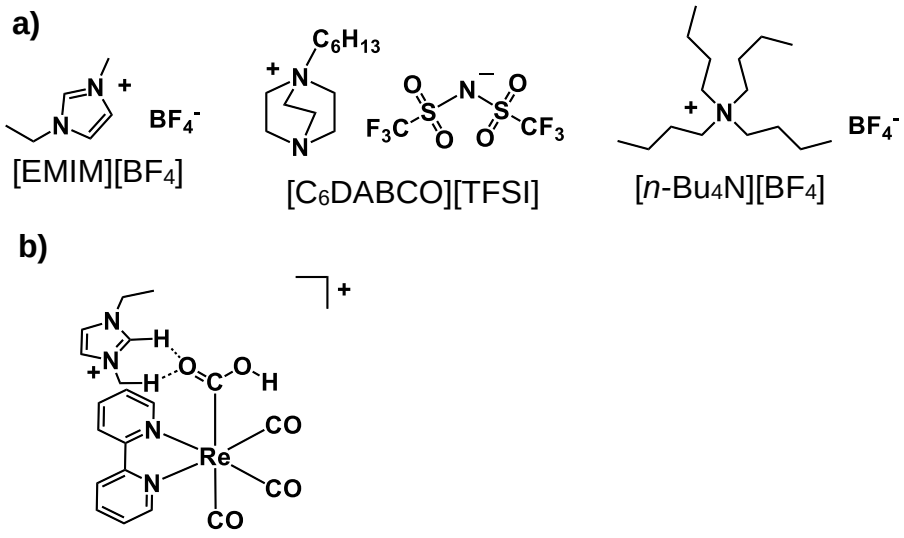

Figure 7. a) Molecular structures of ionic liquids acting as a co-catalyst for CO_2 reduction. b) a proposed structure of the adduct of the CO_2-bound *fac*-ReCl(bpy)$(CO)_3$ with an $[EMIM]^+$ molecule.

Inspired by these results, some researchers made efforts to develop metal complexes covalently linked with organic co-catalysts.[20] Savéant et al. reported that a Fe porphyrin molecular catalyst having ammonium moieties located close to the CO_2-binding site (**$[Fe\text{-}TMA]^{4+}$** in Figure 8a) shows much lower overpotential and higher turnover frequency (TOF) for electochemical CO_2 reduction into CO than those of other reported molecular catalysts.[20a] The enhanced catalytic performance of

[Fe-TMA]$^{4+}$ is considered to be attributable to the stabilization of CO_2-bound Fe species due to the interaction of negatively charged O atoms of CO_2 and positively charged N atoms of trimethyl ammonium units (see Figure 8b). On the other hand, Nippe et al. also reported that a *fac*-ReCl(bpy)$(CO)_3$-based molecular catalyst having a covalently linked imidazolium moiety (**[Re_Im]$^+$** in Figure 8a) shows higher TOF for electrochemical CO_2 reduction into CO compared to that for the non-functionalized *fac*-ReCl(bpy)$(CO)_3$ molecular catalyst.[20b] Moreover, Aukauloo et al. reported that a Fe porphyrin electrocatalyst having imidazolium sites (**[Fe_Im]$^{4+}$** in Figure 8a) shows lower onset overpotential for CO_2 reduction into CO.[20c] These studies actually demonstrate well the effectiveness of introduction of functional cationic sites to improve the catalytic performance of CO_2 reduction molecular catalysts, however, the detailed role of functional cationic sites in the catalytic cycle still remains unclear.

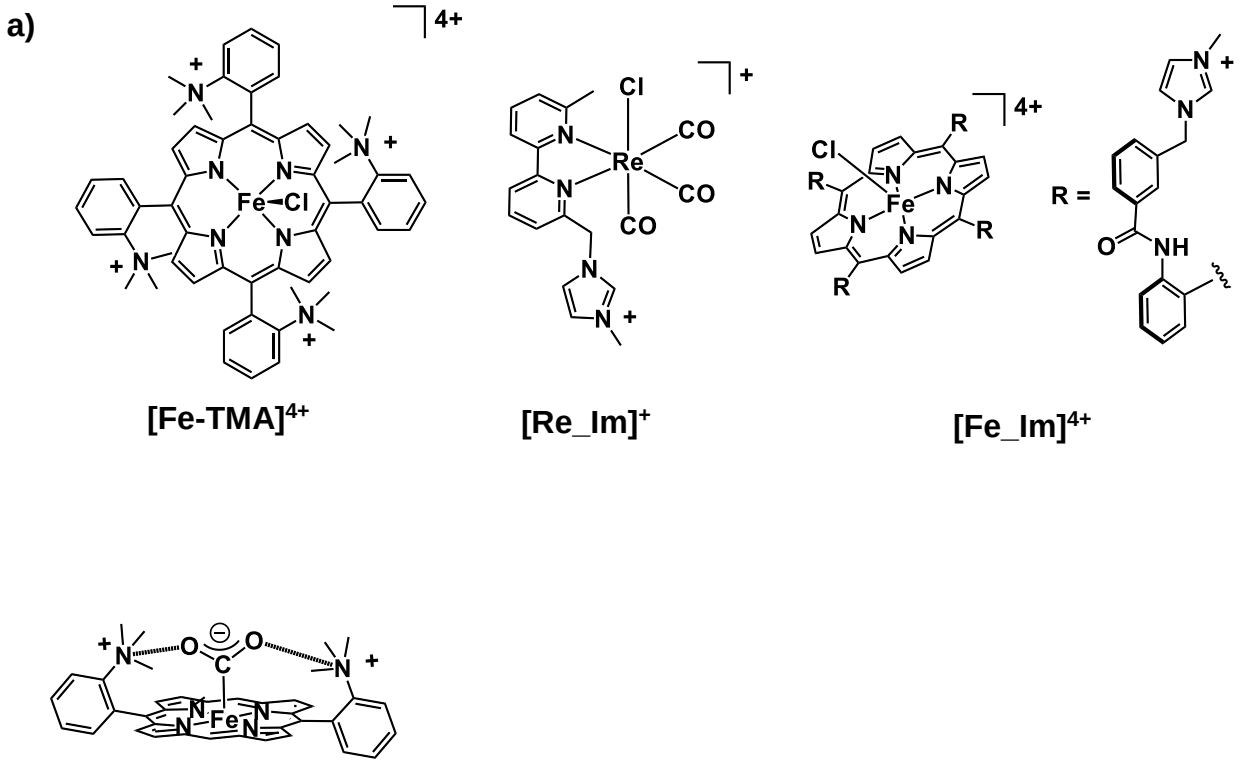

Figure 8. a) Structures of metal complexes having functional cationic moieties. b) Schematic representation for intramolecular charge interactions in CO_2-bound **[Fe-TMA]$^{4+}$**. Two *o*-N,N,N-trimethylaniliniumphenyl groups are omitted for clarity.

Survey of This Thesis

As mentioned above, development of molecular catalysts having covalently linked functional moieties, such as electron reservoir sites and imidazolium units, is considered to be one of the most effective methodologies to achieve the sophisticated catalytic systems similar to the catalytic centers in natural enzymes. Nevertheless, detailed studies on the effects of these functional moieties on the catalytic performance of molecular catalysts have not been carried out even though such studies provide many important insights into the molecular design for achieving sophisticated catalytic systems. In this regards, this thesis focuses on clarification of the detailed effects of position of electron reservoir sites on the photocatalytic H_2 evolution performance of $Pt(bpy)Cl_2$ molecular catalysts (Chapter 1), and those on the multi-electron storage behavior of $Ru(bpy)_3^{2+}$ derivatives (Chapter 2). Moreover, the detailed effects of introduction of imidazolium units on the catalytic activity for CO_2 reduction of a Ru complex (Chapter 3) have been investigated.

Chapter 1 describes catalytic properties of a newly synthesized Pt(bpy)Cl_2-based **PHEMD**, **[$PtCl_2$(bpyMV2)]$^{4+}$** (see Figure 9). Importantly, MV^{2+} moieties locate closer to the Pt complex site in the present study than previous **PHEMD**s (e.g., **[Pt(4,4'-aspMV4)Cl_2]$^{8+}$** in Figure 9). This study revealed that **[$PtCl_2$(bpyMV2)]$^{4+}$** shows catalytic activity for photochemical H_2 evolution in the presence of EDTA as a sacrificial electron donor and H_2 evolution of this system proceeds via formation of triply-reduced species. This behavior is in sharp contrast to those of the previous systems, where doubly-reduced species promotes H_2 evolution. This study clearly showed that catalytic behavior of Pt-based **PHEMD**s having MV^{2+} moieties can be finely controlled by changing the distance between a Pt complex site and MV^{2+} sites (see Figure 9).

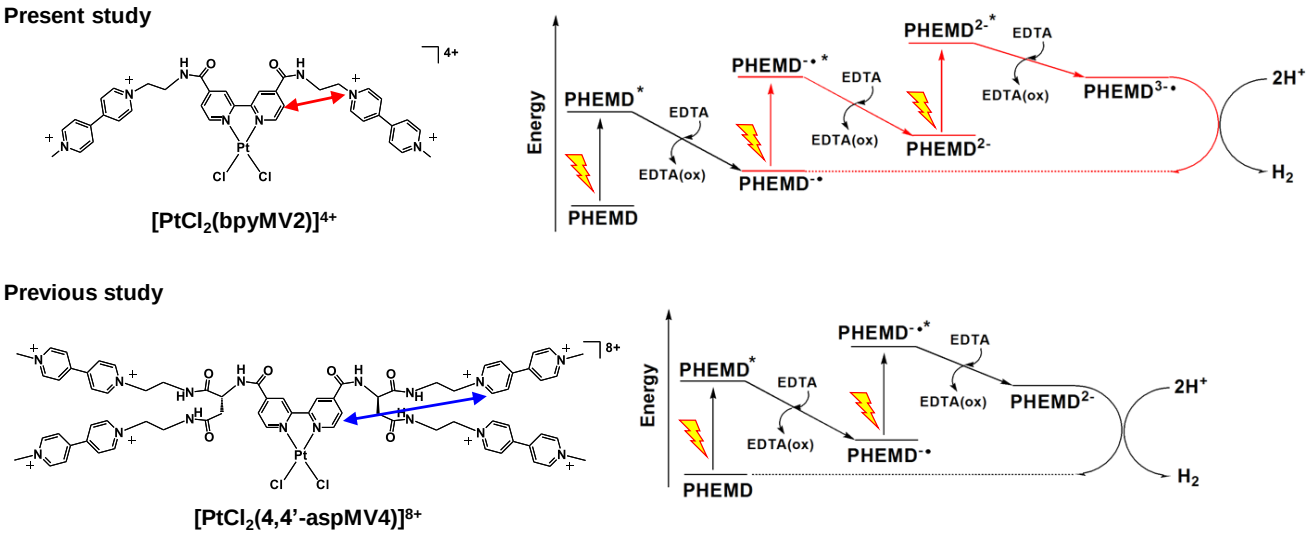

Figure 9. Molecular structures and schemes for photochemical H_2 evolution of (top) **[$PtCl_2$(bpyMV2)]$^{4+}$** and (bottom) **[$PtCl_2$(4,4'-aspMV4)]$^{8+}$**.

Chapter 2 describes the synthesis of a new Ru complex, **[Ru(bpyMV2)$_3$]$^{14+}$** (see Figure 10), with the **[bpyMV2]$^{4+}$** ligand used in Chapter 1 and its application for photo-driven multi-electron storage as a **PCS**. Compared to a reported **PCS [Ru(4,4'-aspMV4)$_3$]$^{26+}$** having twelve MV^{2+} moieties (see Figure 5), **[Ru(bpyMV2)$_3$]$^{14+}$** has six MV^{2+} sites locating closer to the $Ru(bpy)_3^{2+}$ site. This study found that photoirradiation in the presence of sacrificial electron donor allows **[Ru(bpyMV2)$_3$]$^{14+}$** to conduct consecutive photochemical steps consisting of photoexcitation of the Ru site, intramolecular electron transfer to MV^{2+} sites, and reduction by sacrificial electron donor, resulting in storage of ca. 3 electrons within the molecular structure (see Figure 10). Importantly, **[Ru(bpyMV2)$_3$]$^{14+}$** shows relatively preferential formation of $MV^{+\bullet}$ compared to $(MV^+)_2$ in the steady state while almost all the electrons are stored in the form of $(MV^+)_2$ in the **[Ru(4,4'-aspMV4)$_3$]$^{26+}$** system. Because $MV^{+\bullet}$ has higher driving force for H_2 evolution than that of $(MV^+)_2$, **[Ru(bpyMV2)$_3$]$^{14+}$** can promote photochemical H_2 evolution with higher efficiency in the presence of colloidal Pt as a catalyst compared to **[Ru(4,4'-aspMV4)$_3$]$^{26+}$**. As a result, this study succeeded in control of properties of **PCS**s by tuning molecular structures and development of the more efficient catalytic system than reported systems.

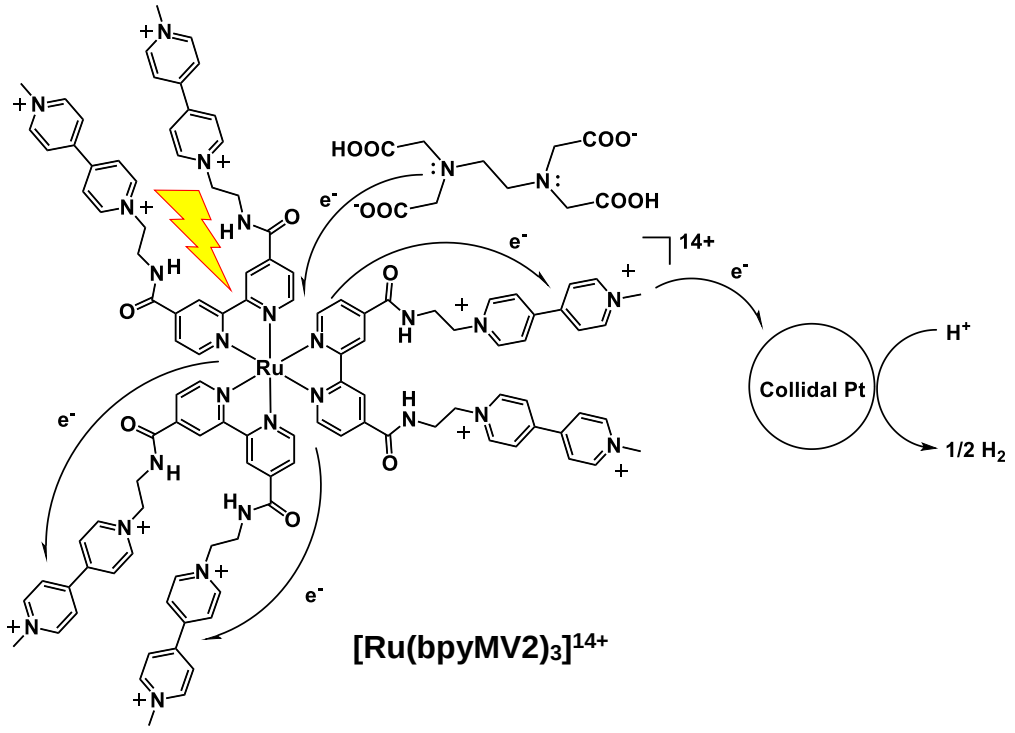

Figure 10. Molecular structure of **[Ru(bpyMV2)$_3$]$^{14+}$** and schematic representation of photochemical H_2 evolution promoted by **[Ru(bpyMV2)$_3$]$^{14+}$.**

Chapter 3 describes some unique properties of introduction of **Im** moieties into the Ru complex architecture revealed by investigation of electrochemical CO_2 reduction catalyzed by a new Ru complex having **Im** moieties, **[Ru_Im]**$^{3+}$ (see Figure 11). In this study, it was found that **Im** moieties strongly stabilize π^* orbital of the bpy site due to their electron-withdrawing effects. Furthermore, the introduction of **Im** moieties leads to the difference of solvent effects on catalytic activity from the non-functionalized Ru complex (**[Ru_Me]**$^{+}$ in Figure 11); catalytic activity of **[Ru_Im]**$^{3+}$ depends on Lewis basicity of the solvent, while **[Ru_Me]**$^{+}$ shows its catalytic activity is influenced by Lewis acidity of the solvent.

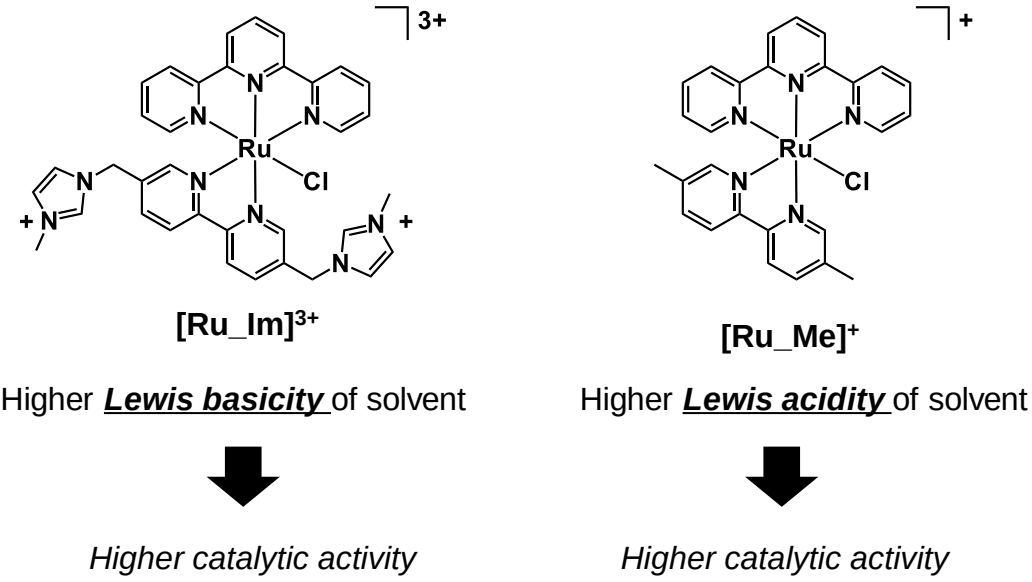

Figure 11. Molecular structures of **[Ru_Im]**$^{3+}$ and **[Ru_Me]**$^{+}$**.**

References

1. E. A. Wrigley, Energy and the English Industrial Revolution, *Phil. Trans. R. Soc. A.*, 2013, **371**.
2. N. S. Lewis, D. G. Nocera, *Proc. Natl. Acad. Sci. U. S. A.*, 2006, **103**, 15729.
3. (a) A. J. Esswein and D. G. Nocera, *Chem. Rev.*, 2007, **107**, 4022.
   (b) K. J. Young, L. A. Martini, R. L. Milot, R. C. Snoeberger III, V. S. Batista, C. A. Schmuttenmaer, R. H. Crabtree and G. W. Brudvig, *Coord. Chem. Rev.*, 2012, **256**, 2503.
4. A. M. Appel, J. E. Bercaw, A. B. Bocarsly, H. Dobbek, D. L. DuBois, M. Dupuis, J. G. Ferry, E. Fujita, R. Hille, P. J. A. Kenis, C. A. Kerfeld, R. H. Morris, C. H. F. Peden, A. R. Portis, S. W. Ragsdale, T. B. Rauchfuss, J. N. H. Reek, L. C. Seefeldt, R. K. Thauer and G. L. Waldrop, *Chem. Rev.*, 2013, **113**, 6621.
5. (a) S. Fukuzumi, Y. Yamada, T. Suenobu, K. Ohkubo and Hiroaki Kotani, *Energy Environ. Sci.*, 2011, **4**, 2754.
   (b) J. R. McKone, S. C. Marinescu, B. S. Brunschwig, J. R. Winkler and H. B. Gray, *Chem. Sci.*, 2014, **5**, 865.
6. (a) J. Qiao, Y. Liu, Feng Hong and J. Zhang, *Chem. Soc. Rev.*, 2014, **43**, 631.
   (b) K. Li, B. Peng and T. Peng, *ACS Catal.*, 2016, **6**, 7485.
7. (a) J. D. Blakemore, R. H. Crabtree and G. W. Brudvig, *Chem. Rev.*, 2015, **115**, 12974.
   (b) B. M. Hunter, H. B. Gray and A. M. Müller, *Chem. Rev.*, 2016, **116**, 14120.
8. D. A. Pantazis, *ACS Catal.*, 2018, **8**, 9477.
9. (a) W. Lubitz, H. Ogata, O. Rüdiger and E. Reijerse, *Chem. Rev.*, 2014, **114**, 4081.
   (b) H. Ogata, K. Nishikawa and W. Lubitz, *Nature*, 2015, **520**, 571.
   (c) F. Wittkamp, M. Senger, S. T. Stripp and U.-P. Apfel, *Chem. Commun.*, 2018, **54**, 5934.
10. (a) J.-H. Jeoung and H. Dobbek, *Science*, 2007, **318**, 1461.
    (b) M. Can, F. A. Armstrong and S. W. Ragsdale, *Chem. Rev.*, 2014, **114**, 4149.
11. (a) B. Rausch, M. D. Symes, G. Chisholm and L. Cronin, *Science*, 2014, **345**, 1326.
    (b) N. Kirkaldy, G. Chisholm, J.-J. Chen and L. Cronin, *Chem. Sci.*, 2018, **9**, 1621.
12. (a) K. Kalyanasundaram, J. Kiwi, M. Grätzel, *Helv. Chim. Acta*, 1978, **61**, 2720.
    (b) R. Bauer and H. A. F. Werner, *Acta Chem. Scand.*, 1991, **45**, 669.
    (c) P. Keller, A. Moradpour, E. Amouyal and H. Kagan, *J. Mol. Catal.*, 1980, **7**, 539.
    (d) E. Amouyal, B. Zidler, P. Keller and A. Moradpour, *Chem. Phys. Lett.*, 1980, **74**, 314.
    (e) G. Li, L. Xu, W. Zhang, K. Zhou, Y. Ding, F. Liu, X. He and G. He, *Angew. Chem. Int. Ed.*, 2018, **57**, 4897.

13. Y. Choi, H. Kim, G. Moon, S. Jo and W. Choi, *ACS Catal.*, 2016, **6**, 821.
14. G. Liu, T. Wang, H. Zhang, X. Meng, D. Hao, K. Chang, P. Li, T. Kako and J. Ye, *Angew. Chem. Int. Ed.*, 2015, **54**, 13561.
15. (a) B. A. Rosen, A. Salehi-Khojin, M. R. Thorson, W. Zhu, D. T. Whipple, P. J. A. Kenis and R. I. Masel, *Science*, 2011, **334**, 643.
(b) E. E. L. Tanner, C. Batchelor-McAuley and R. G. Compton, *J. Phys. Chem. C*, 2016, **120**, 26442.
(c) G. P. S. Lau, M. Schreier, D. Vasilyev, R. Scopelliti, M. Grätzel and P. J. Dyson, *J. Am. Chem. Soc.*, 2016, **138**, 7820.
(d) S.-F. Zhao, M. Horne, A. M. Bond and J. Zhang, *J. Phys. Chem. C*, 2016, **120**, 23989.
(e) D. C. Grills, Y. Matsubara, Y. Kuwahara, S. R. Golisz, D. A. Kurtz and B. A. Mello, *J. Phys. Chem. Lett.*, 2014, **5**, 2033.
(f) Y. Matsubara, D. C. Grills and Y. Kuwahara, *ACS Catal.*, 2015, **5**, 6440.
16. (a) H. Ozawa, M. Haga and K. Sakai, *J. Am. Chem. Soc.*, 2006, **128**, 4926.
(b) H. Ozawa and K. Sakai, *Chem. Commun.*, 2011, **47**, 2227.
(c) P. D. Frischmann, K. Mahata and F. Würthner, *Chem. Soc. Rev.*, 2013, **42**, 1847.
(d) G. F. Manbeck and K. J. Brewer, *Coord. Chem. Rev.*, 2013, **257**, 1660.
(e) M. G. Pfeffer, T. Kowacs, M. Wächtler, J. Guthmuller, B. Dietzek, J. G. Vos and S. Rau, *Angew. Chem. Int. Ed.*, 2015, **54**, 6627.
(f) R. Okazaki, S. Masaoka and K. Sakai, *Dalton Trans.*, 2009, 6127.
(g) M. Kobayashi, S. Masaoka and K. Sakai, *Dalton Trans.*, 2012, **41**, 4903.
(h) K. Yamauchi and K. Sakai, *Dalton Trans.*, 2015, **44**, 8685.
(i) M. Kobayashi, S. Masaoka and K. Sakai, *Angew. Chem. Int. Ed.*, 2012, **51**, 7431.
(j) M. L. Helm, M. P. Stewart, R. M. Bullock, M. R. DuBois, D. L. DuBois, *Science*, 2011, **333**, 863.
(k) A. J. P. Cardenas, B. Ginovska, N. Kumar, J. Hou, S. Raugei, M. L. Helm, A. M. Appel, R. M. Bullock and M. O'Hagan, *Angew. Chem. Int. Ed.*, 2016, **55**, 13509.
(l) R. Tatematsu, T. Inomata, T. Ozawa and H. Masuda, *Angew. Chem. Int. Ed.*, 2016, **55**, 5247.
(m) H. Shao, S. K. Muduli, P. D. Tran and H. S. Soo, *Chem. Commun.*, 2016, **52**, 2948.
17. (a) T. Hiraishi, T. Kamachi and I. Okura, *J. Mol. Catal. A: Chem.*, 1999, **138**, 107.
(b) M. Ogawa, B. Balan, G. Ajayakumar, S. Masaoka, H.-B. Kraatz, M. Muramatsu, S. Ito, Y. Nagasawa, H. Miyasaka and K. Sakai, *Dalton Trans.*, 2010, **39**, 4421.

(c) K. Kitamoto, M. Ogawa, G. Ajayakumar, S. Masaoka, H.-B. Kraatz and K. Sakai, *Inorg. Chem. Front.*, 2016, **3**, 671.

(d) K. Kitamoto and K. Sakai, *Chem. Eur. J.*, 2016, **22**, 12381.

(e) K. Kitamoto and K. Sakai, *Angew. Chem. Int. Ed.*, 2014, **53**, 4618.

(f) K. Kitamoto and K. Sakai, *Chem. Commun.*, 2016, **52**, 1385.

(g) S. Lin, K. Kitamoto, H. Ozawa and K. Sakai, *Dalton Trans*., 2016, **45**, 10643.

(h) M. Miyaji, K. Kitamoto, H. Ozawa and K. Sakai, *Eur. J. Inorg. Chem.*, 2017, 1237.

18. (a) R. Matheu, M. Z. Ertem, J. Benet-Buchholz, E. Coronado, V. S. Batista, X. Sala and A. Llobet, *J. Am. Chem. Soc.*, 2015, **137**, 10786.

(b) M. Yoshida, M. Kondo, S. Torii, K. Sakai and S. Masaoka, *Angew. Chem. Int. Ed.*, 2015, **54**, 7981.

(c) T. Ghosh, P. Ghosh and G. Maayan, *ACS Catal.*, 2018, **8**, 10631.

19. (a) C. Matlachowski, B. Braun, S. Tschierlei, and M. Schwalbe, *Inorg. Chem.*, 2015, **54**, 10351.

(b) C. D. Windle, M. W. George, R. N. Perutz, P. A. Summers, X. Z. Sunb and A. C. Whitwood, *Chem. Sci.*, 2015, **6**, 6847.

(c) Y. Tamaki and O. Ishitani, *ACS Catal.*, 2017, **7**, 3394.

(d) C. Costentin, S. Drouet, M. Robert and J.-M. Savéant, *Science*, 2012, **338**, 90.

(e) A. Chapovetsky, T. H. Do, R. Haiges, M. K. Takase and S. C. Marinescu, *J. Am. Chem. Soc.*, 2016, **138**, 5765.

(f) E. M. Nichols, J. S. Derrick, S. K. Nistanaki, P. T. Smithab and C. J. Chang, *Chem. Sci.*, 2018, **9**, 2952.

(g) C. W. Machan, J. Yin, S. A. Chabolla, M. K. Gilson and C. P. Kubiak, *J. Am. Chem. Soc.*, 2016, **138**, 8184.

(h) S. Roy, B. Sharma, J. Pécaut, P. Simon, M. Fontecave, P. D. Tran, E. Derat and V. Artero, *J. Am. Chem. Soc.*, 2017, **139**, 3685.

20. (a) I. Azcarate, C. Costentin, M. Robert and J.-M. Savéant, *J. Am. Chem. Soc.*, 2016, **138**, 16639.

(b) S. Sung, D. Kumar, M. Gil-Sepulcre and M. Nippe, *J. Am. Chem. Soc.*, 2017, **139**, 13993.

(c) A. Khadhraoui, P. Gotico, B. Boitrel, W. Leibl, Z. Halime and A. Aukauloo, *Chem. Commun.*, 2018, **54**, 11630.

21. K. Kawano, K. Yamauchi and K. Sakai, *Chem. Commun.*, 2014, **50**, 9872.

22. H. Kirchhoff, S. Horstmann and E. Weis, *Biochim. Biophys. Acta*, 2000, **1459**, 148.

Chapter 1

Pt(II)-Catalyzed Photosynthesis for H_2 Evolution Cycling Between Singly and Triply Reduced Species

Introduction

Solar-driven water splitting into H_2 and O_2 has been studied intensively to solve the problems arising from global warming and shortage of fossil fuels.[1] In contrast with the great advancement made in the studies of purely inorganic substances,[2] the studies on molecular systems still require substantial advancement in order to meet the criteria required for the practical applications.[3,4] In this context, Sakai group has been interested in the study of Pt(II)-based molecular H_2-evolving catalysts over the past years,[5] including those functionalized with light-harvesting chromophores, which are called 'photo-hydrogen-evolving molecular devices' (**PHEMDs**). The **PHEMDs** can be either photosensitizer-catalyst dyads consisting of a $Ru(bpy)_3^{2+}$-derived chromophore and a Pt(II)-based H_2-evolving catalyst or even simpler mononuclear Pt(II) complexes that possess both of these functionalities.[6] Examples of the latter Pt(II)-only systems include $\mathbf{PV^{2+}}$ and $\mathbf{[PtCl_2(5,5'\text{-}MV4)]^{8+}}$ depicted in Figure 1a. These Pt(II)-only single-component photocatalysts evolve H_2 in the presence of a sacrificial electron donor (EDTA; ethylenediaminetetraacetic acid disodium salt) via two consecutive photo-driven electron transfer steps (Z-scheme photosynthesis) leading to the formation of a two-electron-reduced species ($\mathbf{PHEMD^{2-}}$) which can thermally drive H_2 evolution from water (see Figure 1b).[7] In these studies, a singly reduced species ($\mathbf{PHEMD^{-\bullet}}$) is first generated via reductive quenching of the photoexcited state (**PHEMD***) by EDTA, followed by photoexcitation of $\mathbf{PHEMD^{-\bullet}}$ leading to a second reduction via the reaction: $\mathbf{PHEMD^{-\bullet *}}$ + EDTA → $\mathbf{PHEMD^{2-}}$ + EDTA(ox), where the asterisked species corresponds to its photoexcited state. An important feature is that the one-electron-reduced species cannot thermally drive H_2 evolution from water.[7a] Thus, H_2 is generated via photochemical activation of the one-electron-reduced species.

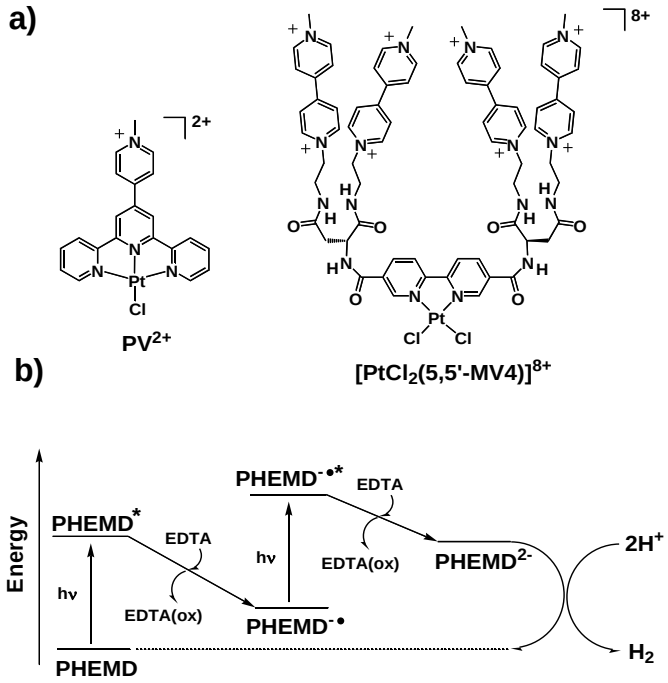

Figure 1. a) Examples of **PHEMDs.** b) Z-scheme photosynthesis by a **PHEMD**.

This chapter focuses on a new $PtCl_2$(bpy) derivative (bpy = 2,2'-bipyridine) tethered to two pendant viologen units, **[PtCl₂(bpyMV2)]⁴⁺** in Figure 2a. This system is found to drive photochemical H_2 evolution only via formation of three-electron-reduced species as illustrated in Figures 2b,3. Importantly, this molecular system does not consume the initially collected one electron when it photocatalyzes H_2 evolution from water. Thermal paths **HER(1)** and **HER(2)** do not take place, while either path **HER(3)** or **HER(4)** may take place. Thus it is shown that a reducing equivalent stored over the bpy ligand is important to drive water reduction to H_2. In other words, the photocatalytic H_2 evolution cycle can be 'switched on' only after filling both the pendant viologen acceptors with a reducing equivalent.

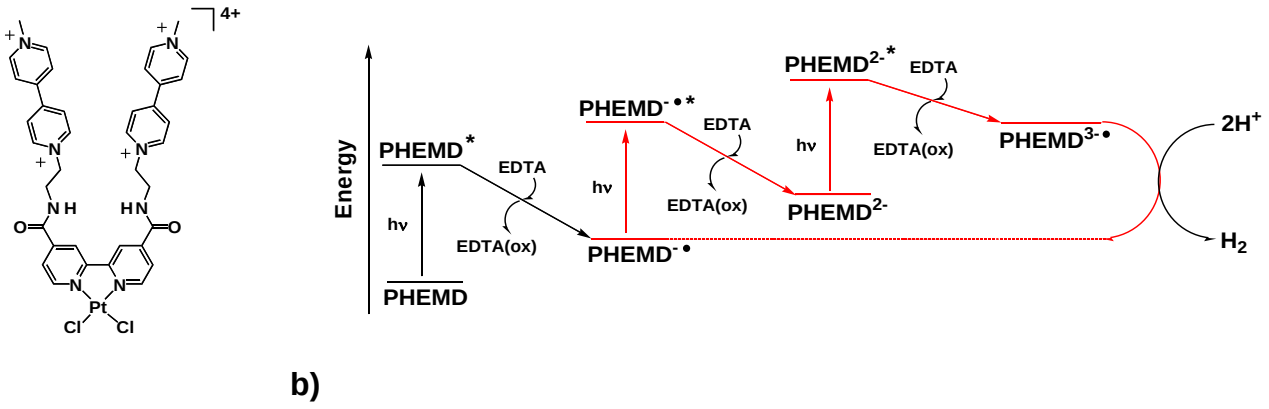

Figure 2. a) Structure of **[PtCl₂(bpyMV2)]⁴⁺**. b) Photochemical H_2 evolution cycling between singly and triply reduced **[PtCl₂(bpyMV2)]⁴⁺**.

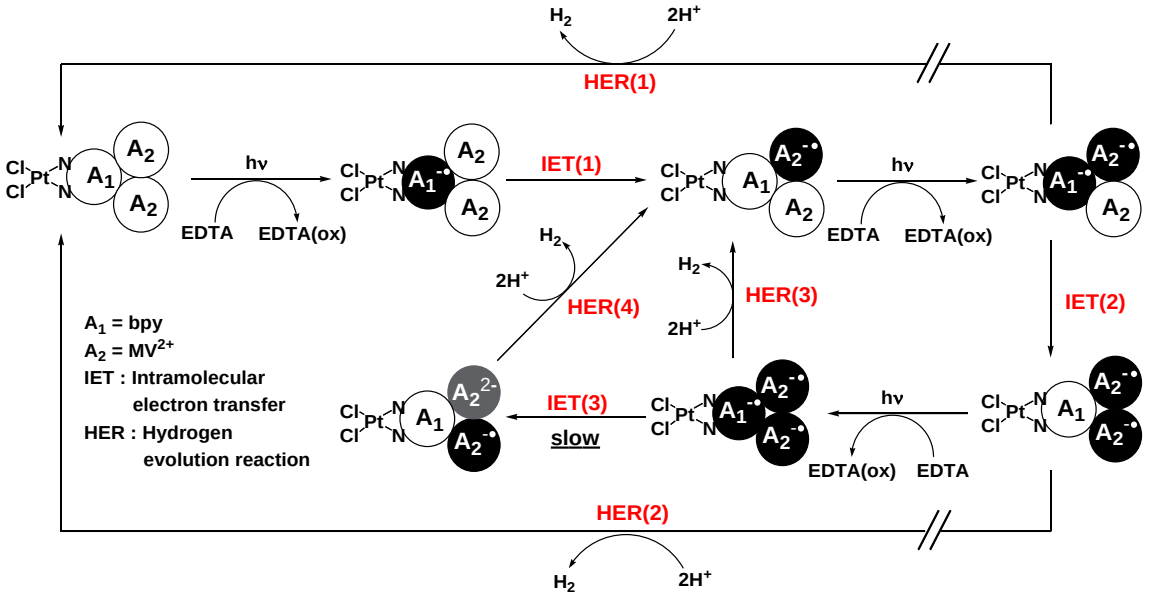

Figure 3. Reaction model of **[PtCl₂bpyMV2)]⁴⁺**.

Experimental Section

Materials

N,N’-Dicyclohexylcarbodiimide (DCC), N-hydroxysuccinimide (NHS), and N,N’-dimethyl-4-aminopyridine (DMAP) were purchased from Watanabe Chemical Industries. All other chemicals and solvents were purchased from Kanto Chemicals Co., Inc. and used without further purification. 4,4’-Dicarboxy-2,2’-bipyridine (dcbpy),[8] 1-(2-aminoethyl)-1'-methyl-4,4'-bipyridinium hexafluorophosphate,[9] *cis*-$PtCl_2(DMSO)_2$ (DMSO = dimethylsulfoxide),[10] $PtCl_2$(dcbpy)[6a] and $[Ru(bpy)_3](NO_3)_2•3H_2O$[11] were synthesized as previously described.

General Methods

UV-Vis and UV-Vis-NIR spectra were recorded on a Shimadzu UV-2600 and a Shimadzu UV-3600 spectrophotometer, respectively. Luminescence spectra were recorded on a Shimadzu RF5300PC spectrofluorophotometer. Low temperature emission spectra were measured for the glassy 77-K solution of each system contained in a quartz EPR tube. Emission decays were recorded on a HORIBA FluoroCube 3000USKU. The excitation source was a diode laser (374 nm) (HORIBA N-375L). ^{1}H NMR spectra were acquired on a JEOL JNM-ESA 600 spectrometer. ESI-TOF (electrospray ionization time-of-flight) mass spectra were acquired on a JEOL JMP-T100LP Accu-TOF mass spectrometer. Square wave voltammograms were recorded on a BAS ALS Model 602DKM electrochemical analyzer, using a three electrode system consisting of a platinum working electrode, a platinum wire counter electrode, and a Ag/Ag^+ reference electrode (0.249 V vs. SCE), where TBAP (tetra(n-butyl)ammonium perchlorate) was used as a supporting electrolyte and all potentials reported are given relative to the Fc/Fc^+ couple (Fc/Fc^+ = 0.380 vs SCE).

Synthesis of bpyMV2$(PF_6)_4•2H_2O$

A solution of 4,4’-dicarboxy-2,2’-bipyridine (501 mg, 2.05 mmol) in dry DMF (N,N-dimethylformamide) (20 mL) was stirred in the presence of DCC (282 mg, 4.12 mmol) and NHS (475 mg, 4.13 mmol) at 40 °C for 15 h. Then, the reaction mixture was filtered for the removal of insoluble materials. Ethanol (20 mL) and hexane (60 mL) were added to the filtrate. The resulting white solid was collected by filtration and dried in vacuo (4,4’-dicarboxysuccinimidyl-2,2’-bipyridine, 605 mg, 67.3 %). 1-(2-Aminoethyl)-1'-methyl-4,4'-bipyridinium hexafluorophosphate (405 mg, 0.801 mmol) and DMAP (98.4 mg, 0.805 mmol) were dissolved in dry DMF (2 mL), and the solution was added into a solution of 4,4’-dicarboxysuccinimidyl-2,2’-bipyridine (162 mg, 0.368 mmol) in dry DMF (6 mL). The solution

was stirred at 30 °C for 12 h. Then, the total volume of the solution was reduced to ca. 2 mL under reduced pressure, followed by addition of water (ca. 10 mL) to give the product as a pale pink solid. The product was redissolved in a mixture of water (5 mL) and acetone (5 mL) at 50 °C. Then the solution was left in air overnight to promote gradual evaporation of acetone to re-precipitate the final product, which was collected and dried in vacuo (yield: 358 mg, 77.4 %). ^{1}H NMR (CD_3CN/TMS, ppm): δ 8.93 (d, *J* = 6.2 Hz, 4H), 8.83 (d, *J* = 6.2 Hz, 4H), 8.79 (d, *J* = 5.0 Hz, 2H), 8.40 (s, 2H), 8.36 (m, 8H), 7.67-7.62 (m, 4H), 4.83 (t, *J* = 5.6 Hz, 4H), 4.39 (s, 6H), 4.01 (m, 4H); Anal. Calcd for $C_{38}H_{38}F_{24}N_8O_2P_4 \bullet 2H_2O$ (1254.65): C, 36.38; H, 3.37; N, 8.93. Found: C, 36.39; H, 3.39; N, 9.03.

Synthesis of $[PtCl_2(bpyMV2)](PF_6)_4 \bullet 2H_2O$

This was prepared by refluxing a solution of *cis*-$PtCl_2(DMSO)_2$ (70.1 mg, 0.166 mmol) and **bpyMV2**$(PF_6)_4 \bullet 2H_2O$ (201 mg, 0.160 mmol) in methanol (30 mL) for 11 h. After cooling down to room temperature, the resulting yellow solid was collected by filtration and recrystallized from a water/acetone mixture as described above for **bpyMV2**$(PF_6)_4 \bullet 2H_2O$ (yield: 134 mg, 53.2 %). ^{1}H NMR (CD_3CN/TMS, ppm): δ 9.87 (d, *J* = 6.2 Hz, 2H), 8.95 (d, *J* = 6.9 Hz, 4H), 8.85 (d, *J* = 6.9 Hz, 4H), 8.57 (s, 2H), 8.40 (d, *J* = 6.8 Hz, 4H), 8.37 (d, *J* = 6.9 Hz, 4H), 7.85 (dd, *J* = 6.2, 1.6 Hz, 2H), 7.79 (s, 2H), 4.86 (t, *J* = 5.5 Hz, 4H), 4.40 (s, 6H), 4.03 (m, 4H); ESI-TOF-MS: m/z = 1339.00 [M – PF_6] (calcd for $C_{38}H_{38}N_8O_2F_{18}P_3Cl_2Pt$: 1339.09); Anal. Calcd for $C_{38}H_{38}Cl_2F_{24}N_8O_2P_4Pt \bullet 2H_2O$ (1520.63): C, 30.01; H, 2.78; N, 7.37. Found: C, 30.01; H, 2.61; N, 7.36.

Photolysis Experiments

The photoirradiation was carried out by an ILC Technology CERMAX LX-300 Xe lamp (300 W) equipped with a CM-1 cold mirror ($400 < \lambda < 800$ nm). Photolysis was carried out using Pyrex glass vials which eliminates the lights below ca. 350 nm. Other experimental details are all same to those reported elsewhere.[6i]

DFT Calculations

Density functional theory (DFT) calculations were performed using the Gaussian 09 package of programs[12] to better understand the structural and spin-state candidates for the π-dimers given by stacking of two singly reduced viologen moieties within the PHEMD reported herein. Calculations were also performed to simulate the UV-Vis-NIR absorption spectra of the candidates computed. The structures were fully optimized using the M06 hybrid functional, developed by Truhlar *et al.*[13–15] with the effect of solvation in water taken into consideration using the polarizable continuum model (PCM)

method.[16-18] The SDD basis set was adopted for the Pt ion, while the 6-31G** basis set was applied to the rest of atoms. The choice of 6-31G** relies on experience of Sakai group that calculations using the 6-31G** basis set afford results essentially identical to those calculated using the 6-311+G(2d,p) basis set when this type of aromatic-aromatic interactions are computed using the M06 hybrid functional. Spin-restricted and -unrestricted methods (i.e., M06 and UM06) were respectively employed for closed- and open-shell singlet states. Particularly, UM06 calculations (Guess=Mix) in broken symmetry (BS) were performed for the open-shell singlet states. For such BS singlet-state calculations, spin contamination is exhibited by nonzero values for the spin-squared expectation value, defined with $<S^2>$ = S(S+1), where S is the molecular spin quantum number. Actually, the spin-squared expectation value after spin annihilation was confirmed to be 0.00, showing that spin contamination of the triplet state is negligible. This supports the validity of the BS approach for the open-shell singlet state without employing the spin-projected methods eliminating the redundant spin contaminations. Moreover, this open-shell singlet-state calculation afforded results equivalent to those given in the closed-shell singlet-state calculation (see below). All stationary points were characterized by their harmonic vibrational frequencies as minima. The unscaled frequencies were used to compute the zero-point vibrational energy corrections to the energies. Electronic excited states were calculated by the TD-DFT method as implemented in Gaussian 09[19-21] with use of the M06 functional and the same basis sets described above (Fig. 11). It is also tested the used of other functionals such as CAM-B3LYP, PBE0, B3PW91, and M06-2X (see Fig. 11), showing that the selection of M06 functional is valid within the scope this study. The calculated transitions were replaced by a Gaussian broadening function with a full width at half maximum height of 0.2 eV to simulate the electronic transition spectrum. Molecular orbital pictures were generated using GaussView 5.0.[22]

Quantum Yield Determination

The quantum yield for the H_2 evolution from water photocatalyzed by **$[PtCl_2(bpyMV2)]^{4+}$** was determined using potassium ferrioxalate, $K_3[Fe(III)(C_2O_4)_3]$, as a chemical actinometer.[23] The light source was same to that described above. However, the wavelength region used in the actinometry was further diminished into the range 360-400 nm (see Fig. 20) by employing a combination of Asahi Spectra SU400 and SV490 band-path glass filters. The chemical actinometry was carried out under the condition which satisfies complete absorption of lights within this wavelength range (see Fig. 20). The photon flux was determined as 5.22×10^{-7} einstein/s. The H_2 evolution rate under the steady state was determined as 2.677×10^{-11} mol/s (Fig. 21). As a result, the apparent quantum yield for H_2 evolution was determined as $\Phi(0.5H_2) = 0.010$. This value was further corrected into the more meaningful value

which defines $\Phi(0.5H_2)$ on the basis of absorption at the MLCT band of the $PtCl_2(bpy)$ chromophore. The correction factor was estimated as 0.53 (see Fig. 20) by evaluating the absorption features of both non-reduced and two-electron-reduced forms of **$[PtCl_2(bpyMV2)]^{4+}$**.

Results and Discussion

Photochemical Properties

As previously reported for **[PtCl$_2$(5,5'-MV4)]$^{8+}$**,[7b,24] the PtCl$_2$(bpy) chromophore possesses a metal-to-ligand charge transfer (^{1}MLCT) band at 388 nm (Figure 4), which can be used to generate a triplet excited state (^{3}MLCT state) that can be reductively quenched by a sacrificial electron donor present in solution. The concentration dependences of absorbance at two wavelengths in the concentration range of 0.04-0.2 mM, showing that they obey the Beer's law and is thereby dimerization in solution is negligible (Figure 5).

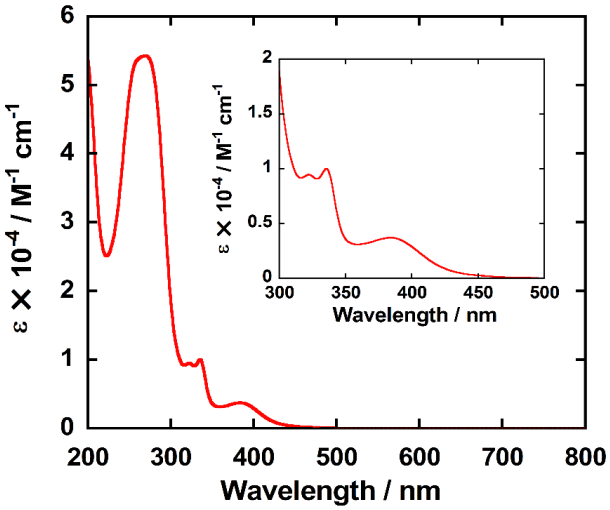

Figure 4. An absorption spectrum of **[PtCl$_2$(bpyMV2)]$^{4+}$** in an aqueous 0.1 M NaCl solution at 20 °C in air. The inset shows a magnification in the range 300-500 nm. The molar absorptivities at 270, 336, and 387 nm have been determined as 54200, 10000, and 3700 M^{-1} cm^{-1}, respectively.

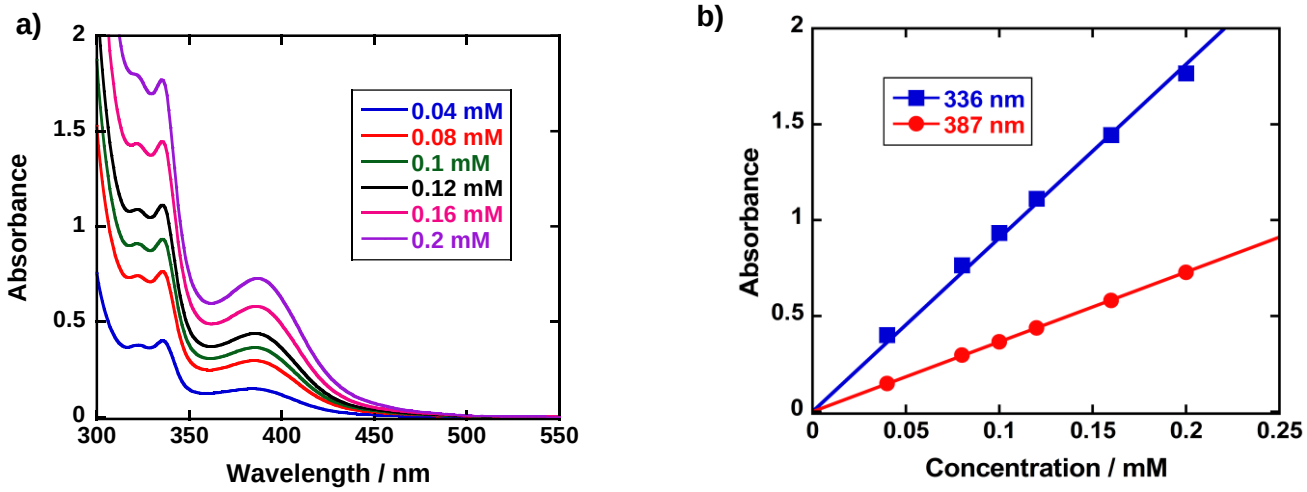

Figure 5. a) UV-Vis absorption spectra of **[PtCl$_2$(bpyMV2)]$^{4+}$** in an aqueous 0.1 M NaCl solution at various concentrations, at 20 °C in air. b) The concentration dependences of absorbance at two wavelengths in the concentration range of 0.04-0.2 mM.

[PtCl$_2$(bpyMV2)]$^{4+}$ does not exhibit emission at room temperature in aqueous solution. However, an emission in the range 500-700 nm is observed for **[PtCl$_2$(bpyMV2)]$^{4+}$** in a methanol/ethanol/N,N-dimethylformamide (MED; 4:4:1) glass at 77 K with the 0-0 and 0-1 vibronic emission peaks respectively centred at 496 and 533 nm with an average lifetime being $\langle\tau\rangle$ = 3.14 μs (see Figure 6 and Table 1). This long-lived character together with the large Stokes shift (ca. 150 nm) reveals that the emission arises from the triplet.

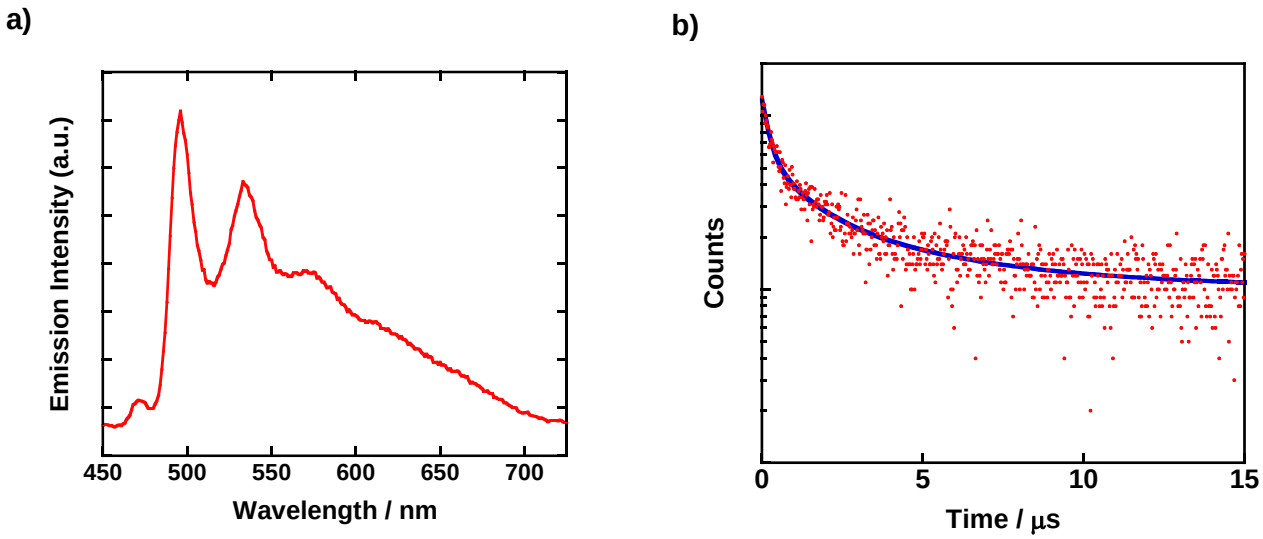

Figure 6. a) An emission spectrum of **[PtCl$_2$(bpyMV2)]$^{4+}$** in MED glass at 77 K (excitation at 380 nm), where MED is a 4/4/1 (v/v/v) methanol/ethanol/DMF mixture. b) An emission decay profile of **[PtCl$_2$(bpyMV2)]$^{4+}$** in MED glass at 77 K. The emission was monitored at 500 nm. The blue line shows a calculated one according to a triple exponential function.

Table 1. Emission wavelengths and lifetimes for **[PtCl$_2$(bpyMV2)]$^{4+}$** in MED glass at 77 K.

λ_{em} / nm	Lifetimes[a]	Relative contribution	$\langle\tau\rangle$[b] / μs
496, 533, 575, 612	τ_1 = 1.24 μs	χ_1 = 26.6 %	3.14 μs
	τ_2 = 4.56 μs	χ_2 = 15.8 %	
	τ_3 = 0.234 μs	χ_3 = 57.6 %	

[a]Lifetimes were estimated by fitting the decay at 500 nm to a triple exponential function. [b]Average lifetime $\langle\tau\rangle$ was estimated using a definition of $\langle\tau\rangle = \Sigma\, a_i\tau_i^2 / \Sigma\, a_i\tau_i$, where a_i is the relative contribution of the corresponding lifetime τ_i.[25]

Electrochemical Properties

Electrochemical study reveals that the first and second reductions of **[PtCl$_2$(bpyMV2)]$^{4+}$** occur at -0.80 and -1.20 V vs. Fc/Fc$^+$ (Figure 7), assignable to the MV^{2+}/MV$^{+\bullet}$ and MV$^{+\bullet}$/MV^0 couples, respectively. These assignments are unambiguous based on the values reported for the series of **PtCl$_2$(bpy)-(MV^{2+})$_n$** (n = 2, 4) dyads.[7b] The third reduction peak is observed at -1.30 V vs. Fc/Fc$^+$ and is assignable to the bpy/bpy$^{-\bullet}$ couple (Figure 7). These redox properties show that the driving force for the water reduction by a MV$^{+\bullet}$–based reducing equivalent is lower than those by the bpy$^{-\bullet}$–and MV^0–based reducing equivalents by 0.5 and 0.4 eV, respectively. This is correlated with my major finding that the bpy$^{-\bullet}$–based (or MV^0–based) reducing equivalent must be involved to drive photocatalytic H_2 formation with this system.

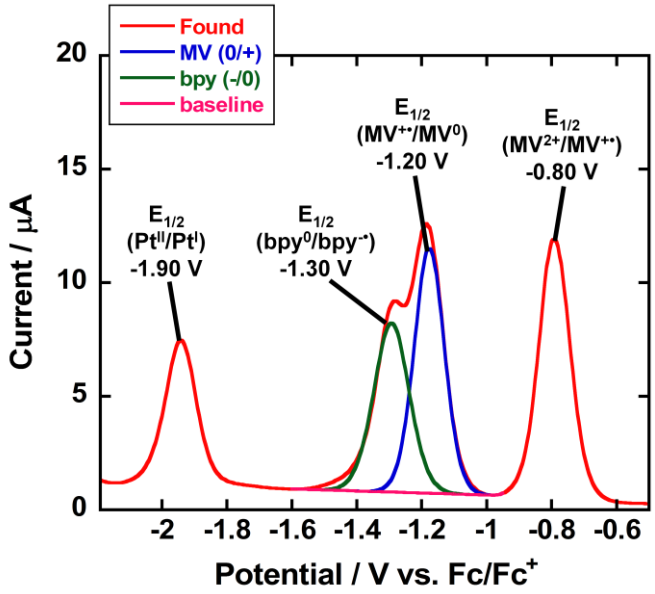

Figure 7. A square wave voltammogram of **[PtCl$_2$(bpyMV2)]$^{4+}$** (1 mM) in a DMF solution containing 0.1 M TBAP at room temperature under Ar atmosphere. For each case, deconvolution was carried out for the potential range where the reduction peaks of viologen and bpy are overlapped (−0.95 ~ −1.6 V vs. Fc/Fc$^+$).

Photo-driven Electron Storage Behavior

Next, I focus on the photo-driven electron storage behavior of **[PtCl$_2$(bpyMV2)]$^{4+}$** in the presence of EDTA. As previously observed for the series of **PtCl$_2$(bpy)-(MV^{2+})$_n$** dyads,[7b] photoirradiation of **[PtCl$_2$(bpyMV2)]$^{4+}$** results in growth of bands in the visible to near infrared region (Figure 8). The broad absorption features appearing above 800 nm are characteristic of those derived from the (MV^{+})$_2$ π-dimer species (i.e., **[PtCl$_2$(bpy)-(MV^{+})$_2$]$^{2+}$**).[26]

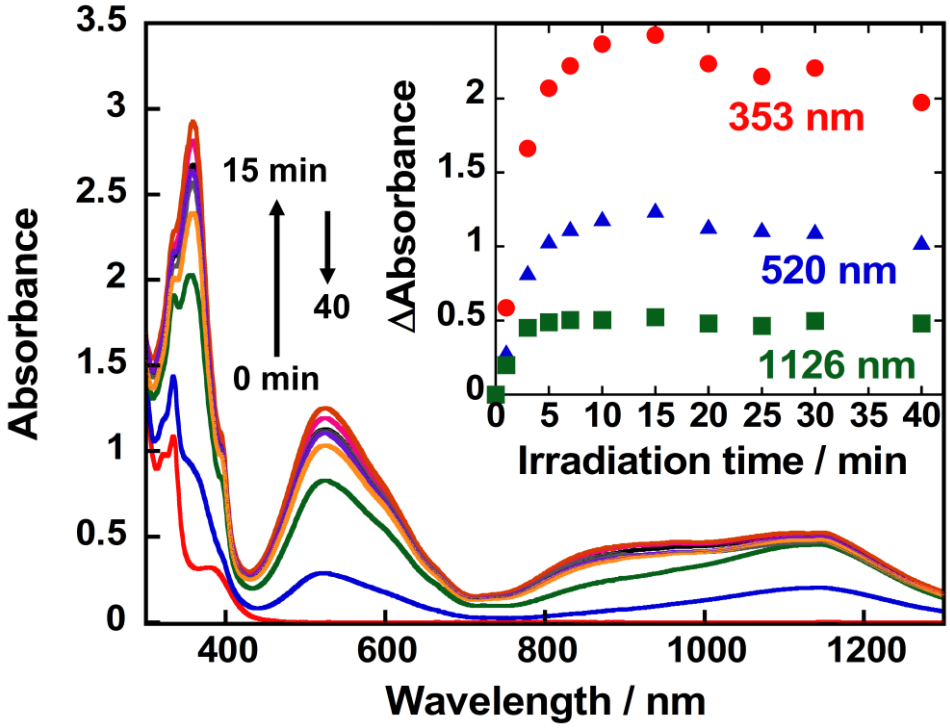

Figure 8. Spectral changes during the photolysis of an aqueous acetate buffer solution (pH 5.0; at 20 °C under Ar) containing 0.1 mM **[PtCl$_2$(bpyMV2)]$^{4+}$**, 0.1 M NaCl, and 30 mM EDTA. Inset: Absorbance changes at 353 nm (red), 520 nm (blue), and 1126 nm (green) during photolysis.

The geometrical and electronic structures of **$[PtCl_2(bpy)\text{-}(MV^+)_2]^{2+}$** were computed for both closed-shell and open-shell singlet states, in which a closed-shell singlet state turned out to be a unique solution for this two-electron-reduced system. The optimized geometry of **$[PtCl_2(bpy)\text{-}(MV^+)_2]^{2+}$** (singlet) has a structure in which two singly reduced viologen planes are stacked intramolecularly in a staggered fashion (Figure 9). Absorption features simulated using the TD-DFT results (Figure 10) are somewhat consistent with the observed spectral features. Formation of this $(MV^+)_2$ π-dimer species saturates after around 10-min irradiation.

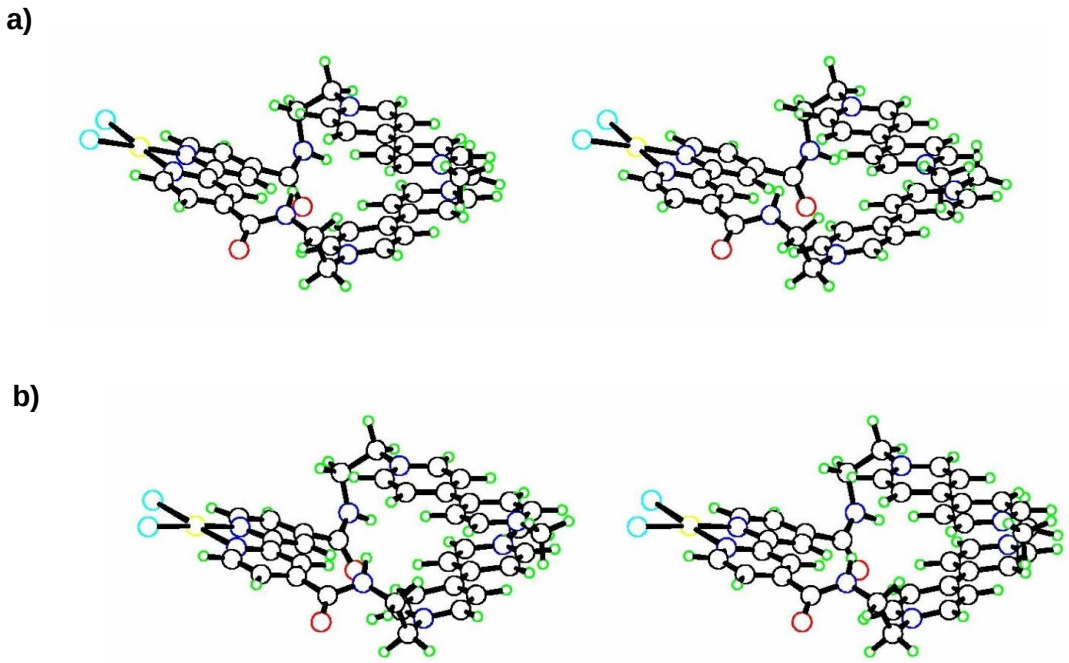

Figure 9. Stereo views showing the geometries for (a) the closed-shell singlet state and (b) the open-shell singlet state of the two-electron-reduced form of **$[PtCl_2(bpyMV2)]^{4+}$**. The structures were optimized at the M06 and UM06 level of DFT calculations with the effect of water solvation taken into consideration using the polarizable continuum model (PCM) method, where the SDD basis set was used for Pt and the 6-31G** basis set for H, C, N, O, and Cl. Geometry is shown in Table 1 (closed-shell singlet) and 2 (open-shell singlet) of the Appendix part in page 123-132.

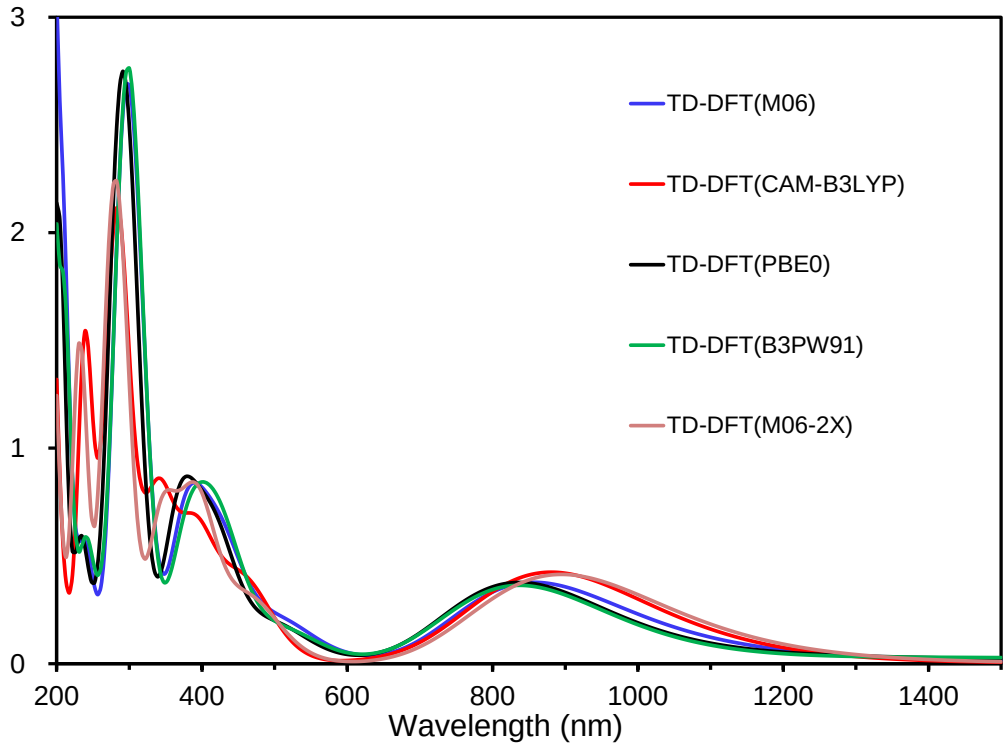

Figure 10. Spectral features simulated based on the TD-DFT calculations using several different functionals, such as M06, CAM-B3LYP, PBE0, P3PW91, and M06-2X, where the structure of **$[PtCl_2(bpy)\text{-}(MV^+)_2]^{2+}$** (closed-shell singlet) employed was that optimized at the M06/SDD(Pt)/6-31G**(HCNOCl)/PCM level of DFT. The results given for the open-shell singlet states were identical to those given for the corresponding closed-shell singlet states and have been thereby omitted in this figure. Electronic transitions are shown in Table 3 (closed-shell singlet) and 4 (open-shell singlet) of the Appendix part in page 133-162.

The molar absorptivity of the two-electron-reduced species at 353 nm (ε_{353} = 24000 $M^{-1}cm^{-1}$) was independently determined by adding a large excess of $Na_2S_2O_4$ (see Figure 11). This absorptivity value was used to calibrate the number of electrons stored per molecule, which corresponds to the vertical axis in Figure 12. The results reveal that approximately two electrons are stored per molecule under steady-state conditions.

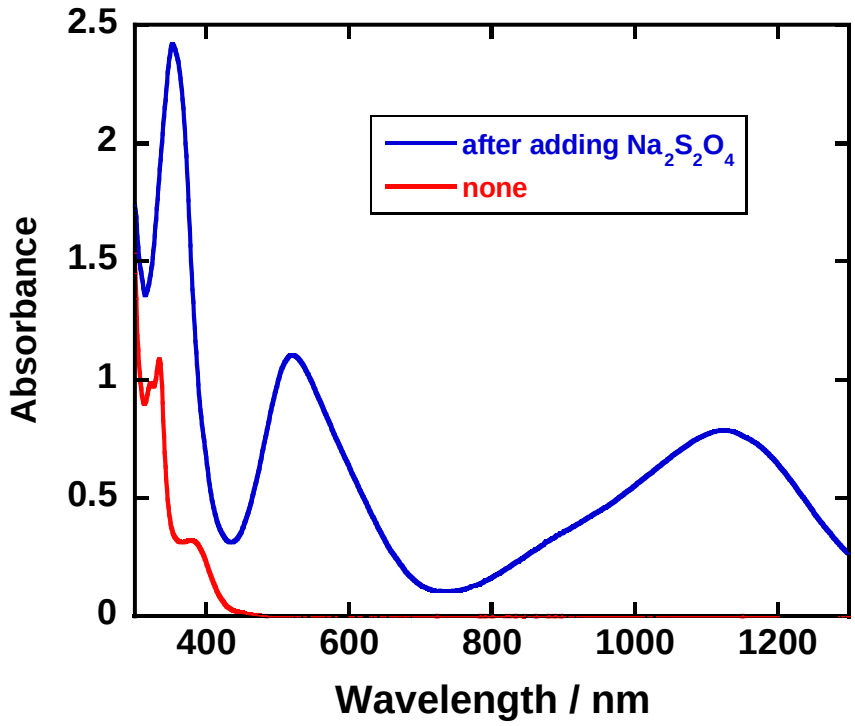

Figure 11. A spectral change of an aqueous acetate buffer solution (pH 5.0; at 20 °C under Ar) containing 0.1 mM **$[PtCl_2(bpyMV2)]^{4+}$**, 0.1 M NaCl, and 30 mM EDTA by adding ca. 0.24 mg (1.38 μmol) of $Na_2S_2O_4$.

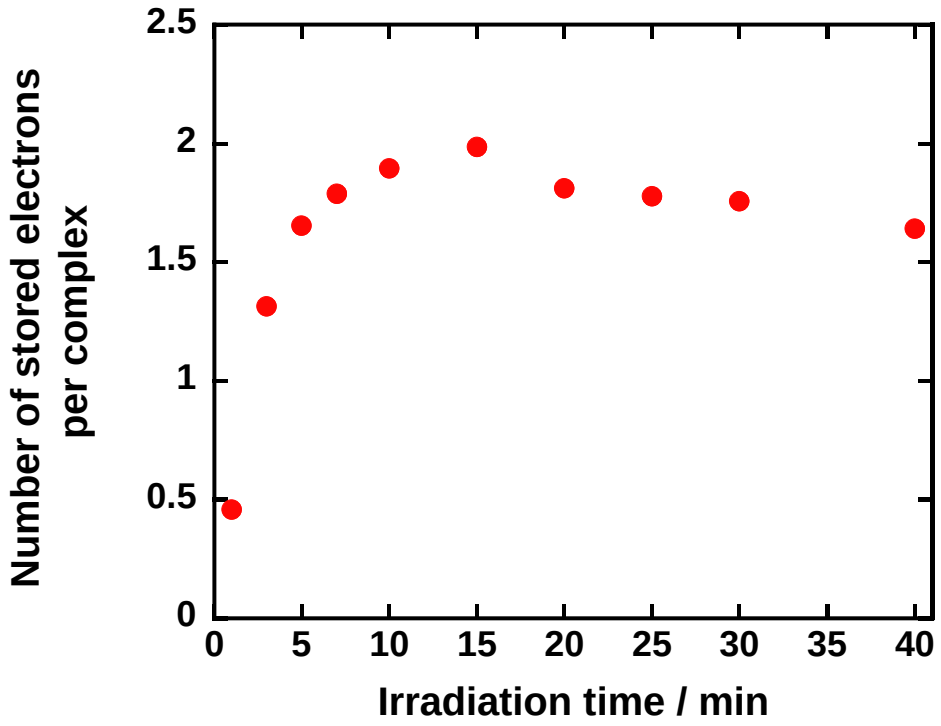

Figure 12. Changes in the total number of electrons stored over **[PtCl$_2$(bpyMV2)]$^{4+}$** during photolysis shown in Figure 8.

Moreover, the two-electron-reduced species generated in the above experiments shows only a minor decay over 1 h and does not exhibit a considerable decay over 15 h when it is left at 20 °C in the dark under Ar (see Figure 13), indicating that thermal reduction of water by this species (**[PtCl$_2$(bpy)-(MV$^+$)$_2$]$^{2+}$** + 2H$^+$ → **[PtCl$_2$(bpy)-(MV^{2+})$_2$]$^{4+}$** + H$_2$) is not a major path to H$_2$ evolution. As previously reported,[5c] electrochemically generated non-tethering free MV$^{+\bullet}$ does bleach in the presence of PtCl$_2$(dcbpy) due to the occurrence of thermal H$_2$ evolution reaction catalyzed by PtCl$_2$(dcbpy) (see Figure 14). This is correlated with the fact that the redox potential of (MV$^+$)$_2$ π-dimer is 0.15 V positive-shifted compared to that of the free MV$^{+\bullet}$ species, as reported ($E_{1/2}$((MV$^+$)$_2$/(MV^{2+})$_2$)= -0.55 V vs. SCE; $E_{1/2}$(MV$^{+\bullet}$/MV^{2+})= -0.70 V vs. SCE).[27]

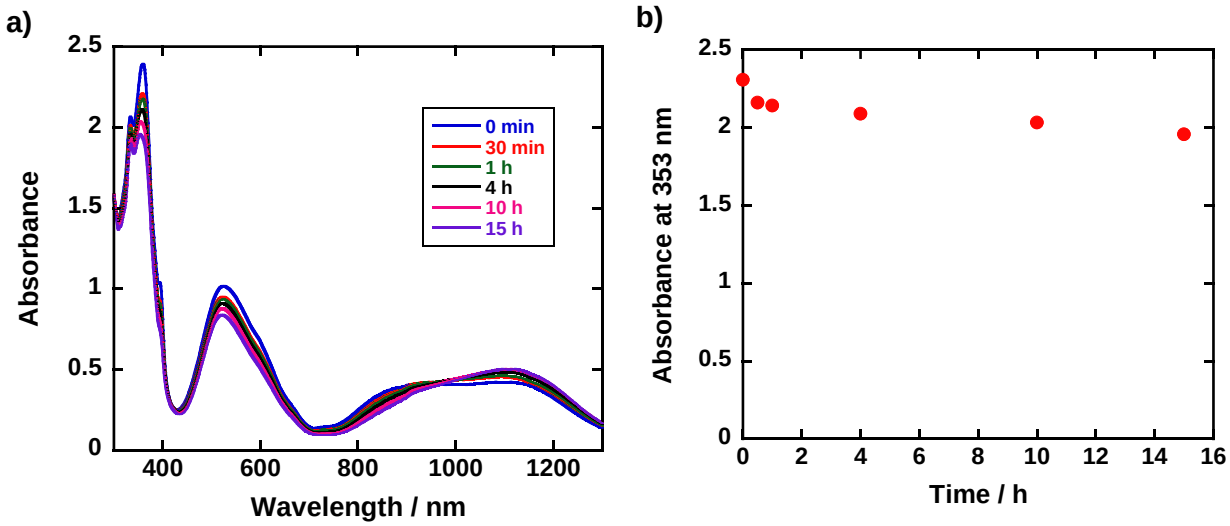

Figure 13. a) Spectral changes observed for an aqueous acetate buffer solution (pH 5.0; at 20 °C under Ar) containing 0.1 mM **[PtCl$_2$(bpyMV2)]$^{4+}$**, 0.1 M NaCl, and 30 mM EDTA in the dark after visible light irradiation (400 < λ < 800 nm) for 10 min. b) Change in absorbance at 353 nm, taken from the spectral changes in Figure 13.

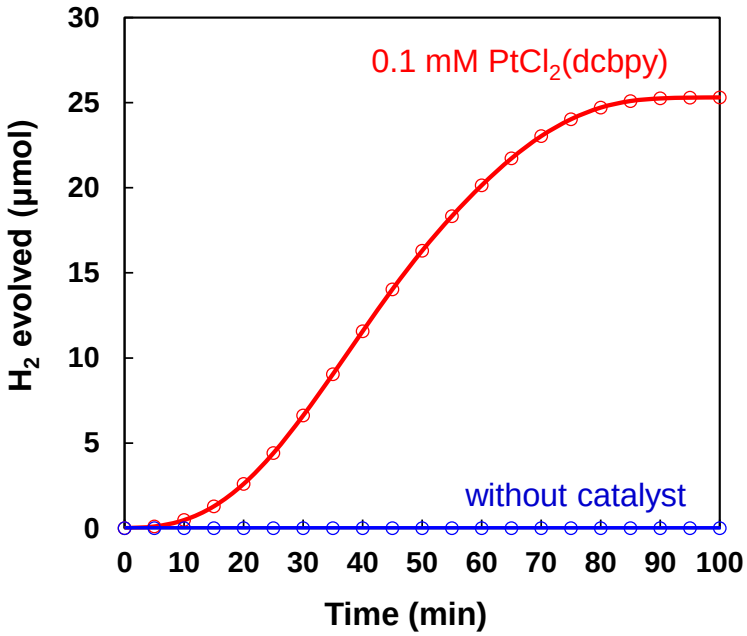

Figure 14. Thermal hydrogen production after mixing $MV^{+\bullet}$ (68 µmol; 1.5 mM) with $PtCl_2(dcbpy)$ (4.5 µmol; 0.1 mM) in an aqueous acetate buffer solutions containing 0.03 M CH_3COOH, 0.07 M CH_3COONa, and 0.1 M NaCl (pH 5.0, 45 mL) at 20 °C under Ar atmosphere. The solution of $MV^{+\bullet}$ was prepared by a bulk electrolysis of a solution of 5.0 mM $[MV]Cl_2 \cdot 3H_2O$ in the same buffer solution at –0.9 V vs. SCE. These experiments were performed as previously described.[5c]

Photochemical H_2 evolution

Photochemical H_2 evolution by **[$PtCl_2$(bpyMV2)]$^{4+}$** in the presence of EDTA is shown in Figure 15. The turnover number (TON) reaches 18 after 24-h irradiation. Importantly, the H_2 evolution rate remains nearly constant within 24 h, showing that this molecular photocatalyst is relatively stable. Note that viologen tethers are essential to enhance the H_2-evolving activity of such $PtCl_2$(bpy) derivatives, since photoirradiation of $PtCl_2$(dcbpy) and EDTA does not lead to H_2 evolution.[7b]

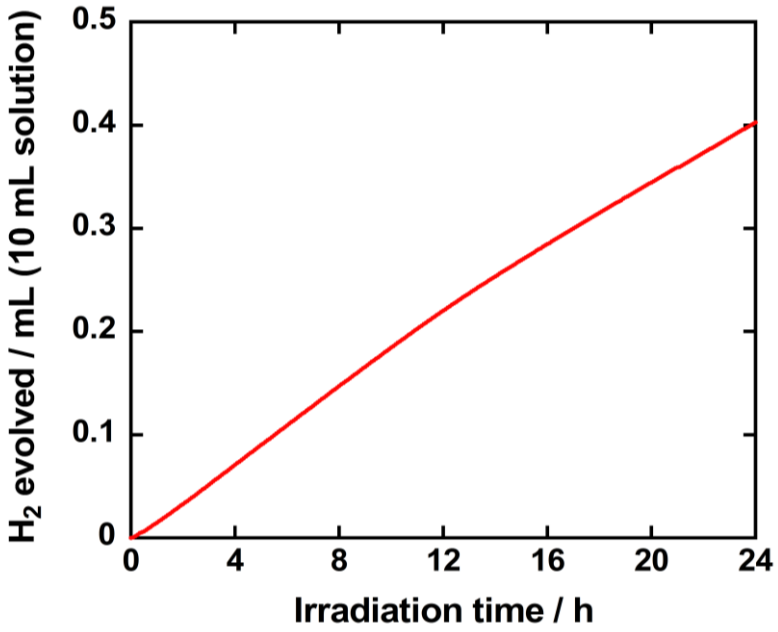

Figure 15. Photochemical H_2 production from an aqueous acetate buffer solution (pH 5.0, 10 mL; at 20 °C under Ar) containing 0.1 mM **[$PtCl_2$(bpyMV2)]$^{4+}$**, 0.1 M NaCl, and 30 mM EDTA.

In situ dynamic light scattering (DLS) measurements were also carried out to check for colloidal platinum formation. The light scattering intensity during the photocatalysis using **[PtCl$_2$(bpyMV2)]$^{4+}$** at first increases due to dispersion of unidentified particles (Figure 16 red and Figure 17). However, upon exposure of the resultant solution to air, the light scattering intensity abruptly decreases and the initial blank level of scattering intensity can be recovered (see Figure 16 blue). Therefore, the observed dispersion during the photolysis must be caused by partial precipitation of some reduced forms of **[PtCl$_2$(bpyMV2)]$^{4+}$** that have lower solubility to aqueous media. Precipitation of such reduced species has often been observed in previous studies.[6j] These observations clearly rule out colloidal platinum formation under my photolysis conditions.

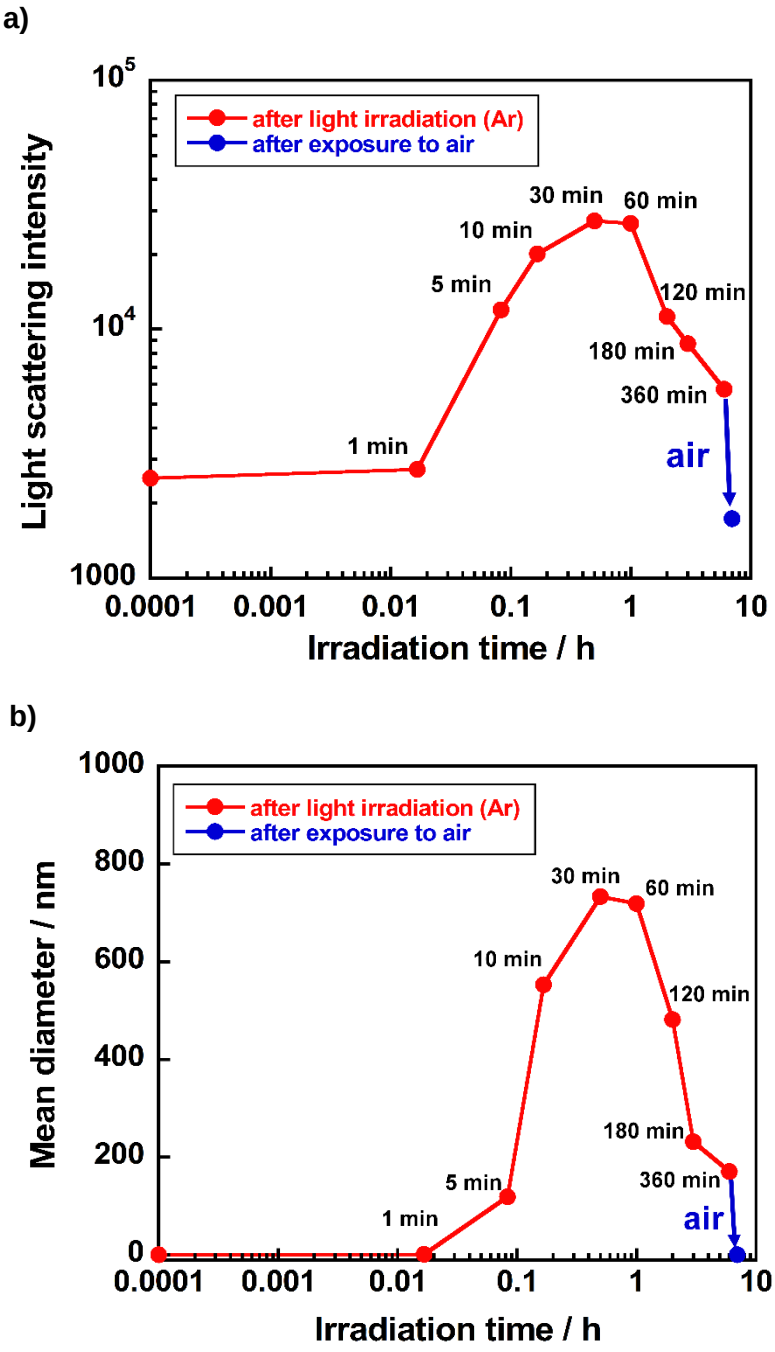

Figure 16. DLS measurements during the photolysis of an aqueous acetate buffer solution (pH 5.0; at 20 °C under Ar) containing 0.1 mM **$[PtCl_2(bpyMV2)]^{4+}$**, 0.1 M NaCl, and 30 mM EDTA. a) Changes in light scattering intensity during the photolysis. b) Changes in a mean diameter of particles dispersed during the photolysis. The maximum particle size seen here (ca. 800 nm) is much larger than those of the platinum nanoparticles given from K_2PtCl_4 under similar experimental conditions (ca. 200 nm; data not shown).

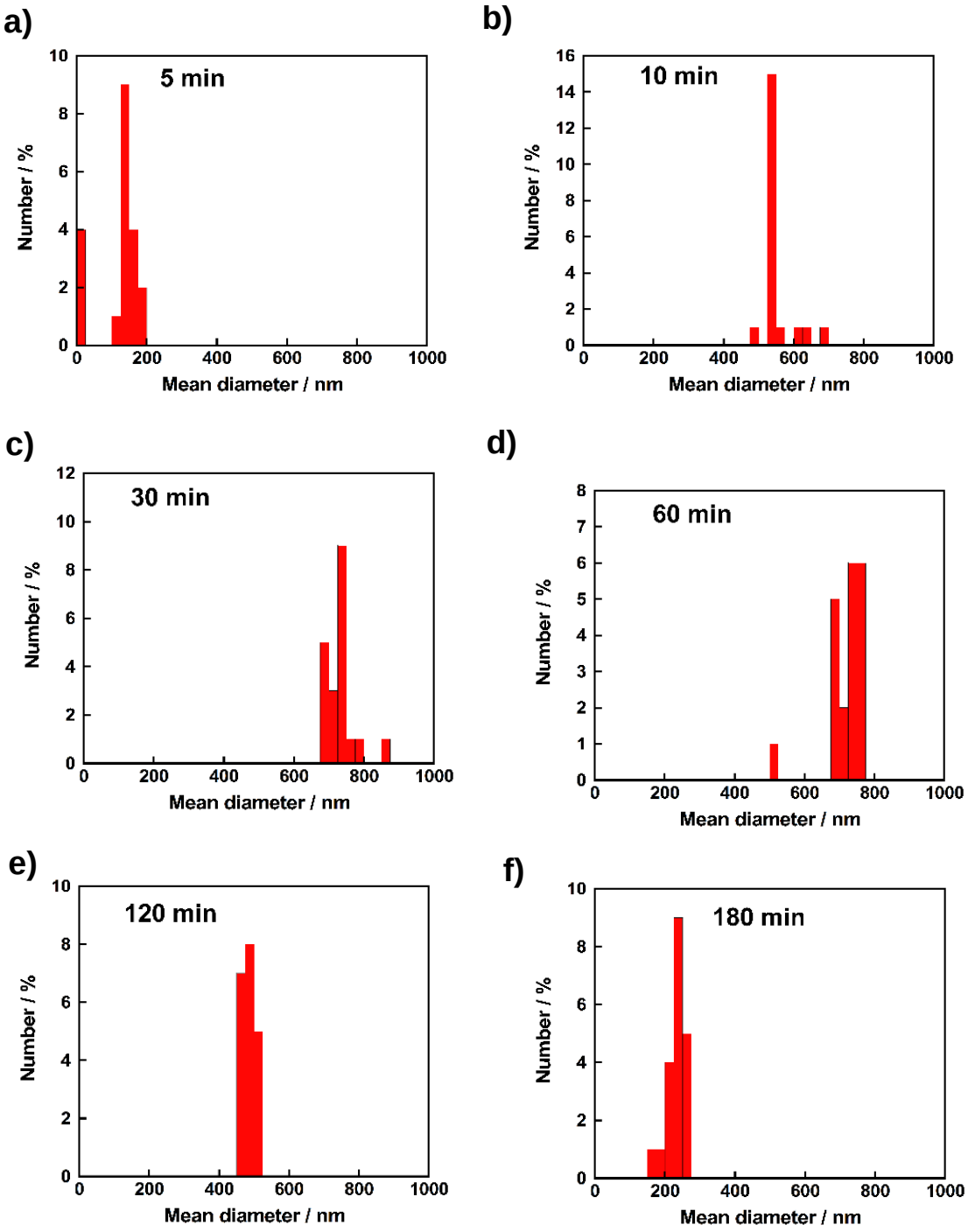

Figure 17. The particle size distribution of unidentified particles generated during the photolysis experiments shown in Figure 16 at a) 5 min, b) 10 min, c) 30 min, d) 60 min, e) 120 min, and f) 180 min.

Importantly, I observe quite clear ON-OFF behavior for H_2 generation upon turning ON and OFF the light irradiation (see Figure 18). As discussed above for Fig. 13, the major chemical species in solution is a two-electron-reduced species at each light-off time shown in Figure 18, which re-confirms that thermal reduction of water by **[PtCl$_2$(bpy)-(MV$^+$)$_2$]$^{2+}$** does not proceed under these conditions. As a result, I can conclude that the observed H_2 evolution results from the photoexcitation of the two-electron-reduced species. This has a similarity to the H_2 evolution via two consecutive photo-driven electron transfer steps discovered for **PV^{2+}** in which photoexcitation of **PV$^{+\bullet}$** is essential to generate the doubly reduced species (**PV^0**) which thermally reduces water to H_2.[7a] With **[PtCl$_2$(bpyMV2)]$^{4+}$**, photoexcitation of the two-electron-reduced species obviously plays a major role in generating species that drives thermal H_2 evolution from water. This indicates H_2 evolution is driven only by bpy$^{-\bullet}$–based (or MV^0–based) reducing equivalent which promotes the reaction with higher driving force than MV$^{+\bullet}$–based reducing equivalent in this system. Furthermore, I consider that the other **Pt(bpy)-A** systems also drive H_2 evolution with these reducing equivalent. I now assume that **HER(3)** predominates **HER(4)** because of the slower nature of **IET(3)** (lower driving force for this IET; ΔG_{IET} = -0.1 eV; see Figure 7) as well as the lower driving force for the H_2 evolution via **HER(4)**. The initial minor decay of reduced species seen in Figure 13 might correspond to the occurrence of **HER(4)**. Nevertheless, the more detailed studies are needed to further clarify this observation.

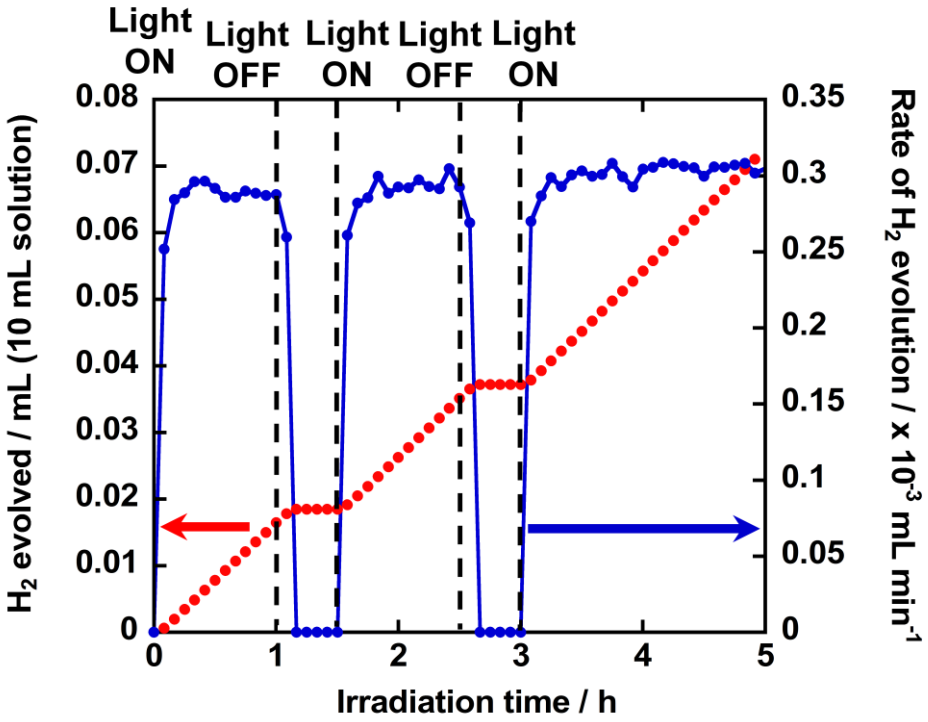

Figure 18. Photoresponse of H_2 production. Red and blue dots correspond to the amount of H_2 evolved and the rate of H_2 evolution, respectively, where experimental conditions are the same as those in Figure 15.

My above results indicate that **[PtCl$_2$(bpyMV2)]$^{4+}$** is a unique system which can only drive H_2 evolution via formation of three-electron-reduced species which include a bpy$^{-\bullet}$–based (or MV$^{\mathbf{0}}$–based) reducing equivalent, as illustrated with path **HER(3)** (or **HER(4)**). Possibly, this is due to the close location of MV^{2+} with regard to the bpy moiety, which enables rapid intramolecular electron transfer from bpy$^{-\bullet}$ to one of the adjacent MV^{2+} units, if there is any un-reduced MV^{2+} site. In other words, the **IET(2)** step in Figure 3 is much faster than the competing H_2 evolution path **HER(1)**. On the contrary, I assume that the **[PtCl$_2$(5,5'-MV4)]$^{8+}$** family can adopt the thermal path **HER(1)** since they can photocatalyze H_2 evolution while a portion of the multiple MV^{2+} sites remain un-reduced, presumably due to the slower nature of both the **IET(1)** and **IET(2)** steps.[7b] As a result, I conclude that all the MV^{2+} sites in **[PtCl$_2$(bpyMV2)]$^{4+}$** must be reduced in order to generate a bpy$^{-\bullet}$ (or MV$^{\mathbf{0}}$) site required to drive the H_2 evolution process.

Quantum Yield of H_2 Formation

The quantum yield of H_2 formation is determined with below methods (Figures. 19,20). With the feature demonstrated in Figure 19, it was estimated that 53% of the incident light absorbed by the two-electron-reduced species contribute to the excitation of the $PtCl_2$(bpy)-based MLCT chromophore. As a result, the apparent quantum yield of H_2 formation was corrected by dividing it by this factor (i.e., 0.53). The quantum yield of H_2 formation, which was estimated with the results of photochemical H_2 evolution (Figure 20), is relatively low for the present system ($\Phi(0.5H_2) = 0.02\%$).

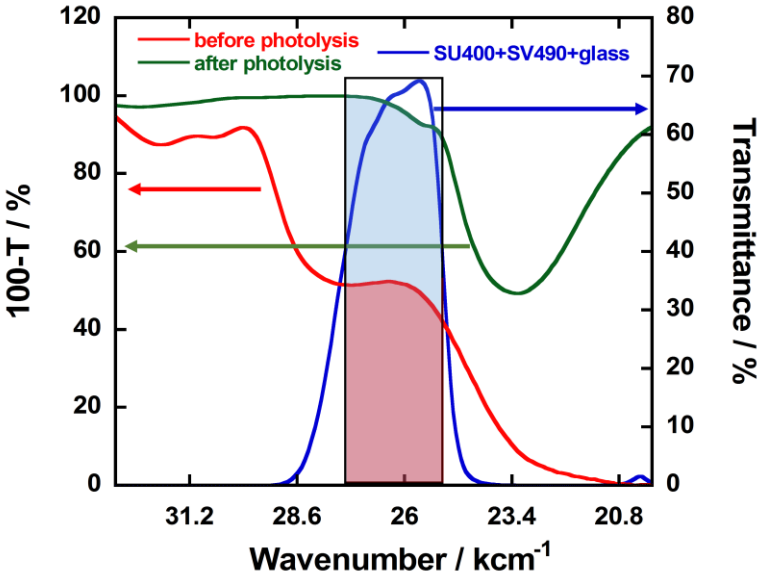

Figure 19. Transmittance property for the employed combination of glass filters is shown by a blue line (this include the transmittance component of the Pyrex glass vial employed in the measurement). The red and green lines correspond to the absorption properties of non-reduced and two-electron-reduced species.

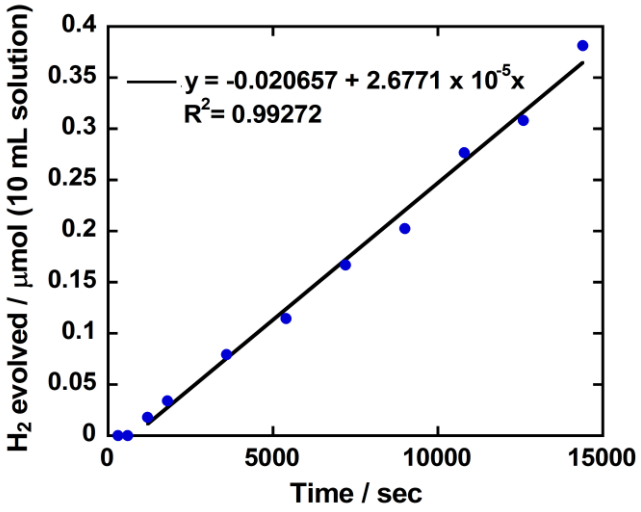

Figure 20. Photochemical H_2 production from an aqueous acetate buffer solution (pH 5.0, 10 mL; at 20 °C under Ar) containing 0.1 mM **[PtCl$_2$(bpyMV2)]$^{4+}$**, 0.1 M NaCl, and 30 mM EDTA, under photoirradiation in the 360-400 nm domain using the set of glass filters described in Figure 19.

This is likely due to quenching of the $PtCl_2$(bpy)-based ^{3}MLCT state by the $(MV^+)_2$ π-dimer moiety in close proximity, as demonstrated by the complete quenching of emission from **[PtCl$_2$(bpy)-(MV$^+$)$_2$]$^{2+}$** generated from **[PtCl$_2$(bpyMV2)]$^{4+}$** by adding $Na_2S_2O_4$ in a frozen media at 77 K (Figure 21). Judging from the results of the similar experiments using $Ru(bpy)_3^{2+}$ instead of **[PtCl$_2$(bpyMV2)]$^{4+}$** (Figure 22), I rule out the quenching of a ^{3}MLCT state by the presence of $Na_2S_2O_4$, leading to my conclusion that the ^{3}MLCT state generated within the two-electron-reduced species **[PtCl$_2$(bpy)-(MV$^+$)$_2$]$^{2+}$** is effectively self-quenched by the $(MV^+)_2$ π-dimer unit tethered to the $PtCl_2$(bpy) moiety in a close contact.

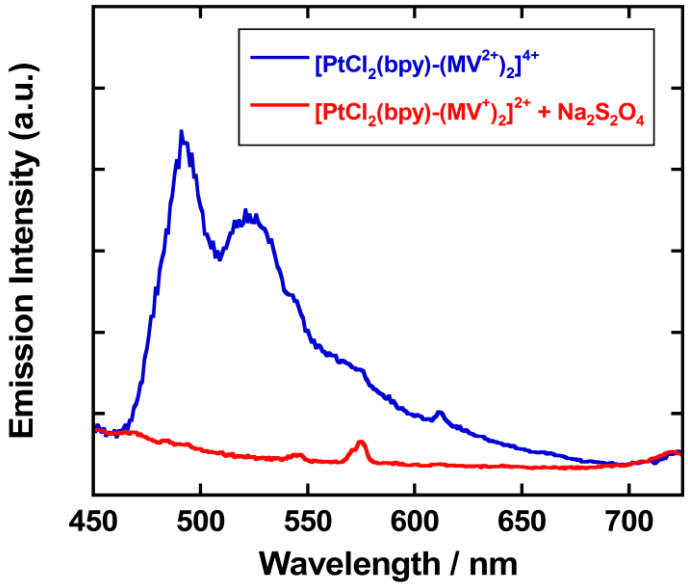

Figure 21. The solution was prepared by dissolving the compound (0.01 mM) in a 1:2 mixture of aqueous acetate buffer (0.1 M, pH 5.0) containing NaCl (0.1 M) and ethylene glycol (0.25 mL) and was sealed in a quartz EPR tube under He. Measurements were carried out at 77 K in a frozen glass, before and after adding $Na_2S_2O_4$ (7 mg, 40 μmol). Emission spectra (excitation at 380 nm) of the non-reduced species **$[PtCl_2(bpy)\text{-}(MV^{2+})_2]^{4+}$** (blue line) and the two-electron-reduced species **$[PtCl_2(bpy)\text{-}(MV^{+})_2]^{2+}$** (red line) generated by adding an excess of $Na_2S_2O_4$.

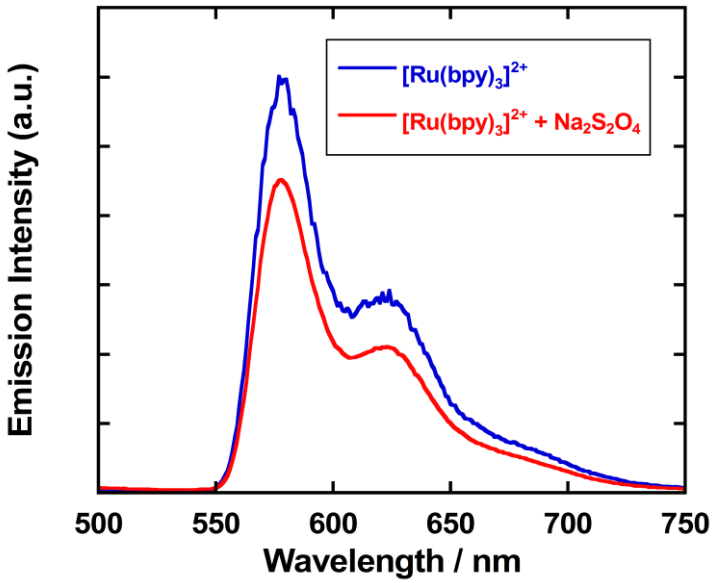

Figure 22. Emission spectra (excitation at 425 nm) of 0.01 mM $[Ru(bpy)_3](NO_3)_2 \cdot 3H_2O$ before (blue line) and after (red line) adding $Na_2S_2O_4$. The solution was prepared by dissolving the compound in a 1:2 mixture of water and ethylene glycol (0.25 mL) and was sealed in a quartz EPR tube under He. Other conditions are same to those described above. Note that the emission intensity was quite sensitive to the manually tuned position of each sample so that quantitative comparison of the emission intensities does not make sense.

Conclusions

In this study, a new Pt(II) complex tethered to two MV^{2+} moieties, **[PtCl$_2$(bpyMV2)]$^{4+}$**, was synthesized and its catalytic properties as a Pt(II)-based **PHEMD** were investigated in detail. It was confirmed that **[PtCl$_2$(bpyMV2)]$^{4+}$** quantitatively stores two electrons by forming two-electron-reduced species, **[PtCl$_2$(bpy)-(MV$^+$)$_2$]$^{2+}$**, during the photoirradiation in the presence of EDTA and this reduced species cannot promote H_2 evolution without further photoexcitation. This shows photocatalysis of **[PtCl$_2$(bpyMV2)]$^{4+}$** for H_2 evolution from water proceeds via the third photochemical step leading to the formation of three-electron-reduced species (Figure 23). This feature is distinct from other Pt-based **PHEMD**s, where two-electron-reduced species promote H_2 evolution, and due to the close location of MV^{2+} sites to a Pt complex site, which leads to rapid intramolecular electron transfer from $bpy^{-\bullet}$ to one of the MV^{2+} sites. Furthermore, this study shows the importance of the formation of $bpy^{-\bullet}$-based species for H_2 evolution in the **Pt(bpy)-MV^{2+}** systems. Although this system does not show much high activity, it allows me to demonstrate the very important strategy for the development of more highly active **PHEMD**s; positions of electron-reservoir sites are crucial for their catalytic behaviors.

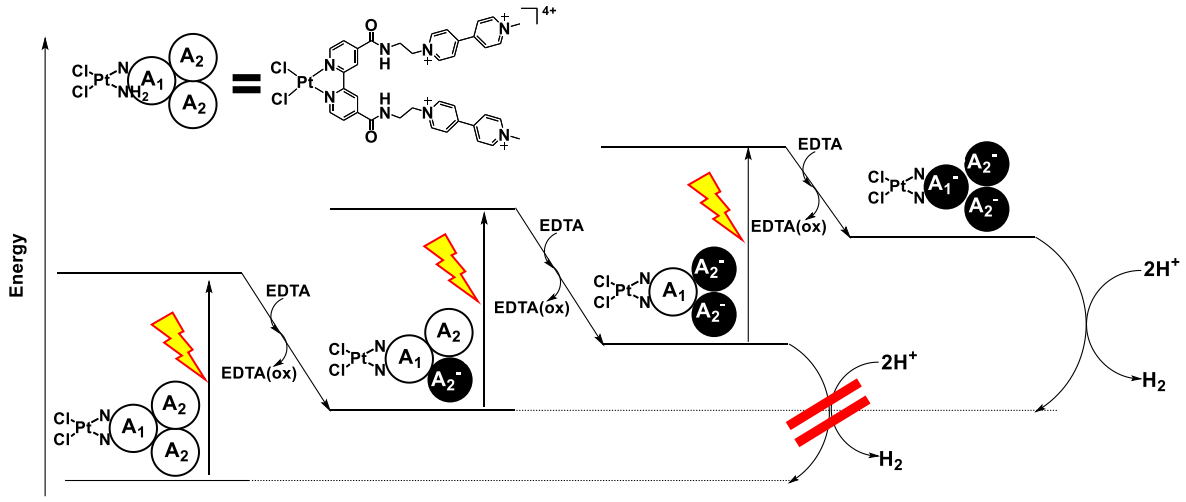

Figure 23. A reaction scheme of photocatalytic H_2 evolution promoted by **[PtCl$_2$(bpyMV2)]$^{4+}$**.

References

1. A. J. Esswein and D. G. Nocera, *Chem. Rev.*, 2007, **107**, 4022.
2. (a) A. Kudo and Y. Miseki, *Chem. Soc. Rev.*, 2009, **38**, 253.
   (b) K. Sayama, K. Mukasa, R. Abe, Y. Abe and H. Arakawa, *Chem. Commun.*, 2001, 2416.
   (c) K. Maeda, K. Teramura, D. Lu, T. Takata, N. Saito, Y. Inoue and K. Domen, *Nature*, 2006, **440**, 295.
3. (a) M. Wang, L. Chen and L. Sun, *Energy Environ. Sci.*, 2012, **5**, 6763.
   (b) S. Losse, J. G. Vos and S. Rau, *Coord. Chem. Rev.*, 2010, **254**, 2492.
4. (a) M. D. Kärkäs, O. Verho, E. V. Johnston and B. Åkermark, *Chem. Rev.*, 2014, **114**, 11863.
   (b) J. D. Blakemore, R. H. Crabtree and G. W. Brudvig, *Chem. Rev.*, 2015, **115**, 12974
5. (a) H. Ozawa, Y. Yokoyama, M. Haga and K. Sakai, *Dalton Trans.*, 2007, 1197.
   (b) K. Sakai and H. Ozawa, *Coord. Chem. Rev.*, 2007, **251**, 2753.
   (c) K. Yamauchi, S. Masaoka and K. Sakai, *J. Am. Chem. Soc.*, 2009, **131**, 8404.
6. (a) H. Ozawa, M. Haga and K. Sakai, *J. Am. Chem. Soc.*, 2006, **128**, 4926.
   (b) S. Masaoka, Y. Mukawa and K. Sakai, *Dalton Trans.*, 2010, **39**, 5868.
   (c) H. Ozawa, M. Kobayashi, B. Balan, S. Masaoka and K. Sakai, *Chem. Asian J.*, 2010, **5**, 1860.
   (d) M. Hirahara, S. Masaoka and K. Sakai, *Dalton Trans.*, 2011, **40**, 3967.
   (e) H. Ozawa and K. Sakai, *Chem. Commun.*, 2011, **47**, 2227.
   (f) G. Ajayakumar, M. Kobayashi, B. Balan, S. Masaoka and K. Sakai, *Dalton Trans.*, 2011, **40**, 3955.
   (g) C. V. Suneesh, B. Balan, H. Ozawa, Y. Nakamura, T. Katayama, M. Muramatsu, Y. Nagasawa, H. Miyasaka and K. Sakai, *Phys. Chem. Chem. Phys.*, 2014, **16**, 1607.
   (h) R. Okazaki, S. Masaoka and K. Sakai, *Dalton Trans.*, 2009, 6127.
   (i) M. Kobayashi, S. Masaoka and K. Sakai, *Dalton Trans.*, 2012, **41**, 4903.
   (j) K. Yamauchi and K. Sakai, *Dalton Trans.*, 2015, **44**, 8685.
7. (a) M. Kobayashi, S. Masaoka and K. Sakai, *Angew. Chem. Int. Ed.*, 2012, **51**, 7431.
   (b) K. Kitamoto and K. Sakai, *Angew. Chem. Int. Ed.*, 2014, **53**, 4618.
   (c) K. Kitamoto and K. Sakai, *Chem. Commun.*, 2016, **52**, 1385.
8. A. R. Oki and R. J. Morgan, *Synth. Commun.*, 1995, **25**, 4093.
9. L. A. Kelly, and M. A. J. Rodgers, *J. Phys. Chem.*, 1994, **98**, 6386.
10. J. H. Price, A. N. Williamson, R. F. Schramm and B. B. Wayland, *Inorg. Chem.*, 1972, **11**, 1280.
11. K. Sakai, Y. Kizaki, T. Tsubomura and K. Matumoto, *J. Mol. Catal.*, 1993, **79**, 141.

12. M. J. Frisch *et al*., Gaussian 09 Revision C.01 (Gaussian Inc., Wallingford CT, 2009).

13. Y. Zhao and D. G. Truhlar, *Theor. Chem. Acc.,* 2008, **120**, 215.

14. Y. Zhao and D. G. Truhlar, *J. Phys. Chem. A*, 2008, **112**, 1095.

15. Y. Zhao and D. G. Truhlar, *Acc. Chem. Res.*, 2008, **41**, 157.

16. V. Barone, M. Cossi and J. Tomasi, *J. Comp. Chem.*, 1998, **19**, 404.

17 M. Cossi, G. Scalmani, N. Rega and V. Barone, *J. Chem. Phys.*, 2002, **117**, 43.

18. J. Tomasi, B. Mennucci and R. Cammi, *Chem. Rev.*, 2005, **105**, 2999.

19. M. E. Casida, C. Jamorski, K. C. Casida and D. R. Salahub, *J. Chem. Phys*., 1998, **108**, 4439.

20. R. E. Stratmann, G. E. Scuseria and M. J. Frisch, *J. Chem. Phys.*, 1998, **109**, 8218.

21. R. Bauernschmitt and R. Ahlrichs, *Chem. Phys. Lett.*, 1996, **256**, 454.

22. GaussView, Version 5, R. Dennington, T. Keith and J. Millam, *Semichem Inc.,* Shawnee Mission, KS, 2009.

23. C. G. Hatchard and C. A. Parker, *Proc. R. Soc. London, Ser. A.*, 1956, **235**, 518-536.

24. M. Ogawa, G. Ajayakumar, S. Masaoka, H.-B. Kraatz and K. Sakai, *Chem. Eur. J.*, 2011, **17**, 1148.

25. D. R. James, Y.-S. Liu, P. De Mayo and W. R. Ware, *Chem. Phys. Lett.*, 1985, **120**, 460-465.

26. C. Lee, Y. M. Lee, M. S. Moon, S. H. Park, J. W. Park, K. G. Kim and S.-J. Jeon, *J. Electroanal. Chem.*, 1996, **416**, 139.

27. W. S. Jeon, H.-J. Kim, C. Lee and K. Kim, *Chem. Commun.*, 2002, 1828.

Chapter 2

Photocatalytic H_2 Evolution Using a Ru Chromophore Tethered to Six Viologen Acceptors

Introduction

One of the most important and ambitious challenges in our society is the development of renewable energy sources that have a modest environmental footprint.[1] Solar energy is very attractive and unlimited, but its wide implementation requires the development of new storage technologies. In the past years, light-driven water splitting into molecular H_2 and O_2 has received considerable attention due to its ideal approach to store the solar energy into an energy-dense and clean-burning fuel, hydrogen (H_2 + ½ O_2 → H_2O).[2-4]

In green plants, the photosynthetic reaction centers consist of two light-harvesting proteins (PSI and PSII), which work together to generate high-energy products (ATP and NADPH) by absorbing sunlight based on the Z-scheme.[5-6] An intriguing feature is that multi-electron transfer processes are conducted at the exciton-coupled dimer of chlorophylls, which is repeatedly photo-excited to drive rapid and consecutive one-electron transfer processes, leading to storage of multiple electrons at the quinone pool ($nQ + 2nH^+ + 2ne^- \rightarrow nH_2Q$).[7] Inspired by their behaviors, extensive efforts have been made to develop artificial molecular systems demonstrating such single-component-driven multi-electron transfer processes within a unimolecular framework.[8-11] Nevertheless, only a limited number of such systems have been adopted in actual photo-driven multi-electron transfer processes leading to produce solar fuels (e.g., water or CO_2 reduction).[12-13]

In this context, Sakai group recently reported new $Ru(bpy)_3^{2+}$ (bpy; 2,2'-bipyridine) chromophores tethered to L-aspartic-acid-based backbones having twelve methyl viologen acceptors (MV^{2+}; *N,N'*-dimethyl-4,4'-bipyridinium) (e.g., **[Ru(4,4'-aspMV4)$_3$]$^{26+}$** in Figure 1), which we term molecular "photo-charge-separators (**PCS**s)".[13a] These systems demonstrated that multiple electrons can be photochemically pumped out from the sacrificial electron donors to be stored over the **PCS** framework, leading to storage of 7-8 electrons per **PCS**. In the study, EDTA (ethylenediaminetetraacetic acid disodium salt; Na_2YH_2) was used as a sacrificial electron donor due to the high affinity of the di-deprotonated EDTA anions (YH_2^{2-}) with the positively charged **PCS**s and thus enhancing the reductive quenching of the triplet state of the chromophore through the formation of ion-pair adducts. Although the electrons were transferred into the MV^{2+} units and thus one-electron-reduced acceptor moieties ($MV^{+\bullet}$) were generated, the reduced acceptors were observed to preferentially form diamagnetic π -dimer form $(MV^+)_2$. Moreover, the back electron transfer (**BET**) events are significantly suppressed as a result of enhancement of electron migration (**EM**) within the dodeca-viologen frameworks. Importantly, these multi-electron-storage system based on **PCS**s can be used for the promotion of photocatalytic H_2 evolution in the presence of colloidal Pt as a catalyst.[13a]

In another recent work, Sakai group demonstrated that the rate of electron charging exhibits an intriguing quadratic dependence on the number of MV^{2+} units tethered to **PCS** (**[Ru(bpy)$_2$(4,4'-aspMV4)]$^{10+}$**, **[Ru(bpy)(4,4'-aspMV4)$_2$]$^{18+}$**, and **[Ru(4,4'-aspMV4)$_3$]$^{26+}$**, Figure 1), which is likely to govern the **EM** efficiency.[13b] It is important to note that, in these $Ru(bpy)_3^{2+}$-MV^{2+} hybrid systems, a direct linear correlation is observed between the rate of electron storage and the rate of H_2 evolution, indicating the importance of the electron storage abilities for the efficient light-driven water reduction using the **PCS**-based systems.[13]

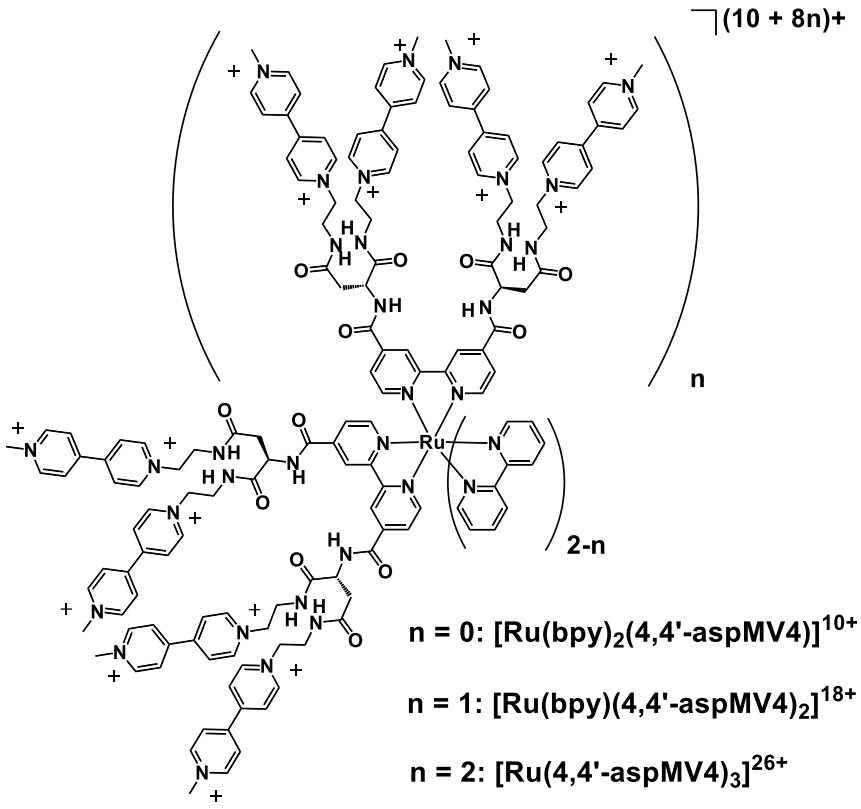

Figure 1. Molecular structures of some selected previously reported Ru-based **PCSs**.

On the other hand, in my previous study which focussed on the **[PtCl$_2$(bpyMV2)]$^{4+}$**, the relatively short distance between the bpy and the viologen acceptors in **bpyMV2^{4+}** ligand led to enhance the rate of electron transfer for both forward and backward processes.[12b] These findings evidence that the water reduction efficiency driven by **PCS** systems can be improved by the rational design of the **PCS** framework. Here, the synthesis and characterisation of a new Ru-based **PCS** having **bpyMV2^{4+}** ligand (**[Ru(bpyMV2)$_3$]$^{14+}$**, Figure 2) are reported in order to compare its photofunctional property with **[Ru(4,4'-aspMV4)$_3$]$^{26+}$**. In spite of such an apparently inferior electron transfer characteristic together with the drastic decrease in the number of acceptor units within the **PCS**, **[Ru(bpyMV2)$_3$]$^{14+}$** is found to exhibit somewhat higher photocatalytic performance, providing higher turnover number for **PCS** (TON_{PCS} = 231) compared with **[Ru(4,4'-aspMV4)$_3$]$^{26+}$** (TON_{PCS} = 161) and the non-hybrid system consisting of $[Ru(bpy)_3]^{2+}$ and MV^{2+} (6 equiv.) (TON_{PCS} = 73).

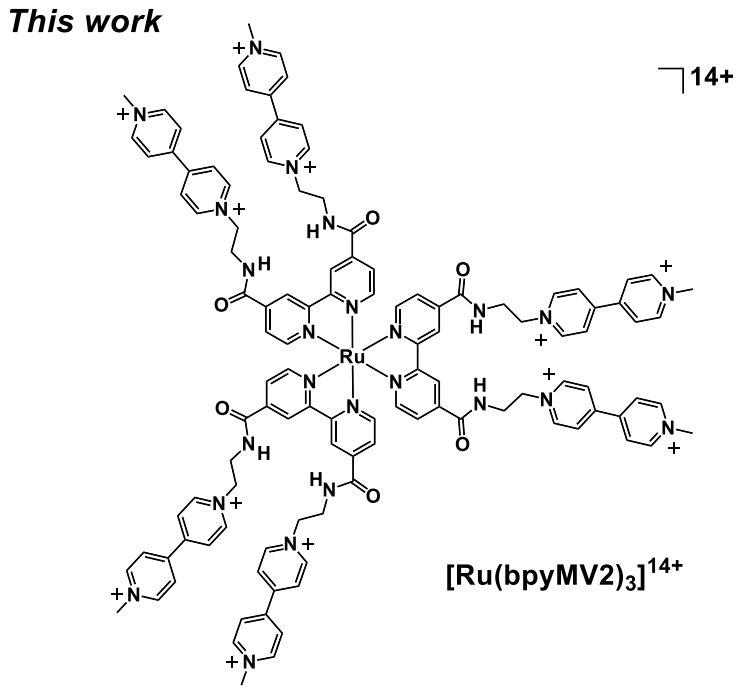

Figure 2. A molecular structure of **[Ru(bpyMV2)$_3$]$^{14+}$** studied in this work.

Experimental Section

Materials

PVP-protected colloidal Pt (2 nm in particle size) was purchased from Tanaka Holdings Co., Ltd. All other chemicals and solvents were purchased from Kanto Chemicals Co., Inc. and used without further purification. **[BpyMV2]**$(PF_6)_4$•$2H_2O$,[12b] *cis*-$RuCl_2(DMSO)_4$ (DMSO = dimethylsulfoxide),[14] $[Ru(bpy)_3](NO_3)_2$•$3H_2O$,[15] and $MV(NO_3)_2$[15] were synthesised as previously described.

Synthesis of $[Ru(bpyMV2)_3](PF_6)_{14}$•$7H_2O$

This was prepared by refluxing a solution of *cis*-$RuCl_2(DMSO)_4$ (18 mg, 0.037 mmol) and **[bpyMV2]**$(PF_6)_4$•$2H_2O$ (180 mg, 0.144 mmol) in a water-ethanol mixture (1 : 1 v/v, 7.5 mL) under Ar for 57 h, while the reaction was monitored spectrophotometrically. The solution was cooled to room temperature and followed by addition of ethanol (14 mL). The brown precipitate was collected by filtration. This crude product was redissolved in a water-acetone mixture (1 : 1 v/v, 4 mL) followed by addition of a saturated aqueous solution of NH_4PF_6 (0.3 mL). After removing acetone by evaporation under reduced pressure, the resulting solution was then cooled to 0 °C for 30 min to give a brown precipitate which was collected by filtration. The crude product was redissolved again in a water-acetone mixture (3 : 7 v/v, 5 mL) at 50 °C. This solution was left at room temperature overnight for the gradual evaporation of acetone. The final product, deposited as a red powder, was collected by filtration and dried in vacuo (yield: 92.2 mg, 59.7 %). ^{1}H NMR (CD_3CN/TMS, ppm): δ 8.93 (d, J = 6.2 Hz, 12H), 8.83 (d, J = 6.9 Hz, 12H), 8.79 (s, 6H), 8.38 (d, J = 6.9 Hz, 12H), 8.35 (d, J = 6.8 Hz, 12H), 7.80 (d, J = 5.5 Hz, 6H), 7.65 (br, 6H), 7.59 (dd, J = 5.7, 2.4 Hz, 6H), 4.83 (t, J = 5.5 Hz, 12H), 4.39 (s, 18H), 4.01 (m, 12H); Anal. Calcd for $C_{114}H_{114}F_{84}N_{24}O_6P_{14}Ru$•$7H_2O$ (4173.00): C, 32.81; H, 3.09; N, 8.06. Found: C, 32.95; H, 3.03; N, 8.09.

General Methods

UV-Vis and UV-Vis-NIR spectra were recorded on a Shimadzu UV-2450 and a Shimadzu UV-3600 spectrophotometer, respectively. Luminescence spectra were recorded on a Shimadzu RF5300PC spectrofluorophotometer. Emission decays were recorded on a HORIBA FluoroCube 3000USKU. The excitation source was a diode laser (472 nm) (HORIBA N-470L). Nanosecond laser flash photolysis experiments were carried out using a Unisoku TSP-1000M-03R system equipped with a Nd:YAG laser (Minilite II-10, Continuum, CA, USA) as a pump source and a 150 W Xe lamp (L2195, Hamamatsu) as a probe source. Transient absorption spectra were recorded using multichannel detector with a gated image-intensifer (C954603, Hamamatsu), while single-wavelength transient absorption traces were monitored using an amplified photomultiplier tube (R2949, Hamamatsu). ^{1}H NMR spectra were acquired on JEOL JNM-ESA 600 and JEOL JNM-ECS 400 spectrometers. Molar conductivity measurements were carried out at 20 °C in water using a TOA CM-20S conductometer with a TOA CG-511B conductivity cell having a cell constant of 0.969 cm^{-1}. Analysis of multi-step ion-pair formation equilibria was carried out based on published procedures.[15] Square wave voltammograms were recorded on a BAS ALS Model 602DKM electrochemical analyzer, using a three electrode system consisting of a platinum working electrode, a platinum wire counter electrode, and a Ag/Ag^{+} reference electrode (0.249 V vs. SCE), where TBAH (tetra(*n*-butyl)ammonium hexafluorophosphate) was used as a supporting electrolyte and all reported potentials are given relative to the Fc/Fc^{+} couple (Fc/Fc^{+} = 0.380 vs SCE).

Photolysis Experiments

The photoirradiation was carried out by an ILC Technology CERMAX LX-300 Xe lamp (300 W) equipped with a CM-1 cold mirror ($400 < \lambda < 800$ nm). Photolysis was carried out using Pyrex glass vials which eliminates the lights below ca. 350 nm. Other experimental details are all same to those reported elsewhere.[16]

Determination of the Main Reduced Forms during Photoirradiation

The relative abundances of electron-stored species in Table 9 are roughly estimated supposing that two-electrons stored within a **PCS** are always coupled to afford the $(MV^+)_2$ species. For either **PCS**, the relative abundances of three species are defined as x, y, and z, respectively, by also supposing eq. (1).

$$x + y + z = 100 \ (\%) \tag{1}$$

Next, the molar ratio of $MV^{+\bullet}$ and $(MV^+)_2$ (A) present in the whole system is defined by eq. (2),

$$A = \frac{ax + by + cz}{lx + my + nz} \tag{2}$$

where a, b, and c denote the number of $MV^{+\bullet}$ site involved in each species (i.e., 0 or 1), and l, m, and n denote the number of $(MV^+)_2$ sites (i.e., 0, 1, 2,…), as summarized in Table 9. With these definitions, the N_{ES} at the saturation can be defined by eq. (3).

$$N_{ES} = \frac{(a + 2l)x + (b + 2m)y + (c + 2n)z}{100} \tag{3}$$

We also note that only the selection of the three species listed in Table 9 for each **PCS** gave a reasonable solution to rationalize the observed phenomena.

Results and Discussion

Electrochemical properties

Complex **[Ru(bpyMV2)$_3$]$^{14+}$** was synthesised following the general procedure, as previously described.[13a] Electrochemical measurements carried out by the square-wave voltammetry (SWV) show that the first reduction and the first oxidation potentials are respectively located at -0.78 and 1.11 V vs. Fc/Fc^+ (Figure 3 and Table 1**)**. These are assignable to the $MV^{2+}/MV^{+\bullet}$ and Ru^{II}/Ru^{III} redox couples, respectively, and are similar to those observed for **[Ru(4,4'-aspMV4)$_3$]$^{26+}$**,[13a] indicating that the electronic interactions among the MV^{2+} moieties are negligible (Table 1). Importantly, the electron transfer efficiency between the $Ru(bpy)_3^{2+}$ core and the Pt electrode is lowered since the Ru core is spherically covered by the MV^{2+} moieties, as judged by the low responsiveness of anodic current with regard to the Ru^{II}/Ru^{III} couple.[13] On the other hand, the redox events associated to the $bpy/bpy^{-\bullet}$ and $MV^{+\bullet}/MV^0$ couples, are clearly overlapped in the range between -1 and -1.7 V vs. Fc/Fc^+. Therefore, deconvolution was carried out to determine all the potentials for the $bpy/bpy^{-\bullet}$ and $MV^{+\bullet}/MV^0$ couples. As can be seen in Figure 3, it is assumed that the second reduction of the MV^{2+} moieties (i.e., $MV^{+\bullet}/MV^0$) is observed as three different reduction events (-1.24, -1.40, and -1.57 V vs. Fc/Fc^+), presumably due to the presence of several different conformers in solution. This is in sharp contrast with the electrochemical behavior observed for **[Ru(4,4'-aspMV4)$_3$]$^{26+}$**, in which only a single peak derived from the $MV^{+\bullet}/MV^0$ reduction was observed at -1.25 V vs. Fc/Fc^+ with a higher intensity than the present system. The remaining three reductions at -1.30, -1.50, and -1.91 V vs. Fc/Fc^+ can be assigned to the $bpy/bpy^{-\bullet}$ couples, which are very close to those assigned for the **[Ru(4,4'-aspMV4)$_3$]$^{26+}$** system (-1.33, -1.49, and -1.92 V vs. Fc/Fc^+), indicating that the redox properties of the $Ru(bpy)_3^{2+}$ unit remain unchanged by tethering the MV^{2+} sites at shorter distance.

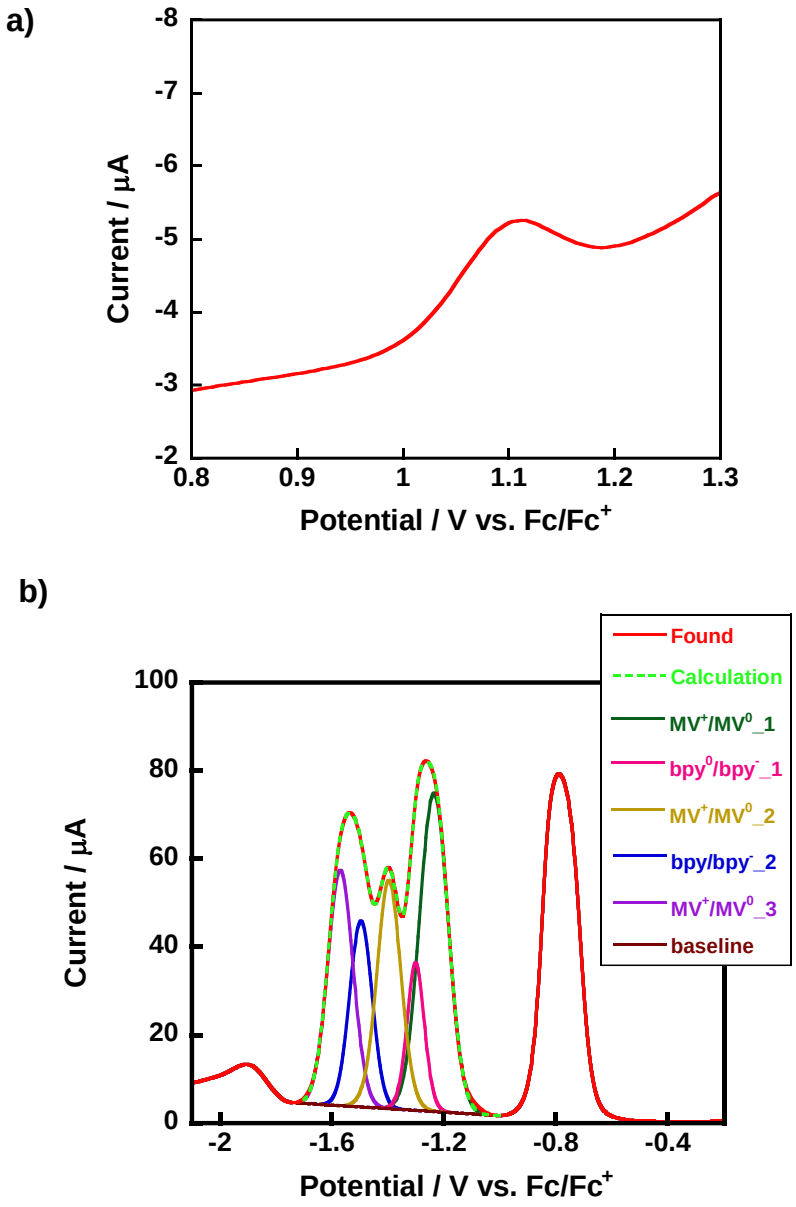

Figure 3. a) Oxidation and b) reduction waves for **[Ru(bpyMV2)$_3$](PF$_6$)$_{14}$**, observed using square wave voltammetry. Measurements were carried out for a 1 mM solution of the complex in acetonitrile containing 0.1 M tetra(*n*-butyl)ammonium hexafluorophosphate (TBAH) at room temperature under Ar atmosphere. The deconvolution was carried out for the potential range, where the reduction peaks of viologen and bpy are overlapped in the range between −1 and −1.7 V vs. Fc/Fc$^+$. The assignment of each peaks extracted by the spectral deconvolution was referenced from the results of **[Ru(4,4'-aspMV4)$_3$]$^{26+}$**.[13a]

Table 1. Redox potentials for **[Ru(bpyMV2)$_3$]$^{14+}$** and **[Ru(4,4'-aspMV4)$_3$]$^{26+}$**.

Complex		**[Ru(bpyMV2)$_3$]$^{14+}$**	**[Ru(4,4'-aspMV4)$_3$]$^{26+}$**[e]
Oxidation[a]	$E_{Ru,1}$	1.11	1.10
Reduction[a]	$E_{MV,1}$[b]	-0.78	-0.78
	$E_{MV,2}$[c]	-1.24	-1.25
	$E_{bpy,1}$[d]	-1.30	-1.33
	$E_{MV,3}$[c]	-1.40	
	$E_{bpy,2}$[d]	-1.50	-1.49
	$E_{MV,4}$[c]	-1.57	
	$E_{bpy,3}$[d]	-1.91	-1.92

[a] Potentials are given in volts vs. Fc/Fc^+ (The voltammograms are shown in Figure 3). The assignment of each peak was referenced from the results of **[Ru(4,4'-aspMV4)$_3$]$^{26+}$**.[13a] [b] Reduction for the $MV^{2+}/MV^{+\bullet}$ couple. [c] Reductions for the $MV^{+\bullet}/MV^0$ couples. [d] Reductions at the 2,2'-bipyridine moieties, where these reduction peaks are overlapped with those of the $MV^{+\bullet}/MV^0$ couples. [e] Values taken from reference 13a.

Ion-pair formation of the PCS with anionic species in solution

As noted below, one of the intrinsic features of the present **PCS** is the high positive charge (+14 for **[Ru(bpyMV2)$_3$]$^{14+}$**) which enables its effective electrostatic associations with anionic species, such as the dianionic form of EDTA (YH_2^{2-}; 93% abundance at pH 5.0).[17] To probe the ion-pair formation behavior of the **PCS** in solution, molar conductivity measurements were performed following the general procedure reported in the literature.[18] The molar conductivity shows a non-linear increase by decreasing the **PCS** concentration (Figure 4), which is attributable to the higher relative abundance of more highly charged species at lower **PCS** concentrations. By using published procedures, the relative abundances of major species in solution with a general formula $\{[Ru(bpyMV2)_3](PF_6)_n\}^{(14-n)+}$ are estimated as 16.9 % for n = 6, 22.8 % for n = 7, 21.8 % for n = 8, and 14.9 % for n = 9 at a total concentration of 0.04 mM (Tables 2-4, and Figure 5).[18] The speciation clearly shows the potential of **[Ru(bpyMV2)$_3$]$^{14+}$** for collecting multiple anionic species (e.g., YH_2^{2-}) in solution.[13,18]

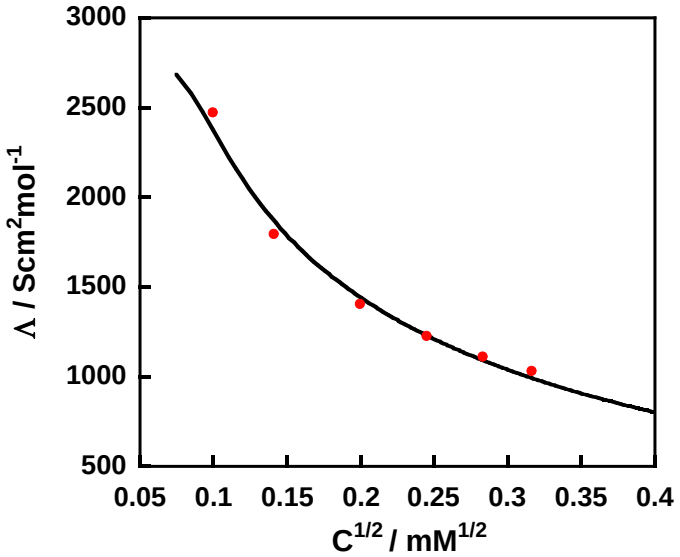

Figure 4. The observed and calculated molar conductivity (Λ) vs. the square root of the total concentration (C_t) of **[Ru(bpyMV2)$_3$]**$(PF_6)_{14}$. The black line shows the fitting based on our published method.[18]

Table 2. The observed molar conductivity of **[Ru(bpyMV2)$_3$]**$(PF_6)_{14}$ in water vs. the square root of the total concentration (C_t), measured in air at 20 °C.

$C_t^{1/2}$ ($mM^{1/2}$)	Λ (Scm^2mol^{-1})
0.3162	1033
0.2828	1113
0.2449	1229
0.1995	1407
0.1408	1796
0.09949	2475

Table 3. The α value, the stepwise formation constants (K_n), and the total stability constants (β_n) used to simulate the ion-pair formation behaviors shown in Figure 4, α is defined as $\alpha = K_n/K_{n-1}$ and is approximated to be constant; see ref. 18.

Params	Values
α	0.71
K_1 (β_1)	40000 (40000)
K_2 (β_2)	28400 (1.14×10^9)
K_3 (β_3)	20160 (2.29×10^{13})
K_4 (β_4)	14320 (3.28×10^{17})
K_5 (β_5)	10170 (3.33×10^{21})
K_6 (β_6)	7217 (2.41×10^{25})
K_7 (β_7)	5124 (1.23×10^{29})
K_8 (β_8)	3638 (4.48×10^{32})
K_9 (β_9)	2583 (1.16×10^{36})
K_{10} (β_{10})	1834 (2.12×10^{39})
K_{11} (β_{11})	1302 (2.77×10^{42})
K_{12} (β_{12})	942.5 (2.56×10^{45})
K_{13} (β_{13})	656.4 (1.68×10^{48})
K_{14} (β_{14})	466.0 (7.82×10^{50})

Table 4. The relative abundances of the chemical species derived from **[Ru(bpyMV2)$_3$]**$(PF_6)_{14}$ under the conditions adopted in photochemical H_2 evolution studies, where the formation constants listed in Table 3 are used to estimate the values listed in this table. A^{14+} denotes **[Ru(bpyMV2)$_3$]$^{14+}$** and X^- denotes PF_6^-.

Chemical species	C_t = 0.04 mM
A^{14+}	0.00209
AX^{13+}	0.0220
AX_2^{12+}	0.165
AX_3^{11+}	0.877
AX_4^{10+}	3.31
AX_5^{9+}	8.87
AX_6^{8+}	16.9
AX_7^{7+}	22.8
AX_8^{6+}	21.8
AX_9^{5+}	14.9
AX_{10}^{4+}	7.19
AX_{11}^{3+}	2.47
AX_{12}^{2+}	0.601
AX_{13}^{+}	0.104
AX_{14}	0.0127

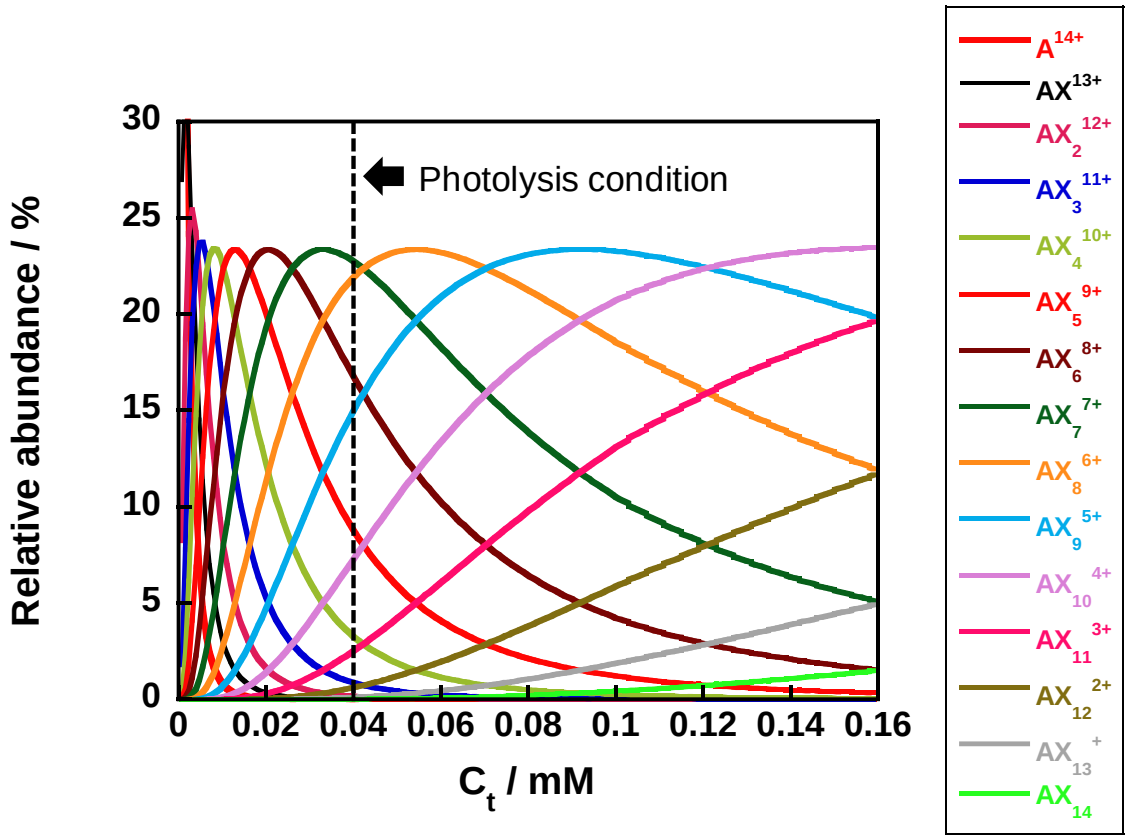

Figure 5. Relative abundances of the $AX_m^{(z-m)+}$ species (A^{14+} = **[Ru(bpyMV2)$_3$]$^{14+}$**, X^- = PF_6^-, m = 1, 2, 3, ...) vs. C_t are calculated for **[Ru(bpyMV2)$_3$]**$(PF_6)_{14}$ using the parameters determined for Figure 4 (see Table 4 for details).

Photo-driven forward and backward electron transfer processes in the PCS

The UV-Vis spectrum of **[Ru(bpyMV2)$_3$]$^{14+}$** shows a metal-to-ligand charge transfer (^{1}MLCT) band, characteristic of the Ru^{II}(bpy)$_3^{2+}$ chromophore, at 467 nm (ε = 23600 M^{-1} cm^{-1}) (Figure 6), as reported for the **[Ru(4,4'-aspMV4)$_3$]$^{26+}$** system (468 nm). Additionally, the spectral features at 254 nm (ε = 148000 M^{-1} cm^{-1}) and 305 nm (ε = 82000 M^{-1} cm^{-1}) are attributable to the viologen and bpy-based π- π^* transitions, respectively.[13,18]

Figure 7 shows possible schemes for the formation of **CS** states in **[Ru(bpyMV2)$_3$]$^{14+}$**; oxidative and reductive quenching paths (i.e., **OQ** and **RQ** paths). The emission spectrum of this system is characterised by a weak emission from the triplet (^{3}MLCT state) around 630 nm (Figure 8), because of the intramolecular forward electron transfer (**FET**) (i.e., FET(1)) from the Ru^{III}(bpy)$_2$(bpy$^{-\bullet}$)$^{2+}$ unit to one of the MV^{2+} acceptors (i.e., **OQ** path in Figure 7**,** left cycle).[13a] This gives rise to a **CS** state (CS(1)), formally expressed as [Ru^{III}(bpy)$_3$-(MV$^{+\bullet}$)(MV^{2+})$_5$]$^{14+}$. However, in the presence of EDTA, the dominant YH$_2^{2-}$ dianion forms ion-pair with the highly charged **PCS**, leading to the predominant promotion of **RQ** within the adduct rather than to promote **OQ**. The product in **RQ** then undergoes a **FET** forming a [Ru^{II}(bpy)$_3$-(MV$^{+\bullet}$)(MV^{2+})$_5$]$^{13+}$--EDTA$^{+\bullet}$ adduct (Figure 7, right cycle).

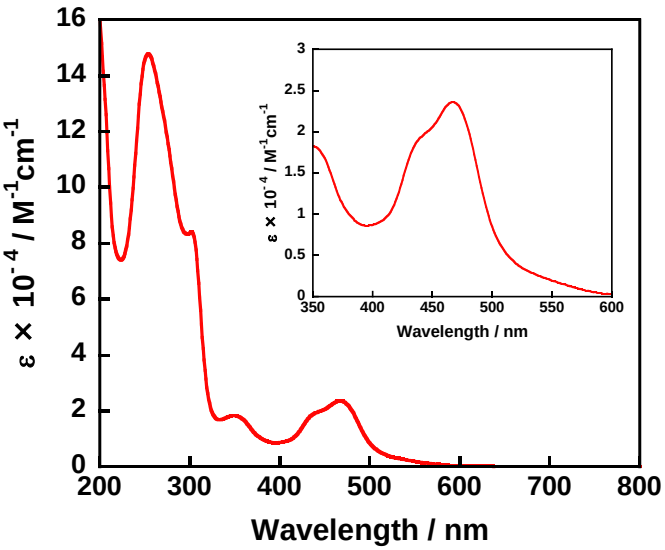

Figure 6. An absorption spectrum of **[Ru(bpyMV2)$_3$]**(PF$_6$)$_{14}$ in water at 20 °C. The inset shows a magnification in the range 350-600 nm. The molar absorptivities at 254 and 467 nm have been determined as 148000 and 23600 M^{-1} cm^{-1}, respectively.

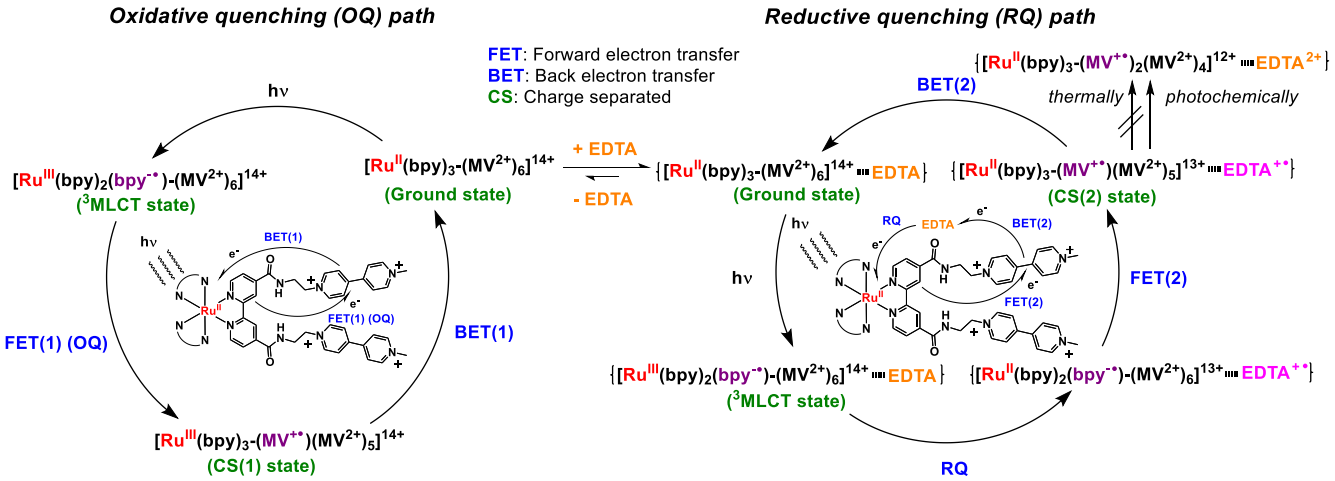

Figure 7. Photoinduced electron transfer processes in **PCSs** via (*left*) oxidative quenching (**OQ**) path and (*right*) reductive quenching (**RQ**) path.

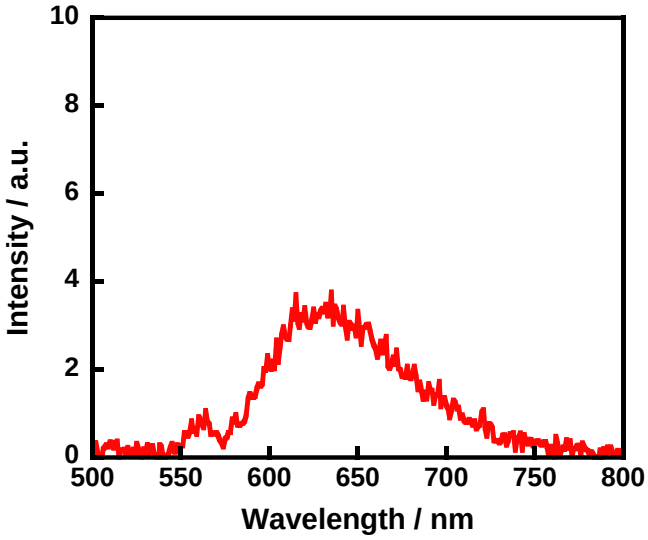

Figure 8. An emission spectrum recorded for an aqueous acetate buffer solution (0.1 M, pH 5.0) of **[Ru(bpyMV2)$_3$]**$(PF_6)_{14}$ at 20 °C under Ar. The excitation wavelength was 470 nm and the solution had 0.05 of absorbance at 470 nm.

In order to deepen understanding it was then decided to evaluate the time constants for the FET(1) events by measuring the emission decay profile of **[Ru(bpyMV2)$_3$]$^{14+}$**. It is composed of two decay components (Figure 9) indicative of the presence of two major conformers showing the individual decay lifetimes; τ_1 = 8.63 ns (67.4 %) and τ_2 = 12.6 ns (32.6 %) (the values in parenthesis are the relative abundance) (Table 5). In contrast, three different decay components are observed for **[Ru(4,4'-aspMV4)$_3$]$^{26+}$**, presumably due to the different number of MV^{2+} units and their different conformational distribution (Table 5). From the net time constant $< \tau >$ = 10.3 ns (see the footnote in Table 5 for detailed information), the net FET(1) rate (k_{ET}) for **[Ru(bpyMV2)$_3$]$^{14+}$** is estimated to be k_{ET} = 9.71 × 10^7 s^{-1}, which is slightly higher than that previously observed for **[Ru(4,4'-aspMV4)$_3$]$^{26+}$** (k_{ET} = 6.50 × 10^7 s^{-1}) (Table 5).[13a] However, it seems that shortening in the distance between the chromophore and the electron acceptors does not have an important effect on the increase in the FET(1) rate, although such a distance dependence on k_{ET} was observed for the related Pt^{II} systems.[12a-b]

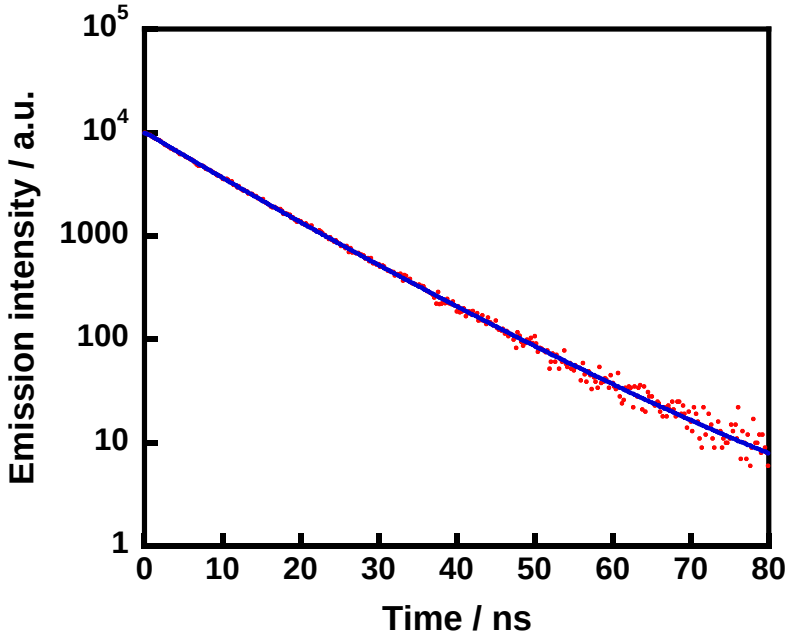

Figure 9. An emission decay profile after the laser pulse excitation at 472 nm of an aqueous acetate buffer solution (0.1 M, pH 5.0) containing **[Ru(bpyMV2)$_3$]**$(PF_6)_{14}$ at 20 °C under Ar. The emission was monitored at 630 nm. The blue dots show a calculated one according to a double exponential function.

Table 5. Time constants of FET and net FET rates from emission decay profiles measured in an aqueous acetate buffer solution (0.1 M, pH 5.0), at 20 ºC under Ar.

Constants	**[Ru(bpyMV2)$_3$]$^{14+}$**	**[Ru(4,4'-aspMV4)$_3$]$^{26+}$**[d]
Time constants for FET(1)[a]	τ_1 = 8.63 [ns] (67.4 %) τ_2 = 12.6 [ns] (32.6 %)	τ_1 = 2.72 [ns] (13.1 %) τ_2 = 10.9 [ns] (71.0 %) τ_3 = 25.2 [ns] (15.9 %)
Net time constant for FET(1)[b]	$<\tau>$ = 10.3 [ns]	$<\tau>$ = 15.4 [ns][e]
Net FET(1) rate[c]	$<k_{ET}>$ = 9.71 × 10^7 [s^{-1}]	$<k_{ET}>$ = 6.50 × 10^7 [s^{-1}][e]

[a] Estimated from the emission decay at 630 nm. [b] Each net time constant ($<\tau>$) was estimated using a definition of $<\tau> = \Sigma\ a_i\tau_i^2 / \Sigma\ a_i\tau_i$, where a_i is the relative contribution of the corresponding lifetime τ_i.[19] [c] $<k_{ET}> = 1/<\tau>$. [d] Values taken from reference 13a. [e] Estimated from the values reported in reference 13a.

Additional experiments were conducted with nanosecond transient absorption spectroscopy (TAS) to analyze the rate of back electron transfer from the $MV^{+\bullet}$ to the Ru^{III} core (BET(1)) that occurs after the **OQ**-based charge separation (Figure 7, left cycle). Laser pulse excitation at 532 nm of an aqueous solution of **[Ru(bpyMV2)$_3$]$^{14+}$** causes a slight increase in absorbance at 400 nm which appears overlapped with the peak of the ^{3}MLCT state of the Ru chromophore, and corresponds to the formation of one-electron-reduced $MV^{+\bullet}$ moieties (Figure 10a). This corroborates that the photoexcitation of **[Ru(bpyMV2)$_3$]$^{14+}$** leads to the CS(1) state. From the time profile of transient absorption changes at 400 nm (Figure 11), the lifetimes of the CS(1) state ($\tau_{C\ S,1}$- $\tau_{CS,3}$) were extracted (Table 6). The shorter-lived decay component has major contribution (53.3 %) and can be assigned to the Ru ^{3}MLCT state ($\tau_{e\ m}$). Accordingly, from the CS(1) lifetimes, the net rate constant of BET(1) ($<k_{BET}>$) can be estimated as 4.40 × 10^6 s^{-1} (Table 6). It is important to highlight that this value is around 2.9-fold times higher than that previously determined for **[Ru(4,4'-aspMV4)$_3$]$^{26+}$** ($<k_{BET}>$ = 1.54 × 10^6 s^{-1}), indicating that the BET(1) is strongly promoted by shortening the distance between the Ru chromophore and the MV^{2+} units.

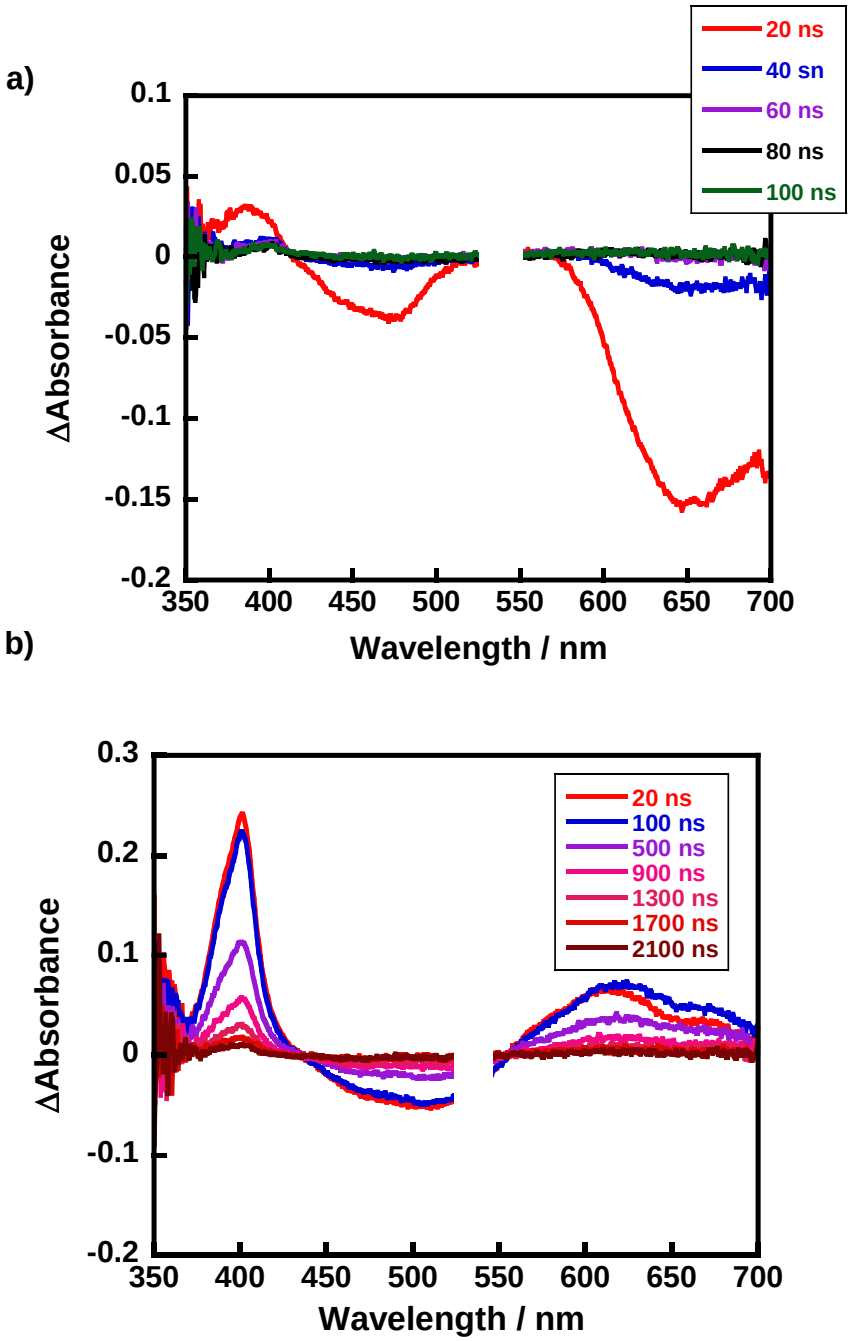

Figure 10. Transient absorption spectral changes observed after laser pulse excitation at 532 nm for an aqueous acetate buffer solution (0.1 M, pH 5.0) of **[Ru(bpyMV2)$_3$]**$(PF_6)_{14}$ (0.02 mM) in the a) absence and b) presence of EDTA (Na_2YH_2) under Ar atmosphere at room temperature. The inset in a) shows a magnification in the range 350-420 nm.

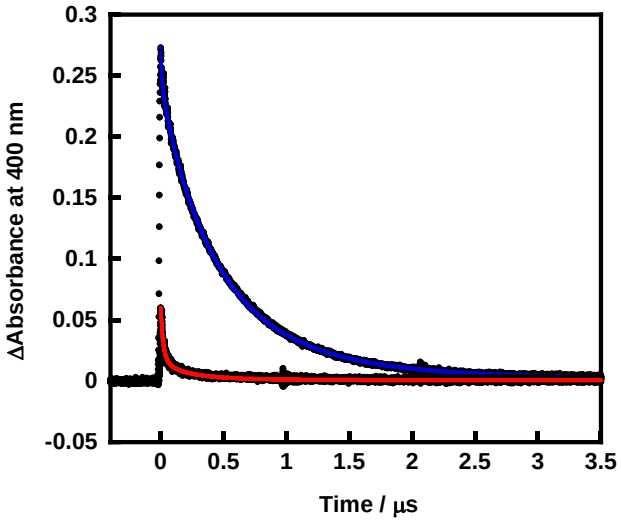

Figure 11. Transient absorption profiles at 400 nm observed after laser pulse excitation at 532 nm of an aqueous acetate buffer solution (0.1 M, pH 5.0) containing 0.02 mM of **[Ru(bpyMV2)3]**$(PF_6)_{14}$ in the absence (red dot) and the presence (blue dot) of 30 mM EDTA (Na_2YH_2).

Table 6. CS lifetimes and net BET rates estimated from transient absorption measured in an aqueous acetate buffer solution (0.1 M, pH 5.0), at 20 ºC under Ar.

Constants	**$[Ru(bpyMV2)_3]^{14+}$**	**$[Ru(4,4'\text{-}aspMV4)_3]^{26+}$**[d]
In the absence of EDTA		
CS(1) lifetimes[a]	τ_{em} = 16.1 [ns] (53.3 %) $\tau_{CS,1}$ = 37.8 [ns] (20.6 %) $\tau_{CS,2}$ = 143 [ns] (11.9 %) $\tau_{CS,3}$ = 328 [ns] (14.2 %)	τ_{em} = 43.3 [ns] (38.9 %) $\tau_{CS,1}$ = 264 [ns] (26.9 %) $\tau_{CS,2}$ = 502 [ns] (29.2 %) $\tau_{CS,3}$ = 1.46 [μs] (5.0 %)
Net CS(1) lifetime[b]	$<\tau>$ = 227 [ns]	$<\tau>$ = 650 [ns]
Net BET(1) rate[c]	$<k_{BET}>$ = 4.40 × 10^6 [s^{-1}]	$<k_{BET}>$ = 1.54 × 10^6 [s^{-1}]
In the presence of EDTA		
CS(2) lifetimes[a]	τ_{em} = 6.43 [ns] (9.07 %) $\tau_{CS,1}$ = 59.8 [ns] (4.38 %) $\tau_{CS,2}$ = 371 [ns] (52.6 %) $\tau_{CS,3}$ = 783 [ns] (33.2 %) $\tau_{CS,4}$ = 1.89 [μs] (0.69 %)	$\tau_{CS,1}$ = 242 [ns] (26.9 %) $\tau_{CS,2}$ = 624 [ns] (30.5 %) $\tau_{CS,3}$ = 1.43 [μs] (42.6 %)
Net CS(2) lifetime[b]	$<\tau>$ = 638 [ns]	$<\tau>$ = 1.05 [μs]
Net BET(2) rate[c]	$<k_{BET}>$ = 1.57 × 10^6 [s^{-1}]	$<k_{BET}>$ = 9.52 × 10^5 [s^{-1}]

[a] Estimated from the transient absorption decays at 400 nm. [b] Each net CS lifetime ($<\tau>$) was estimated using a definition of $<\tau> = \Sigma\ a_i\tau_i^2 / \Sigma\ a_i\tau_i$, where a_i is the relative contribution of the corresponding lifetime τ_i.[19] [c] $<k_{BET}> = 1/<\tau>$. [d] Values taken from reference 13a.

Nevertheless, the yield of $MV^{+\bullet}$ in the presence of EDTA is clearly enhanced as judged by the increase in the maximum absorbance at 400 nm (about 4.5 times) compared to that observed in the absence of EDTA (Figures 10b and 11). This observation demonstrates the excellent capability of the highly positively charged **[Ru(bpyMV2)$_3$]$^{14+}$** system to collect the anionic YH_2^{2-} species by forming ion-pair adducts so that reductive quenching is strongly enhanced to give the charge-separated state $[Ru^{II}(bpy)_2(bpy^{-\bullet})\text{-}(MV^{2+})_6]^{13+}$--$EDTA^{+\bullet}$, followed by intramolecular electron transfer to give $[Ru^{II}(bpy)_3\text{-}(MV^{+\bullet})(MV^{2+})_5]^{13+}$--$EDTA^{+\bullet}$ (CS(2) state). The dramatic enhancement in the **CS** yield by the presence of EDTA also indicates that the reductive quenching is highly predominant and the CS(2) state is major in the presence of EDTA in high concentrations. To the contrary, the smaller increase in the CS yield (about 3.1) observed in **[Ru(4,4'-aspMV4)$_3$]$^{26+}$** suggests a more contribution of the **OQ** path in **CS** formation for the electron storage, which is also supported by the lower BET(1) rate (3 times lower compared to that of **[Ru(bpyMV2)$_3$]$^{14+}$**). On the other hand, as it can be seen in Table 6, the CS(2) lifetime of the present **PCS** is composed by five decay components: τ_{em} = 6.43 ns (9.07 %), τ_1 = 59.8 ns (4.38 %), τ_2 = 371 ns (52.6 %), τ_3 = 783 ns (33.2 %), and τ_4 = 1.89 ns (0.69 %) (the values in parenthesis are the relative contribution of each component). The shortest-lived component (τ_{em}) is assignable to the decay of the ^{3}MLCT state ($[Ru^{II}*(bpy)_3\text{-}(MV^{2+})_6]^{14+}$--EDTA → $[Ru^{II}(bpy)_3\text{-}(MV^{2+})_6]^{14+}$--EDTA), even in the presence of EDTA. The fact that the triplet component is absent in **[Ru(4,4'-aspMV4)$_3$]$^{26+}$** can be rationalized by a slightly more efficient electron injection from EDTA to the excited chromophore, due to its higher ability to form ion-pair adducts (higher positive charge compared to **[Ru(bpyMV2)$_3$]$^{14+}$**). Moreover, the higher number of MV^{2+} moieties leading to the more frequent collision of them in the **[Ru(4,4'-aspMV4)$_3$]$^{26+}$** system. This feature facilitates the electron migration within the MV^{2+} skeleton, leading to the decrease in the probability of back electron transfer to the EDTA (longer CS(2) state lifetime (1.05 μs) compared to that of **[Ru(bpyMV2)$_3$]$^{14+}$** (783 ns)) (Table 6).

In addition, it is noted that, in the present **PCS** system, the TA decay profile displays nearly quantitative recovery of the ground state species (Figure 11), proving that recombination of the charge-separated state (i.e., BET(2)) proceeds quantitatively under these experimental conditions ($[Ru^{II}(bpy)_3\text{-}(MV^{+\bullet})(MV^{2+})_5]^{13+}$--$EDTA^{+\bullet}$ → $[Ru^{II}(bpy)_3\text{-}(MV^{2+})_6]^{14+}$--EDTA). Therefore, the transfer and storage of two electrons over the multi-viologen frameworks can only be achieved by two consecutive light absorption processes at each single $Ru^{II}(bpy)_3^{2+}$ chromophore.

Photo-driven multi-electron storage behaviour

Next, I focus on the photodriven multi-electron storage properties of **[Ru(bpyMV2)$_3$]$^{14+}$**. As previously reported, the multi-electron storage behavior can be monitored by absorption spectroscopy.[12,13,20] Visible light irradiation (800 > λ > 400 nm) of an aqueous solution of **[Ru(bpyMV2)$_3$]$^{14+}$** at pH 5.0 in the presence of 30 mM EDTA results in growth of new bands in the visible to near infrared (NIR) region as a direct consequence of one-electron reduction of MV^{2+} acceptor sites (Figure 12a). The bands located at 358, 527, and 868 nm are assigned as those derived from the diamagnetic $(MV^{+})_2$ π -dimer in which the two $MV^{+\bullet}$ moieties stacked intramolecularly in a staggered fashion, as previously described for this **bpyMV2^{4+}** ligand.[12b] The net number of electrons stored per **PCS** (N_{ES}) and the relative abundances of the $MV^{+\bullet}$ and $(MV^{+})_2$ components at each irradiation time can be determined by spectral deconvolution analysis using published procedures (Figures 12b, 13, 14, 15, Tables 7 and 8).[20] At the saturation stage (at 60 min), **[Ru(bpyMV2)$_3$]$^{14+}$** stores 3.3 electrons per **PCS**. This maximum N_{ES} is roughly a half of those observed for the dodeca-viologen tethered systems (N_{ES} = 7-8).[13a] Therefore, the electron filling yields within the frameworks (55-67%) are similar to those for the previous **PCS**s regardless of the total acceptor numbers. The important finding here is not the N_{ES} value but the relative abundance of non-dimerized $MV^{+\bullet}$, which is known to serve as a stronger reducing equivalent towards water reduction when compared with the dimerized species.[12b,21] For instance, the molar ratio of $MV^{+\bullet}$ and $(MV^{+})_2$ ($[MV^{+\bullet}]/[(MV^{+})_2]$ = 0.45) is substantially higher than that observed for the **[Ru(4,4'-aspMV4)$_3$]$^{26+}$** system (0.14) (Table 8),[13a] revealing much lower preference to form the $(MV^{+})_2$ dimer relative to the previous **PCS**s.

From the time course of N_{ES} depicted in Figure 4b, the initial rate of electron storage ($Rate_{ES}$; $2e^{-}$ h^{-1}), which is defined as the number of two-electron storage cycles per **PCS** per hour, can be estimated as 91.3 $2e^{-}$ h^{-1}. This value is significantly lower than the value observed for **[Ru(4,4'-aspMV4)$_3$]$^{26+}$** (630 $2e^{-}$ h^{-1}).[13a] The lower $Rate_{ES}$ value observed in the present system agrees with my finding that the probability of **BET** events are significantly promoted by decreasing the probability of **EM** based on the decrease in the number of non-reduced MV^{2+} sites surrounding the one-electron-reduced $MV^{+\bullet}$ moieties.

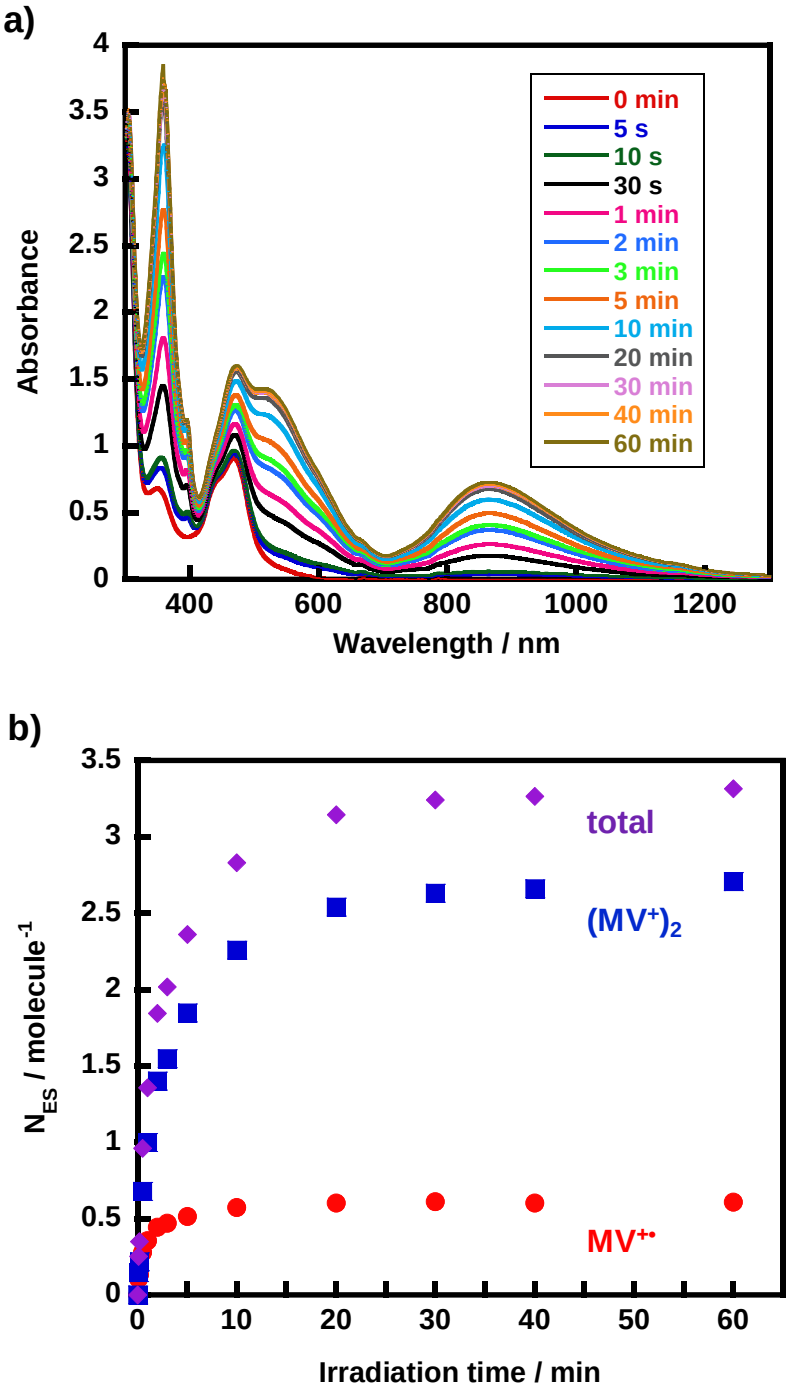

Figure 12. a) Spectral changes during the photolysis of an aqueous acetate buffer solution (0.1 M, pH = 5.0) containing 30 mM EDTA (Na_2YH_2) in the presence of 0.04 mM **[Ru(bpyMV2)$_3$]**$(PF_6)_{14}$ at 20 °C under Ar atmosphere. b) The time course of the total N_{ES} for **[Ru(bpyMV2)$_3$]$^{14+}$** together with those derived from the individual $MV^{+\bullet}$ and $(MV^{+})_2$ components.

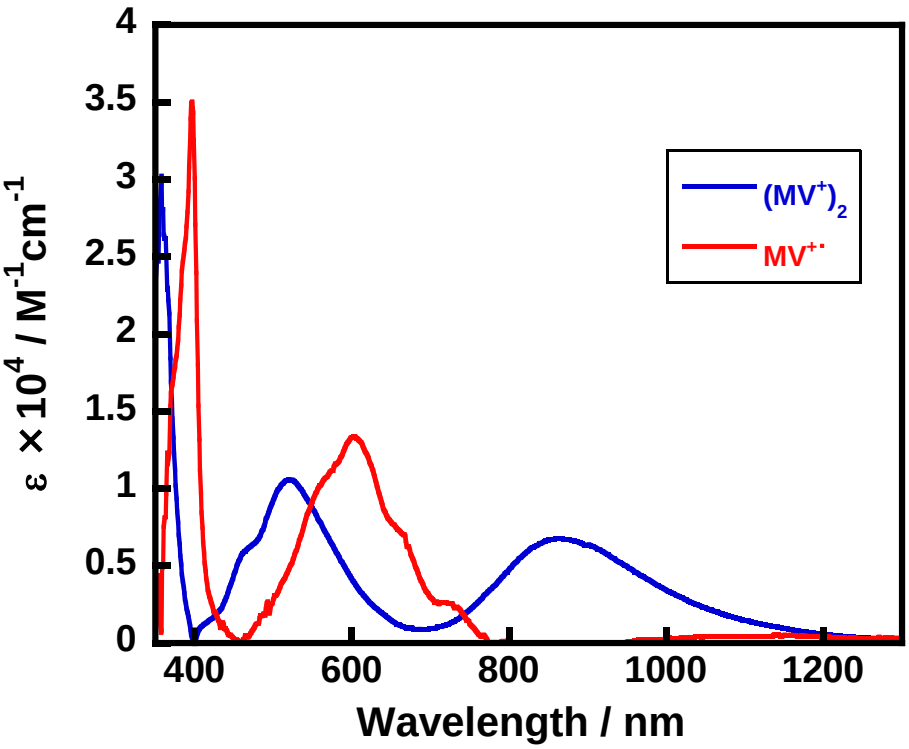

Figure 13. Two spectral components extracted in spectral deconvolution analysis. All spectra observed during multi-charge storage can be expressed as the sum of two spectral components arising from $MV^{+\bullet}$ and $(MV^{+})_2$, with a definition of Abs(w, t) = $C_m(t)\varepsilon_m(w) + C_d(t)\varepsilon_d(w)$, where Abs is absorbance, C_m and C_d are molar concentrations of $MV^{+\bullet}$ and $(MV^{+})_2$, respectively, ε_m and ε_d are molar absorptivities of $MV^{+\bullet}$ and $(MV^{+})_2$, respectively, t is time, and w is wavelength. The original scans are those given in Figure 12a.

Table 7. Absorption maxima and molar absorptivities for $MV^{+\bullet}$ and $(MV^{+})_2$ sites generated in this system. The values are determined from the spectra shown in Figure 13, which were obtained by spectral deconvolution in Figures 14 and 15.

Species	λ_{abs} / nm	ε / $M^{-1}cm^{-1}$
$(MV^{+})_2$	358	30200
	524	10600
	866	6800
$MV^{+\bullet}$	397	35000
	604	13400

Table 8. The net concentrations of the $MV^{+\bullet}$ and $(MV^{+})_2$ sites generated over **[Ru(bpyMV2)$_3$]$^{14+}$** during the photolysis with EDTA (original spectral data in Figure 12a). Some relevant parameters are also listed.
*N_{ES} : Number of Electrons Stored

Irradiation time	$MV^{+\bullet}$ (μM)	$(MV^{+})_2$ (μM)	$MV^{+\bullet}$ (%)	$(MV^{+})_2$ (%)	N_{ES}* (molecule^{-1})	K_d ($\times 10^5$ M^{-1})
5 s	4.22	2.96	1.76	2.47	0.254	1.66
10 s	5.27	4.35	2.19	3.63	0.349	1.57
30 s	11.2	13.6	4.66	11.3	0.960	1.09
1 min	14.3	20.0	5.95	16.7	1.36	0.982
2 min	17.7	28.1	7.37	23.4	1.84	0.897
3 min	18.8	31.0	7.82	25.8	2.02	0.880
5 min	20.5	36.9	8.55	30.8	2.36	0.877
10 min	22.9	45.2	9.55	37.7	2.83	0.860
20 min	24.1	50.8	10.0	42.4	3.14	0.876
30 min	24.4	52.6	10.2	43.9	3.24	0.883
40 min	24.2	53.2	10.1	44.4	3.27	0.911
60 min	24.3	54.2	10.1	45.1	3.32	0.917

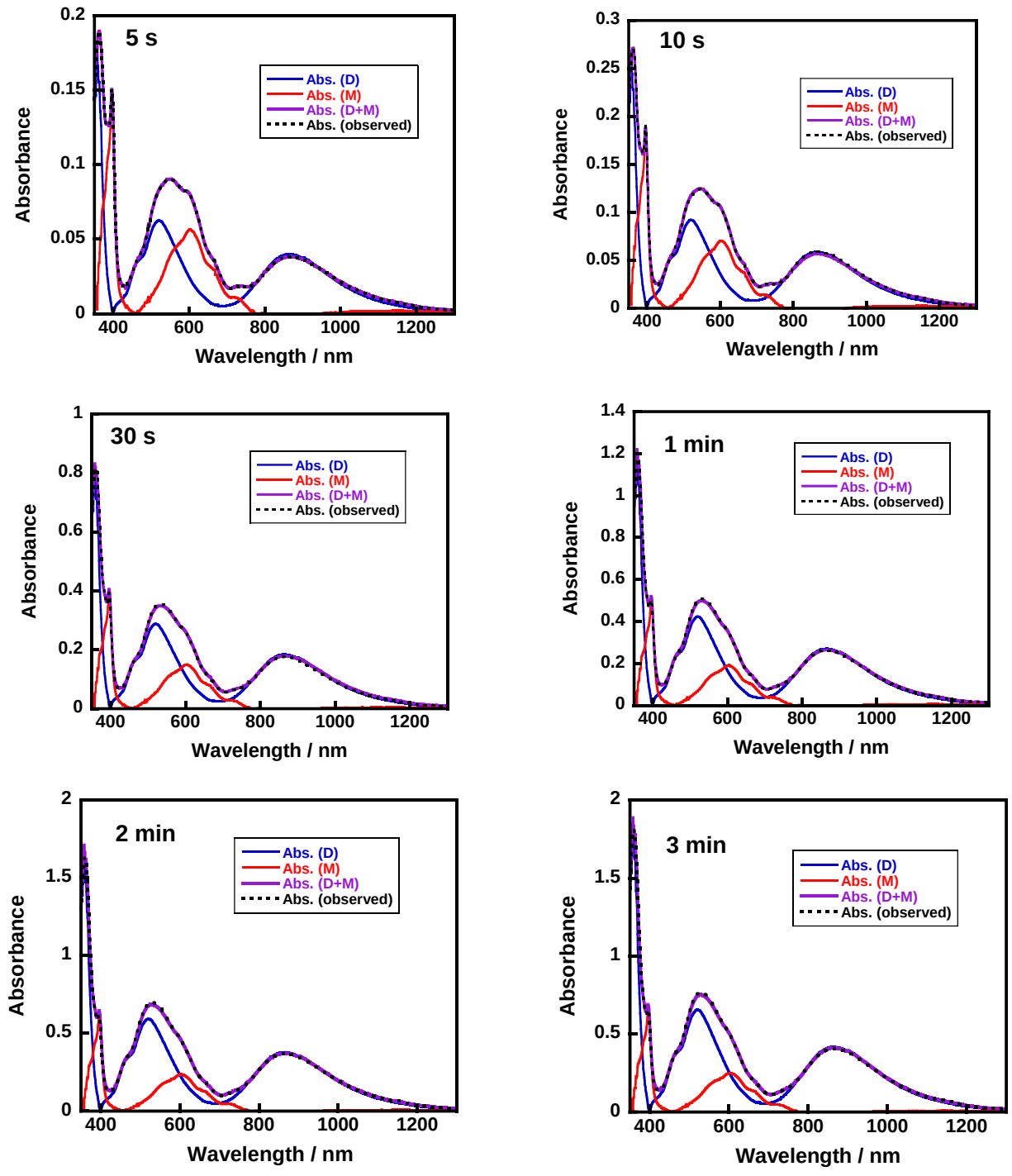

Figure 14. Deconvolution of spectral changes observed during the photolysis (0-3 min) of **[Ru(bpyMV2)$_3$]$^{14+}$**. The raw data were taken from those in Figure 12a, where the spectral component derived from the unphotolyzed charge separator was removed by subtraction. Each spectrum was fitted to the sum of two spectral components shown in Figure 13, the concentrations of $MV^{+\bullet}$ and $(MV^{+})_2$ were determined by the least-squares method implemented in the program of Sakai group.[20]

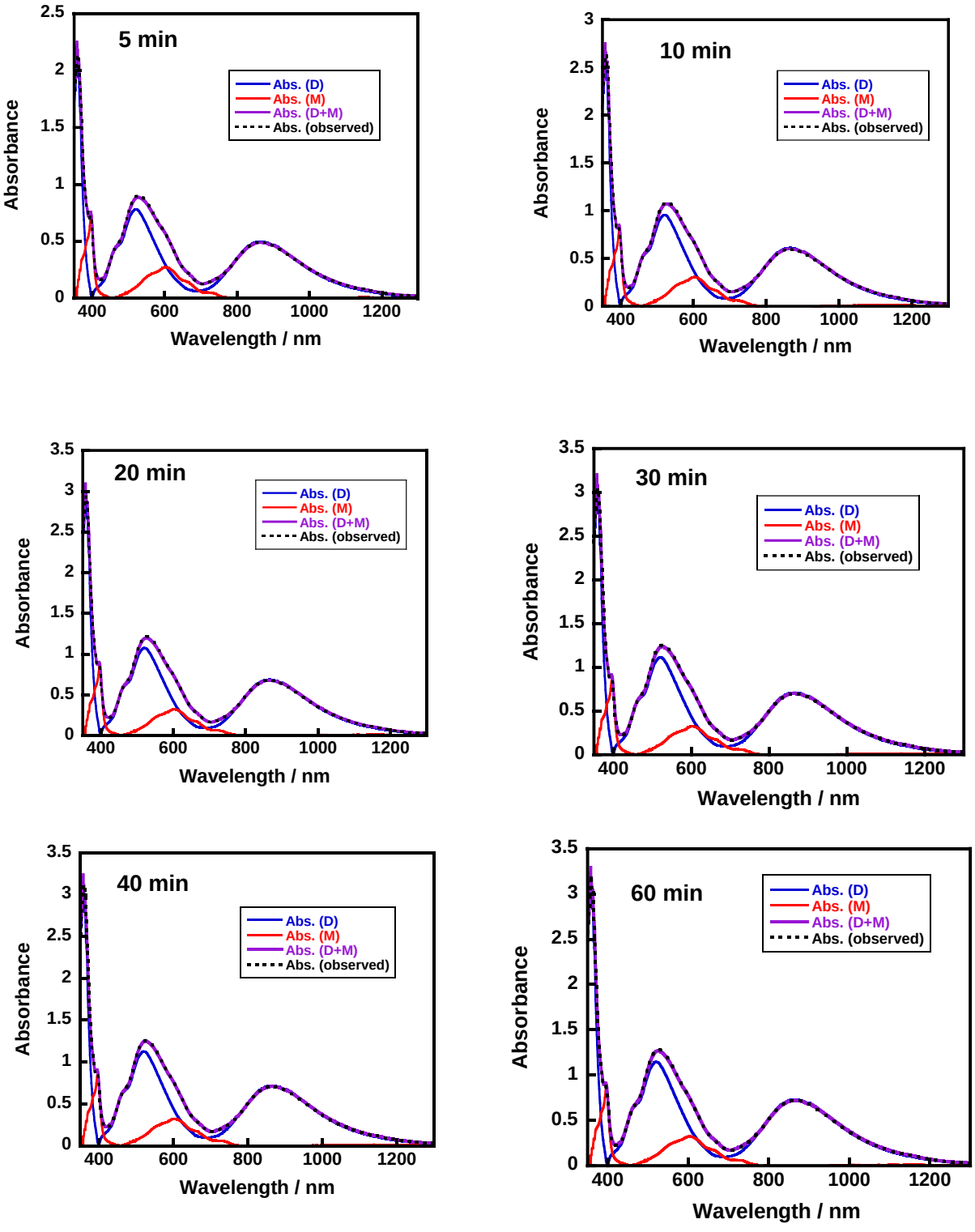

Figure 15. Deconvolution of spectral changes observed during the photolysis (5-60 min) of **[Ru(bpyMV2)$_3$]$^{14+}$**.

Furthermore, it is also important to pay attention to the lower efficiency of the present **PCS** in the storage of $MV^{+\bullet}$. The initial rates of $MV^{+\bullet}$ storage cycle per molecule per hour ($Rate_{MV+\bullet S}$; $MV^{+\bullet}$ h^{-1}) were estimated from the spectral changes for the two **PCS**s, showing that the $Rate_{MV+\bullet S}$ of **[Ru(bpyMV2)$_3$]$^{14+}$** (76.0 $MV^{+\bullet}$ h^{-1}) is lower than that observed for **[Ru(4,4'-aspMV4)$_3$]$^{26+}$** (189 $MV^{+\bullet}$ h^{-1}).[13a] However, the value of $Rate_{MV+\bullet S}/Rate_{ES}$ = 0.83 is much higher than that reported for **[Ru(4,4'-aspMV4)$_3$]$^{26+}$** ($Rate_{MV+\bullet S}/Rate_{ES}$ = 0.30). This also corroborates the relative preference in the formation of $MV^{+\bullet}$ radical during photoirradiation, which is considered to be the major cause of the higher H_2 evolution characteristics realized for the present **PCS** (*vide infra*).

Additionally, the relative abundances of reduced species at the saturation stage can be roughly estimated as $[Ru(bpy)_3\text{-}(MV^{2+})_4(MV^{+})_2]^{12+}$ ($2e^-$ reduced form: 3.5 %), $[Ru(bpy)_3\text{-}(MV^{2+})_3(MV^{+\bullet})(MV^{+})_2]^{11+}$ ($3e^-$ reduced form: 61 %), and $[Ru(bpy)_3\text{-}(MV^{2+})_2\{(MV^{+})_2\}_2]^{10+}$ ($4e^-$ reduced form: 36 %) (Table 9; Details are explained in Experimental Section). As can be seen in Table 4**,** the distribution of the reduced species is remarkably different from that estimated for **[Ru(4,4'-aspMV4)$_3$]$^{26+}$**. In the present **PCS**, by shortening the distance between the Ru chromophore and the MV^{2+} moieties, the self-quenching processes of the excited Ru chromophore such as electron transfer from $MV^{+\bullet}$ moieties or energy transfer to $(MV^{+})_2$ moieties are promoted, as previously discussed for **[PtCl$_2$(bpyMV2)]$^{4+}$**.[12b] This is likely to be the major cause of giving $[Ru(bpy)_3\text{-}(MV^{2+})_3(MV^{+\bullet})(MV^{+})_2]^{11+}$ ($3e^-$ reduced form) as the major species at the saturation stage. Therefore, it is expected that the self-quenching of the ^{3}MLCT state by the $(MV^{+})_2$ and $MV^{+\bullet}$ sites formed in the present system is also responsible for the much lower $Rate_{ES}$.

In addition to the above results, it was also tested the use of a neutral electron donor, TEOA (triethanolamine), instead of EDTA in order to ascertain the effect of ion-pair formation by the dianionic form of EDTA.[13a] As shown in Figure 16, a similar photolysis study conducted by employing TEOA causes much smaller changes in absorption in the visible to near-infrared domain than that observed with EDTA (Figure 12a), indicating that the ion-pair formation plays a major role in enhancing the reductive quenching required to drive the major photo-driven electron transfer events.[12,13]

Table 9. Rough estimates of the relative abundances of three major electron-stored species formed at the saturation stage when **[Ru(bpyMV2)$_3$]$^{14+}$** or **[Ru(4,4'-aspMV4)$_3$]$^{26+}$** was irradiated by visible light in the presence of EDTA without any catalyst.[a]

	Reduced form	Abundance[a]	Number of $MV^{+\bullet}$	Number of $(MV^+)_2$	A_{obs}[b]	A_{calc}[c]	$N_{ES,obs}$[b]	$N_{ES,calc}$[c]
[Ru(bpyMV2)$_3$]$^{14+}$	$2e^-$ $3e^-$ $4e^-$	3.5 % (x) 61 % (y) 36 % (z)	0 (a) 1 (b) 0 (c)	1 (l) 1 (m) 2 (n)	0.45	0.45	3.32	3.32
[Ru(4,4'-aspMV4)$_3$]$^{26+}$	$6e^-$ $7e^-$ $8e^-$	39 % (x) 44 % (y) 17 % (z)	0 (a) 1 (b) 0 (c)	3 (l) 3 (m) 4 (n)	0.14	0.14	6.78	6.78

[a] Definition of x, y, and z is given in Experimental Section. [b] Values estimated by spectral deconvolution (Table 8). [c] Values obtained by using eqs. (1)-(3).

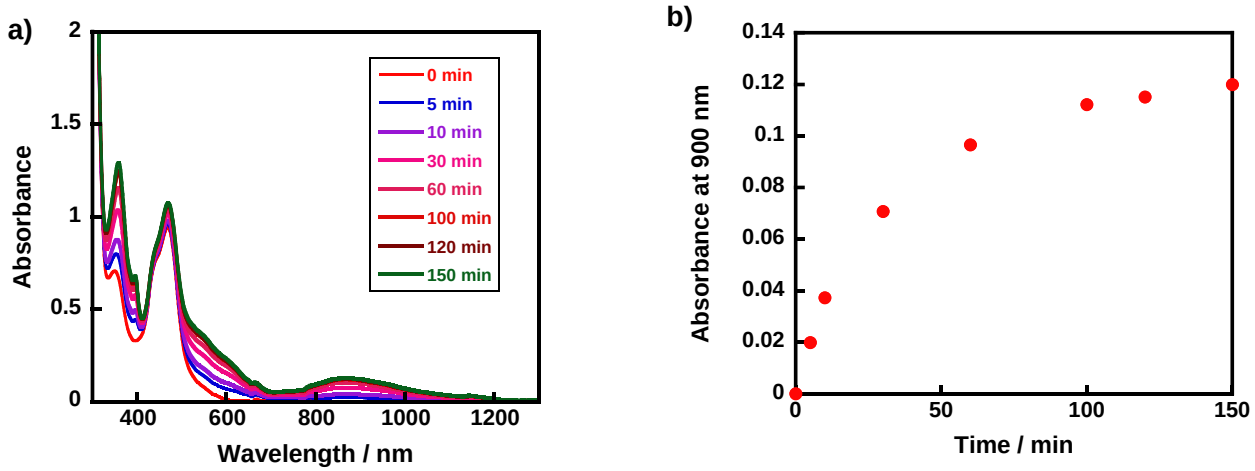

Figure 16. a) Spectral changes during the photolysis of an aqueous solution (pH = 7.0) containing 30 mM triethanolamine (TEOA) in the presence of **[Ru(bpyMV2)$_3$]**$(PF_6)_{14}$ at 20 °C under Ar atmosphere, where pH was adjusted with HCl. b) The time course of absorbance at 900 nm during the photolysis.

Photo-driven H_2 evolution using the PCS

Photochemical H_2 evolution promoted by **[Ru(bpyMV2)$_3$]$^{14+}$** (0.04 mM) was tested using PVP-protected colloidal Pt (nanoparticles, 2 nm in diameter; PVP = polyvinylpyrrolidone) (0.1 mM) as a catalyst in the presence of EDTA (30 mM) (Figures 17 and 18). Under these conditions, the initial rate in H_2 evolution (TOF_{PCS} = TON_{PCS} h^{-1}) is estimated as TOF_{PCS} = 128 h^{-1} and is comparable to that observed for **[Ru(4,4'-aspMV4)$_3$]$^{26+}$** (TOF_{PCS} = 157 h^{-1}). As mentioned above, the TOF_{PCS} values are directly proportional to the rate of two-electron charging.[13] However, the $Rate_{ES}$ observed for **[Ru(bpyMV2)$_3$]$^{14+}$** (91.3 $2e^-$ h^{-1}) is much lower than that of **[Ru(4,4'-aspMV4)$_3$]$^{26+}$** (630 $2e^-$ h^{-1}). As demonstrated in reported Pt^{II} system,[12b] the formation of $(MV^+)_2$ π -dimer species causes a loss in the driving force for H_2 evolution since the reduction potential of MV^{2+} is by 0.15 V shifted to the anodic side upon dimerization ($E_{1/2}((MV^+)_2/(MV^{2+})_2)$ = -0.55 V vs. SCE; $E_{1/2}(MV^{+\bullet}/MV^{2+})$ = -0.70 V vs. SCE).[21] As a result, in spite of the lower $Rate_{ES}$, the higher relative abundance of $MV^{+\bullet}$ in the **[Ru(bpyMV2)$_3$]$^{14+}$** system offers higher *net driving force* for H_2 evolution, leading to the TOF_{PCS} comparable to that observed for **[Ru(4,4'-aspMV4)$_3$]$^{26+}$**. Similar trends were also observed at pH 7 for the previous aspartic-acid-based systems where the increase in the $MV^{+\bullet}$ ratio led to the enhanced activity in water reduction.[13b] This argument is in good agreement with the higher activity observed with the non-hybrid system comprised of the non-derivatized $[Ru(bpy)_3]^{2+}$ chromophore with 6 equiv. of the free MV^{2+} (TOF_{PCS} = 158 h^{-1}), in which the major one-electron-reduced MV^{2+} form is the $MV^{+\bullet}$ species (see Figure 17b)

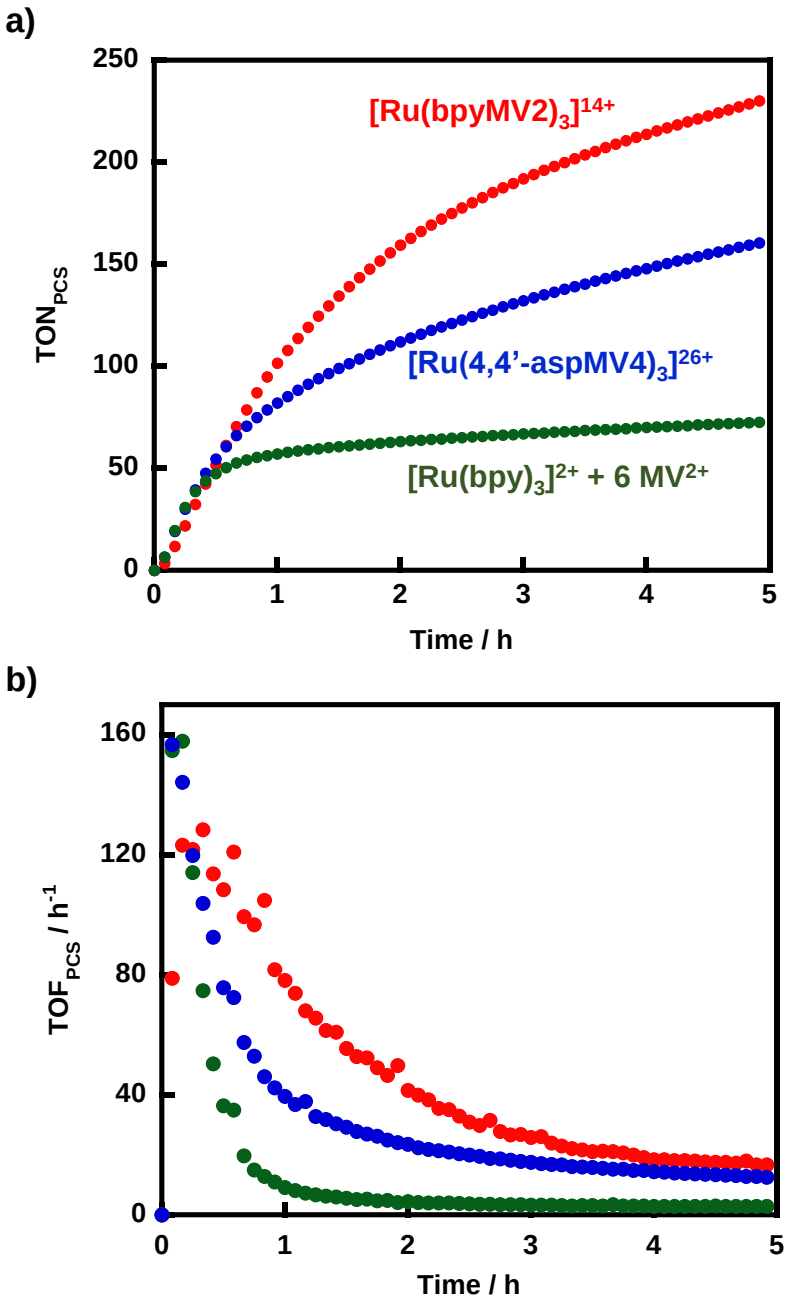

Figure 17. Time course of a) TON_{PCS} and b) TOF_{PCS} profiles for photochemical H_2 production from an aqueous acetate buffer solution (pH 5.0, 10 mL; at 20 °C under Ar) containing PVP-protected colloidal Pt (0.1 mM on the basis of the net Pt atom concentration) and EDTA (30 mM) in the presence of (red) 0.04 mM **[Ru(bpyMV2)$_3$]**$(PF_6)_{14}$, (blue) 0.04 mM **[Ru(4,4'-aspMV4)$_3$]**$(PF_6)_{26}$, or (green) 0.04 mM $[Ru(bpy)_3](NO_3)_2$ and 0.24 mM $MV(NO_3)_2$.

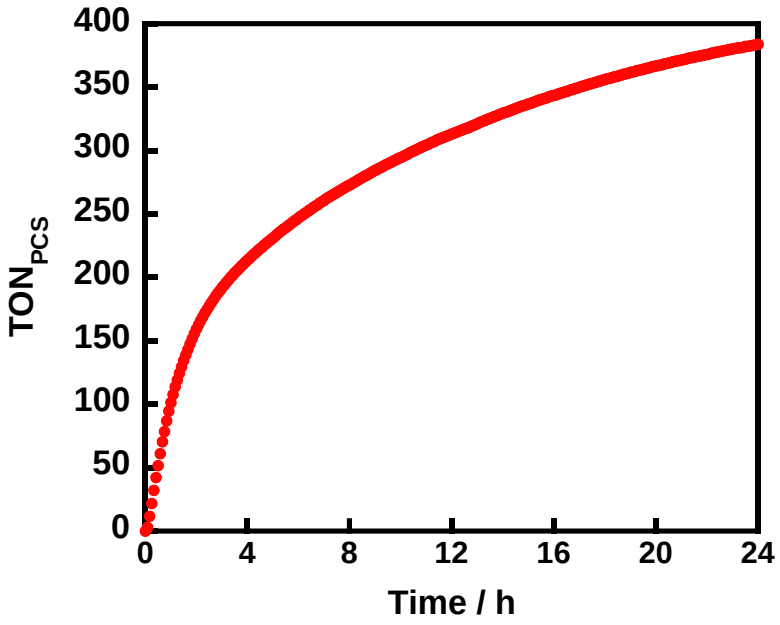

Figure 18. Photochemical H_2 production observed during the 24-h photoirradiation of an aqueous acetate buffer solution (pH 5.0, 10 mL; at 20 °C under Ar) containing PVP-protected colloidal Pt (0.1 mM on the basis of the net Pt atom concentration) and EDTA (30 mM) in the presence of 0.04 mM **[Ru(bpyMV2)$_3$]**$(PF_6)_{14}$.

On the other hand, turnover number of **[Ru(bpyMV2)$_3$]$^{14+}$** in H_2 evolution (TON_{PCS} = 231, 5h) is higher than that of **[Ru(4,4'-aspMV4)$_3$]$^{26+}$** (TON_{PCS} = 161, 5h),[13a] showing a higher stability. Moreover, as shown in Figure 19, the amounts of reduced species populated (i.e., $MV^{+\bullet}$ and $(MV^+)_2$) during the photocatalysis are much less than those populated in the absence of Pt (see Figure 12), indicating that the catalytic rate exceeds the electron storage rate. As noted above, H_2 evolution driven by the non-dimerized $MV^{+\bullet}$ is much more favorable compared to that by the dimerized $(MV^+)_2$ (*vide supra*). Therefore, it is quite reasonable to consider that the rapid consumption of the reduced equivalents by fast H_2 evolution reaction prevents the degradation of the photosystem such as polymerization of viologen species, as described elsewhere.[22] Actually, the previous **PCS**s predominantly form π -dimer $(MV^+)_2$ sites and exhibit lower radical consumption rates and faster degradation,[13a] while the present **PCS** predominantly forms monoradical $MV^{+\bullet}$ site, which vanishes faster due to the fast catalysis and degrades slower.

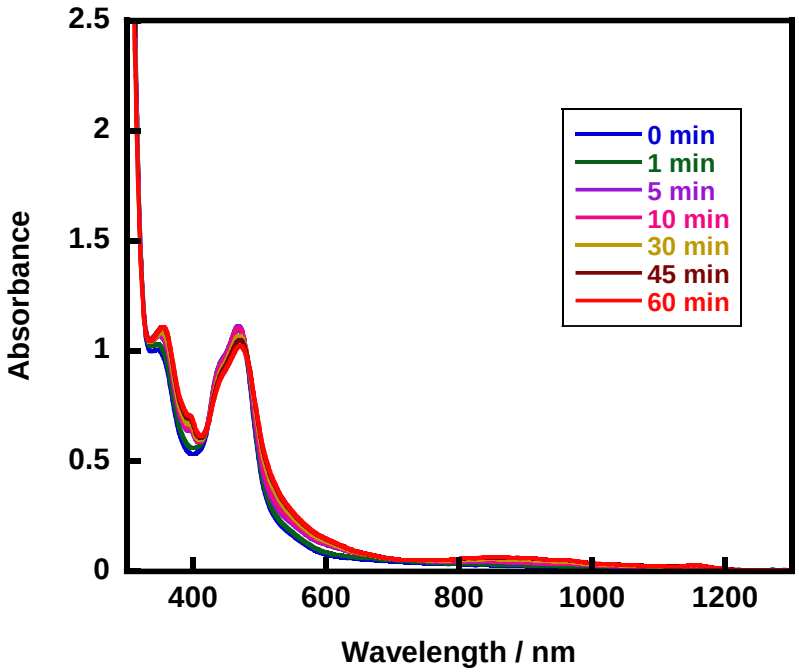

Figure 19. Spectral changes of **[Ru(bpyMV2)$_3$]$^{14+}$** during the photocatalytic reaction depicted in Figure 17.

.

The higher robustness realized for the present **PCS** (TON_{PCS} = 231, 5h) can also be compared with much lower robustness observed for the non-covalently bonded systems, that is, the two-component system consisting of $[Ru(bpy)_3]^{2+}$ and 6 equivalents of MV^{2+}, shown in Figure 17. It shows that the H_2 evolution ceases much earlier after around 30 min irradiation with much lower turnover number (TON_{PCS} = 73, 5h) than that of **[Ru(bpyMV2)$_3$]$^{14+}$**. Obviously, this is attributable to the degradation of MV^{2+} mainly by hydrogenation of MV^{2+}, as previously described.[15,23] Actually, the photocatalytic H_2 evolution could be re-activated by simply adding the same equivalents of MV^{2+} to the photolysis solution after the cease of H_2 evolution (Figure 20). Moreover, such re-activation could not be achieved when the initially added amount of $[Ru(bpy)_3]^{2+}$ was added instead of adding MV^{2+}.

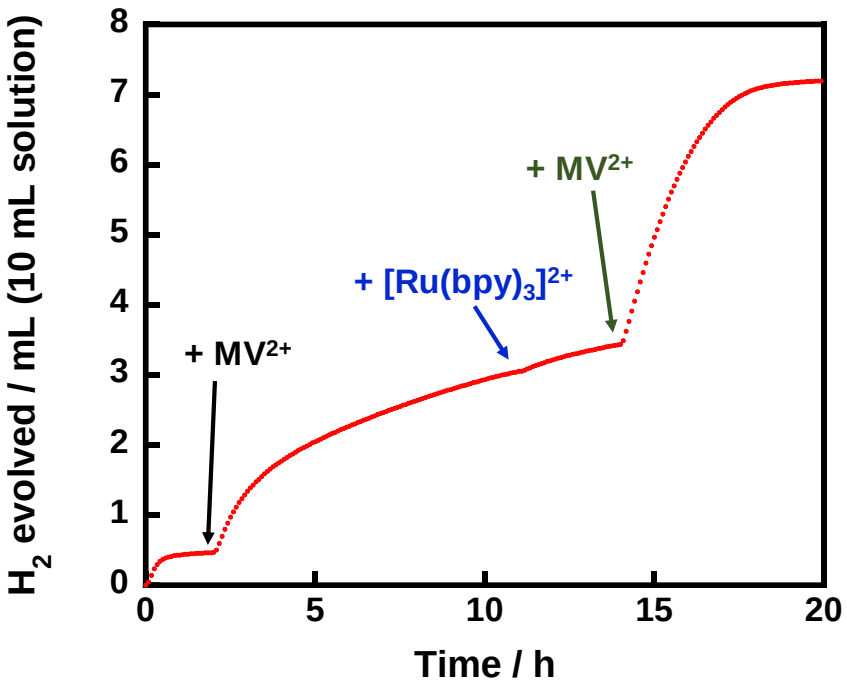

Figure 20. The recovery of photocatalytic activity for H_2 production from an aqueous acetate buffer solution (pH 5.0, 10 mL; at 20 °C under Ar) for the bulk system consisting of 0.1 mM PVP-protected colloidal Pt, 30 mM EDTA (Na_2YH_2), 0.04 mM $[Ru(bpy)_3](NO_3)_2$, and 0.24 mM $MV(NO_3)_2$ by the addition of 2.4 μmol $MV(NO_3)_2$ at 2 h (black arrow), 0.40 μmol $[Ru(bpy)_3](NO_3)_2$ at 11 h (blue arrow), and 2.4 μmol $MV(NO_3)_2$ at 14 h (green arrow).

Similarly, the hydrogenation of **[Ru(bpyMV2)$_3$]$^{14+}$** catalyzed by colloidal Pt is likely to be the major cause of its deactivation, as evidenced by the following experiments (Figures 21 and 22). While the H_2 evolution activity increases by increasing the **[Ru(bpyMV2)$_3$]$^{14+}$** concentration (Figure 21), an opposite trend is observed when the amount of colloidal Pt is increased, likely due to the enhancement of the hydrogenation of the MV^{2+} moieties (Figure 22). Certainly, similar behaviors were also observed for the two-component $[Ru(bpy)_3]^{2+}/MV^{2+}$ systems.[23b,24] While such a two-component system is deactivated around 2 h of irradiation, the **[Ru(bpyMV2)$_3$]$^{14+}$** system maintains its activity even after the 24 h of photoirradiation (Figure 18). It is assumed that this is due to the significant steric hindrance of **[Ru(bpyMV2)$_3$]$^{14+}$** compared to the free MV^{2+}. A reasonable consideration is that the free MV^{2+} can make an easier access to the Pt surfaces that are protected by the PVP frameworks, leading to the more efficient hydrogenation reactions to proceed. On the other hand, relatively large steric hindrances are provided around the viologen units installed in **[Ru(bpyMV2)$_3$]$^{14+}$**, which probably makes them less favorable to have an access to the Pt surfaces in order to get them hydrogenated. It is also reasonable to consider that the electron transfer leading to H_2 evolution may be allowed without having a close contact, although hydrogenation reaction must proceed via collision between a MV^{2+} moiety and a possible Pt-H site.

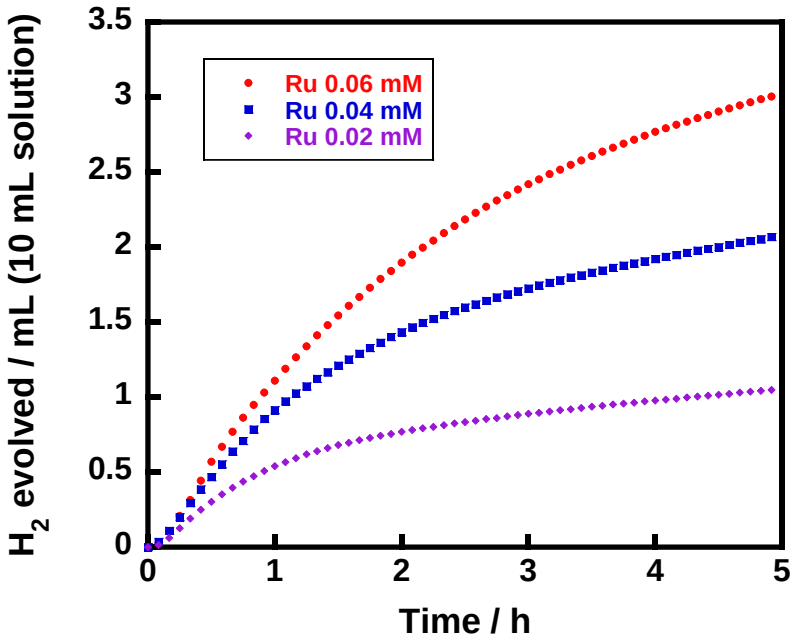

Figure 21. Photochemical H_2 production from an aqueous acetate buffer solution (pH 5.0, 10 mL; at 20 °C under Ar) containing PVP-protected colloidal Pt (0.1 mM on the basis of the net Pt atom concentration) and EDTA (30 mM) in the presence of (red) 0.06 mM, (blue) 0.04 mM, or (purple) 0.02 mM **[Ru(bpyMV2)$_3$]**$(PF_6)_{14}$.

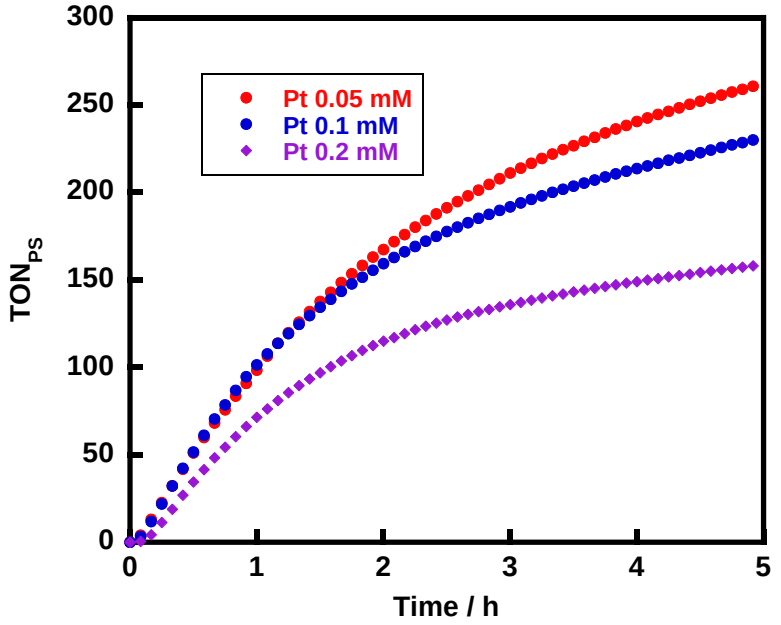

Figure 22. Photochemical H_2 production from an aqueous acetate buffer solution (pH 5.0, 10 mL; at 20 °C under Ar) containing (red) 0.05 mM (on the basis of the net Pt atom concentration), (blue) 0.1 mM, or (purple) 0.2 mM PVP-protected colloidal Pt and 30 mM EDTA in the presence of 0.04 mM **[Ru(bpyMV2)$_3$]**$(PF_6)_{14}$.

Conclusions

In this study, I investigated the photochemical and photocatalytic properties of my new **PCS**, **[Ru(bpyMV2)$_3$]$^{14+}$** in the photo-driven electron storage and H_2 evolution from water. Photochemical measurements revealed that the charge-separated states of photoexcited **[Ru(bpyMV2)$_3$]$^{14+}$** have the shorter lifetimes compared to the previous **PCS**s, leading to lower efficiency of the new **PCS** in photo-driven electron storage than those of the previously reported aspartic-acid-based **PCS**s. However, the present **PCS** has the advantage of the higher preference to store $MV^{+\bullet}$ versus $(MV^+)_2$ compared to the previous **PCS**s. This behavior is well understood on the basis of its shorter distance connecting the $Ru(bpy)_3^{2+}$ chromophore and the MV^{2+} acceptor units. The higher preference in forming the $MV^{+\bullet}$ site, which has higher reducing power than $(MV^+)_2$, also leads to improve the overall rate of photochemical H_2 production in the presence of colloidal Pt as a catalyst and EDTA as a sacrificial electron donor (Figure 23) in spite of its lower electron storage efficiency. Moreover, **[Ru(bpyMV2)$_3$]$^{14+}$** shows higher TON_{PCS} compared to the previous **PCS**s by suppressing decomposition of viologen residues due to its higher rate in catalytic process. The superior robustness of the present **PCS** is also rationalized by its higher resistant towards hydrogenation over the colloidal platinum owing to the steric hindrances around the viologen residues. This study shows storage of electrons with the $MV^{+\bullet}$ form is important to develop higher photocatalytic systems based on **PCS**s. These new aspects are quite important and useful in extended studies in molecular-based artificial photosynthesis systems.

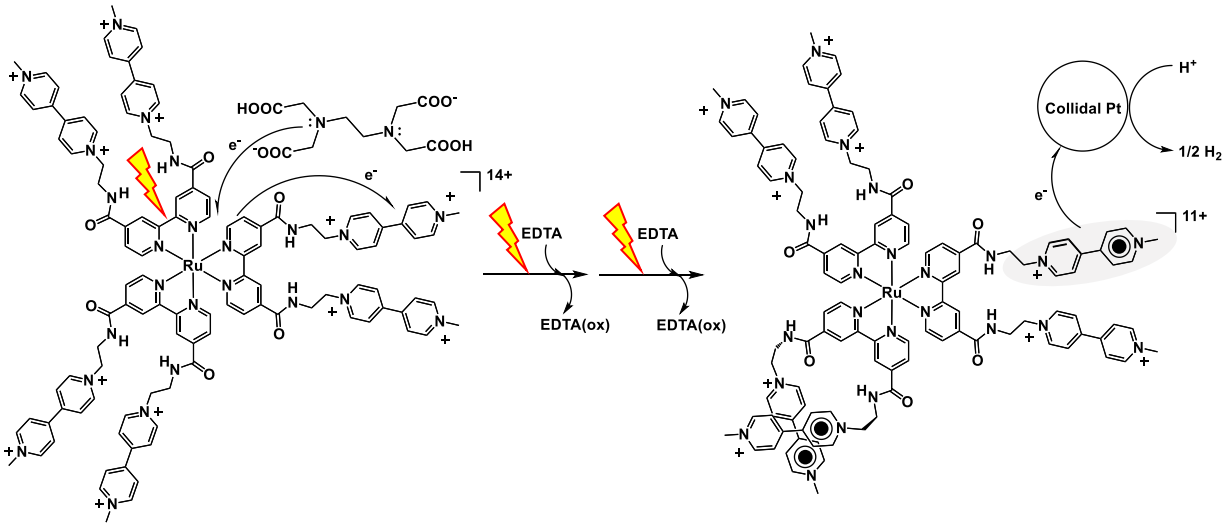

Figure 23. Schematic representation of photochemical H_2 production promoted by **[Ru(bpyMV2)$_3$]$^{14+}$**.

References

1. N. S. Lewis, D. G. Nocera, *Proc. Natl. Acad. Sci. U. S. A.* **2006**, *103*, 15729-15735.
2. (a) D. G. Nocera, *Acc. Chem. Res.* **2012**, *45*, 767−776.
   (b) V. S. Thoi, Y. Sun, J. R. Long, C. J. Chang, *Chem. Soc. Rev.* **2013**, *42*, 2388−2400.
   (c) J. R. McKone, N. S. Lewis, H. B. Gray, *Chem. Mater.* **2014**, *26*, 407−414.
3. (a) P. Du, R. Eisenberg, *Energy Environ. Sci.* **2012**, *5*, 6012-6021.
   (b) D. Z. Zee, T. Chantarojsiri, J. R. Long, C. J. Chang, *Acc. Chem. Res.* **2015**, *48*, 2027-2036.
   (c) P. D. Frischmann, K. Mahata, F. Würthner, *Chem. Soc. Rev.* **2013**, *42*, 1847-1870.
   (d) T. Stoll, M. Gennari, J. Fortage, C. E. Castillo, M. Rebarz, M. Sliwa, O. Poizat, F. Odobel, A. Deronzier, M.-N. Collomb, *Angew. Chem. Int. Ed.* **2014**, *53*, 1654-1658; *Angew. Chem.* **2014**, *126*, 1680-1684.
   (e) M. G. Pfeffer, T. Kowacs, M. Wächtler, J. Guthmuller, B. Dietzek, J. G. Vos, S. Rau, *Angew. Chem. Int. Ed.* **2015**, *54*, 6627-6631; *Angew. Chem.* **2015**, *127*, 6727-6731.
   (f) T. Kowacs, L. O'Reilly, Q. Pan, A. Huijser, P. Lang, S. Rau, W. R. Browne, M. T. Pryce, J. G. Vos, *Inorg. Chem.* **2016**, *55*, 2685-2690.
   (g) G. F. Manbeck, E. Fujita, K. J. Brewer, *J. Am. Chem. Soc.* **2017**, *139*, 7843-7854.
   (h) C. Lentz, O. Schott, T. Auvray, G. Hanan, B. Elias, *Inorg. Chem.* **2017**, *56*, 10875−10881.
   (i) C.-F. Leung, S.-C. Cheng, Y. Yang, J. Xiang, S.-M. Yiu, C.-C. Ko, T.-C. Lau, *Catal. Sci. Technol.* **2018**, *8*, 307–313.
4. (a) J. J. Concepcion, M.-K. Tsai, J. T. Muckerman, T. J. Meyer, *J. Am. Chem. Soc.* **2010**, *132*, 1545-1557.
   (b) L. Duan, F. Bozoglian, S. Mandal, B. Stewart, T. Privalov, A. Llobet, L. Sun, *Nat. Chem.* **2012**, *4*, 418-423.
   (c) L. Kohler, N. Kaveevivitchai, R. Zong, R. P. Thummel, *Inorg. Chem.* **2014**, *53*, 912-921.
   (d) C. Casadevall, Z. Codolà, M. Costas, J. Lloret-Fillol, *Chem. Eur. J.* **2016**, *22*, 10111-10126.
   (e) M. Schulze, V. Kunz, P. D. Frischmann, F. Würthner, *Nat. Chem.* **2016**, *8*, 576–583.
   (f) M. Okamura, M. Kondo, R. Kuga, Y. Kurashige, T. Yanai, S. Hayami, V. K. K. Praneeth, M. Yoshida, K. Yoneda, S. Kawata, S. Masaoka, *Nature* **2016**, *530*, 465-468.
   (g) K. J. Fisher, K. L. Materna, B. Q. Mercado, R. H. Crabtree, G. W. Brudvig, *ACS Catal.* **2017**, *7*, 3384−3387.
   (h) A. Bucci, S. Dunn, G. Bellachioma, G. M. Rodriguez, C. Zuccaccia, C. Nervi, A. Macchioni, *ACS Catal.* **2017**, *7*, 7788−7796.

(i) P. Garrido-Barros, C. Gimbert-Suriñach, D. Moonshiram, A. Picoón, P. Monge, V. S. Batista, A. Llobet, *J. Am. Chem. Soc.* **2017**, *139*, 12907−12910.

5. G. Ananyev, G. C. Dismukes, *Photosynth. Res.* **2005**, *84*, 355-365.
6. E. Ceccarelli, A. K. Arakaki, N. Cortez, N. Carrillo, *Biochim. Biophys. Acta* **2004**, *1698*, 155-165.
7. H. Kirchhoff, S. Horstmann, E. Weis, *Biochim. Biophys. Acta* **2000**, *1459*, 148-168.
8. (a) M. P. O'Neil, M. P. Niemczyk, W. A. Svec, D. Gosztola, G. L. Gaines III, M. R. Wasielewski, *Science* **1992**, *257*, 63-65.

   (b) T. H. Ghaddar, J. F. Wishart, D. W. Thompson, J. K. Whitesell, M. A. Fox, *J. Am. Chem. Soc.* **2002**, *124*, 8285-8289.

   (c) S. Karlsson, J. Boixel, Y. Pellegrin, E. Blart, H.-C. Becker, F. Odobel, L. Hammarström, *J. Am. Chem. Soc.* **2010**, *132*, 17977-17979.

   (d) M. Orazietti, M. Kuss-Petermann, P. Hamm, O. S. Wenger, *Angew. Chem. Int. Ed.* **2016**, *55*, 9407-9410; *Angew. Chem.* **2016**, *128*, 9553-9556.

   (e) M. Kuss-Petermann, M. Orazietti, M. Neuburger, P. Hamm, O. S. Wenger, *J. Am. Chem. Soc.* **2017**, *139*, 5225-5232; (f) M. Kuss-Petermann, O. S. Wenger, *Chem. Eur. J.* **2017**, *23*, 10808-10814.
9. (a) S. M. Molnar, G. Nallas, J. S. Bridgewater, K. J. Brewer, *J. Am. Chem. Soc.* **1994**, *116*, 5206-5210.

   (b) M. Elvington, K. J. Brewer, *Inorg. Chem.* **2006**, *45*, 5242-5244.

   (c) K. Rangan, S. M. Arachchige, J. R. Brown, K. J. Brewer, *Energy Environ. Sci.* **2009**, *2*, 410-419.

   (d) R. Konduri, H. Ye, F. M. MacDonnell, S. Serroni, S. Campagna, K. Rajeshwar, *Angew. Chem. Int. Ed.* **2002**, *41*, 3185-3187; *Angew. Chem.* **2002**, *114*, 3317-3319.

   (e) D. E. Polyansky, D. Cabelli, J. T. Muckerman, T. Fukushima, K. Tanaka, E. Fujita, *Inorg. Chem.* **2008**, *47*, 3958-3968.

   (f) T. Asatani, Y. Nakagawa, Y. Funada, S. Sawa, H. Takeda, T. Morimoto, K. Koike, O. Ishitani, *Inorg. Chem.* **2014**, *53*, 7170-7180.

   (g) J. M. Aslan, D. J. Boston, F. M. MacDonnell, *Chem. Eur. J.* **2015**, *21*, 17314-17323.

   (h) J. Nomrowski, O. S. Wenger, *J. Am. Chem. Soc*. **2018**, *140*, 5343-5346.

   (i) J.-F. Lefebvre, J. Schindler, P. Traber, Y. Zhang, S. Kupfer, S. Gräfe, I. Baussanne, M. Demeunynck, J.-M. Mouesca, S. Gambarelli, V. Artero, B. Dietzek, M. Chavarot-Kerlidou, *Chem. Sci.* **2018**, *9*, 4152-4159.
10. H. Li, A. C. Fahrenbach, A. Coskun, Z. Zhu, G. Barin, Y. L. Zhao, Y. Y. Botros, J.-P. Sauvage, J. F. Stoddart, *Angew. Chem. Int. Ed.* **2011**, *50*, 6782-6788; *Angew. Chem.* **2011**, *123*, 6914-6920.

11. (a) K. J. Elliott, A. Harriman, L. L. Pleux, Y. Pellegrin, E. Blart, C. R. Mayer, F. Odobel, *Phys. Chem. Chem. Phys.* **2009**, *11*, 8767-8773.
(b) B. Matt, J. Fize, J. Moussa, H. Amouri, A. Pereira, V. Artero, G. Izzet, A. Proust, *Energy Environ. Sci.* **2013**, *6*, 1504-1508.
12. (a) K. Kitamoto, K. Sakai, *Angew. Chem. Int. Ed.* **2014**, *53*, 4618-4622; *Angew. Chem.* **2014**, *126*, 4706-4710.
(b) K. Yamamoto, K. Kitamoto, K. Yamauchi, K. Sakai, *Chem. Commun.* **2015**, *51*, 14516-14519.
(c) K. Kitamoto, K. Sakai, *Chem. Commun.* **2016**, *52*, 1385-1388.
(d) S. Lin, K. Kitamoto, H. Ozawa, K. Sakai, *Dalton Trans*. **2016**, *45*, 10643-10654.
13. (a) K. Kitamoto, M. Ogawa, G. Ajayakumar, S. Masaoka, H.-B. Kraatz, K. Sakai, *Inorg. Chem. Front.* **2016**, *3*, 671-680.
(b) K. Kitamoto, K. Sakai, *Chem. Eur. J.* **2016**, *22*, 12381-12390.
14. E. Dulière, M. Devillers, J. Marchand-Brynaert, *Organometallics* **2003**, *22*, 804-811.
15. K. Sakai, Y. Kizaki, T. Tsubomura, K. Matsumoto, *J. Mol. Catal.* **1993**, *79*, 141-152..
16. M. Kobayashi, S. Masaoka, K. Sakai, *Dalton Trans.* **2012**, *41*, 4903-4911.
17. R. Okazaki, S. Masaoka, K. Sakai, *Dalton Trans.* **2009**, 6127-6133.
18. M. Ogawa, B. Balan, G. Ajayakumar, S. Masaoka, H.-B. Kraatz, M. Muramatsu, S. Ito, Y. Nagasawa, H. Miyasaka, K. Sakai, *Dalton Trans.* **2010**, *39*, 4421-4434.
19. D. R. James, Y.-S. Liu, P. De Mayo, W. R. Ware, *Chem. Phys. Lett.* **1985**, *120*, 460-465.
20. M. Ogawa, G. Ajayakumar, S. Masaoka, H.-B. Kraatz, K. Sakai, *Chem. Eur. J.* **2011**, *17*, 1148-1162.
21. W. S. Jeon, H.-J. Kim, C. Lee, K. Kim, *Chem. Commun.* **2002**, 1828-1829.
22. (a) M. Gohn, N. Getoff, *Z. Naturf. Teil A* **1979**, *34*, 1135-1139.
(b) S. Tanaka, S. Masaoka, K. Yamauchi, M. Annaka, K. Sakai, *Dalton Trans.* **2010**, *39*, 11218-11226.
23. (a) P. Keller, A. Moradpour, E. Amouyal, H. B. Kagan, *Nouv. J. Chim.* **1980**, *4*, 377-384.
(b) O. Johansen, A. Launikonis, J. W. Loder, A. W.-H. Mau, W. H. F. Sasse, J. D. Swift, D. Wells, *Aust. J. Chem.* **1981**, *34*, 981-991.
24. E. Amouyal, P. Koffi, *J. Photochem.* **1985**, *29*, 227-242.

Chapter 3

CO_2 Reduction Catalyzed by a Ru Complex Having Imidazolium Moieties

Introduction

Catalytic conversion of CO_2 into valuable chemical fuels has attracted much attention because this reaction contributes not only to reduce the greenhouse gas but also to decrease the consumption of fossil fuels.[1] In this context, many efforts have been made to develop efficient homogeneous[2] and heterogeneous[3] electrocatalysts for CO_2 reduction, however, achievement of catalytic conversion of CO_2 with high selectivity and low overpotential is still challenging.

One of possible approaches to achieve high efficient reaction systems is to use metal complex catalysts having functional moieties which interact with CO_2 molecules activated on metal ions. Upon now, some molecular catalysts having functional moieties such as hydroxy group,[4a,b] amine group,[4c,d] and trimethylammonium group[4e] have been reported and shown higher activities than those of non-functionalized catalysts. In this context, metal complexes having imidazolium (**Im**) moieties (e.g., **[Re_Im]**$^{+}$ and **[Fe_Im]**$^{4+}$ in Figure 1a) recently have been paid attention because **Im**-functionalization also results in enhancement of catalytic efficiency.[5,6] These studies have shown the effectiveness of introducing functional moieties, however, detail properties of these moieties have not been revealed. In this context, Warren et al. recently reported importance of solvent properties for catalytic activity of a hydroxy-functionalized Fe porphyrin catalyst (**Fe_OH** in Figure 1b).[7] In their study, it was revealed that **Fe_OH** shows much higher activity for electrocatalytic CO_2 reduction in MeCN compared to that in DMF. They assume that this is due to the higher Lewis basicity of DMF than that of MeCN. Focusing on the CO_2-bound intermediate of **Fe_OH** during catalysis, it can be considered that there is equilibrium between intra (A in Figure 1b) and intermolecular (B in Figure 1b) hydrogen-bonding states, where the A state is favorable for promoting CO_2 reduction because of stabilization of the CO_2-bound state. Warren et al. assume that the population of the B state should be higher for DMF due to a higher ability as a Lewis base compared to MeCN, resulting in the much lower activity in DMF than that in MeCN. From these reported results, it is expected that the solvent also affect catalytic activity of

Im-functionalized metal complexes, however, solvent effects have not been investigated for these catalysts yet.[5,6]

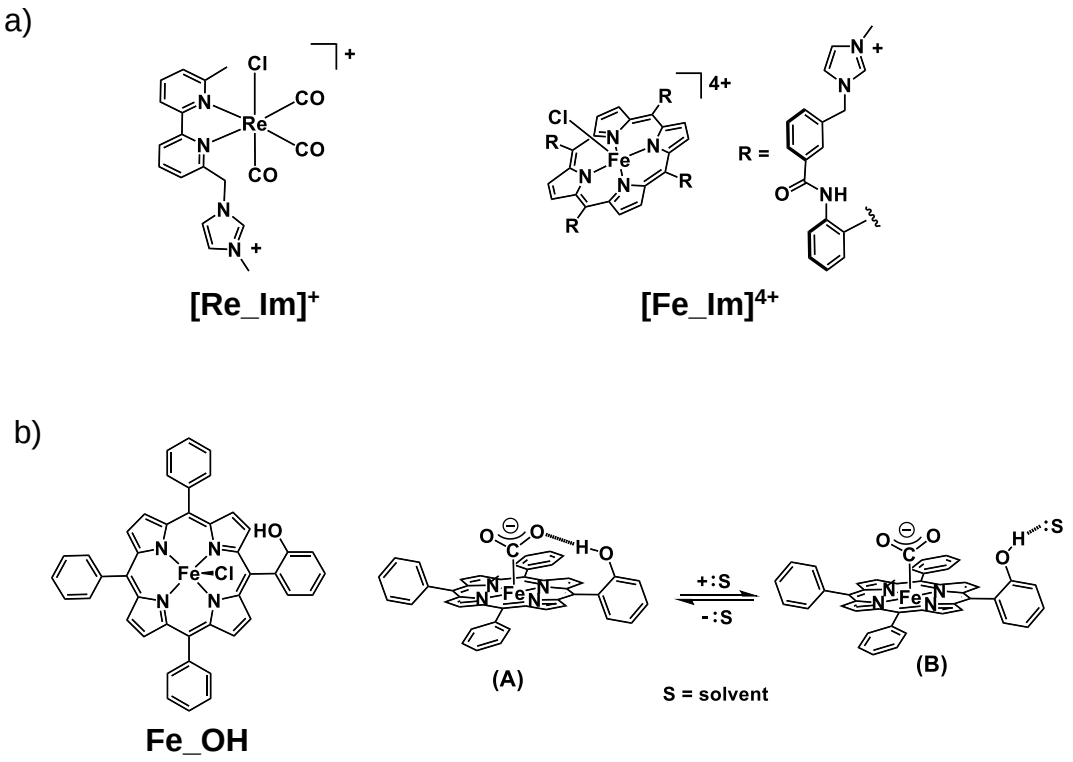

Figure 1. a) Molecular structures of [**Re_Im**]$^{+}$ and [**Fe_Im**]$^{4+}$. b) Molecular structure of **Fe_OH** and possible structures of the CO_2-bound **Fe_OH** forming intra (A) or intermolecular (B) hydrogen bond.

Here, using a bpy ligand having **Im** moieties (**[bpy_Im]**$^{2+}$ in Figure 2a), a new Ru-based electrocatalyst for CO_2 reduction is developed based on the $[Ru(bpy)(tpy)Cl]^+$ (bpy = 2,2'-bipyridine, tpy = 2,2':6',2"-terpyridine) structure, which is known to be active for CO_2 reduction (**[Ru_Im]**$^{3+}$ in Figure 2a).[8] Figure 2b shows a possible structure of the Ru-CO_2 adduct computed by the molecular mechanics method, where the distances between protons of an **Im** moiety, H_A and H_B, and O atom of CO_2 (O_A) are 2.43 Å and 2.77 Å, respectively. According to this result, it is expected that an **Im** moiety can interact with a CO_2 molecule during the catalytic reaction. In this study, experimental and theoretical investigations with comparison to the control complex having a dmbpy (5,5'-dimethyl-2,2'-bipyridine) ligand (**[Ru_Me]**$^+$ in Figure 2a) unveiled the unique effects by the addition of **Im** moieties; the significant stabilization of π* orbital of the bpy ligand and the interesting dependence of catalytic activity on solvents.

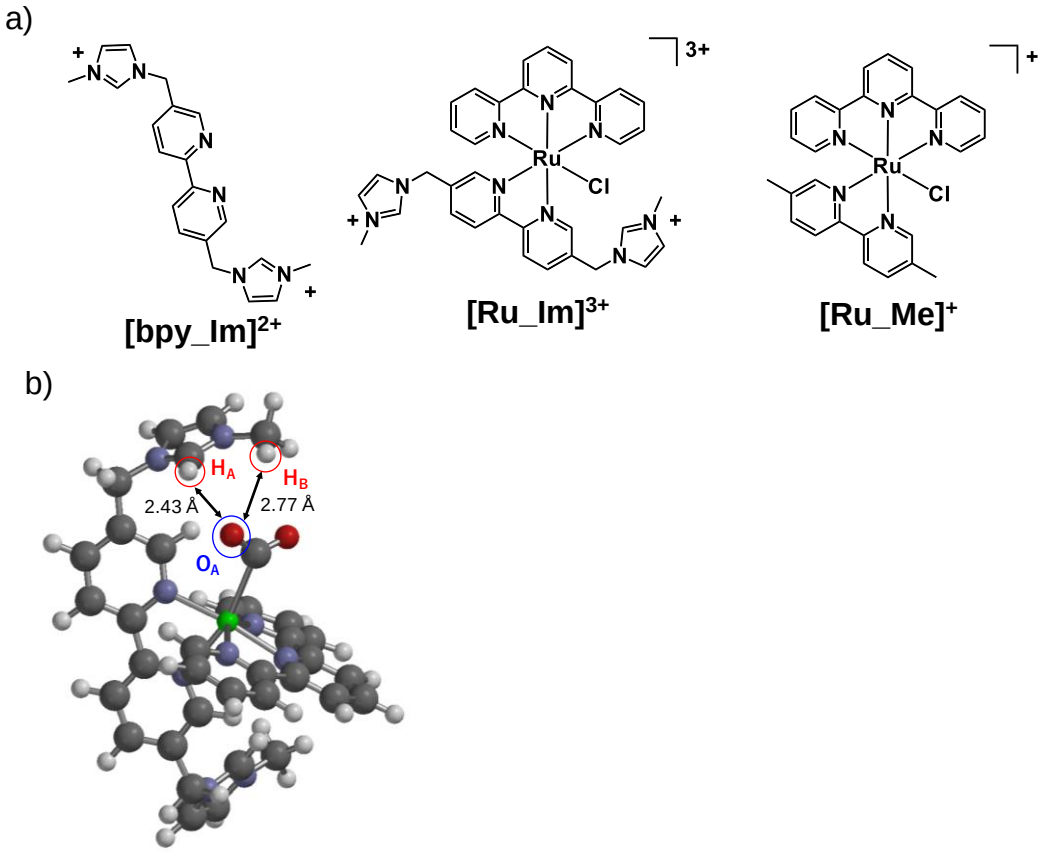

Figure 2. a) Molecular structures of compounds studied in this work. b) A structure of the CO_2-bound **[Ru_Im]**$^{3+}$ computed by MMFF94.

Experimental Section

Materials

5,5'-Dimethyl-2,2'-bipyridine was purchased from Tokyo Chemical Industry Co., Ltd. All other chemicals and solvents were purchased from Kanto Chemicals Co., Inc. and used without further purification. **[Bpy_Im]**$(PF_6)_2$[9] and $Ru(tpy)Cl_3$[10] were synthesised as previously described.

Synthesis of $[Ru\_Im](PF_6)_3$

This was prepared by refluxing a solution of $Ru(tpy)Cl_3$ (0.42 g, 0.96 mmol), **[bpy_Im]**$(PF_6)_2$ (0.62 mg, 0.97 mmol), LiCl (0.22 g, 5.2 mmol), and ascorbic acid (0.34 g, 1.9 mmol) in a water-ethanol mixture (3 : 1 v/v, 60 mL) for 4 h. After cooling to room temperature, the solution was concentrated by evaporation in order to remove most of ethanol, resulting in deposition of the product as a deep purple solid. This crude product was redissolved in a water-acetone mixture (5 : 3 v/v, 8 mL). This solution was left at room temperature overnight for the gradual evaporation of acetone. The final product, deposited as a deep purple powder, was collected by filtration and dried in vacuo (yield: 0.38 g, 35 %). ^{1}H NMR (DMSO-d6/TMS, ppm): δ 10.1 (d, J = 1.2 Hz, 1H), 9.39 (s, 1H), 8.95 (d, J = 8.2 Hz, 1H), 8.88 (s, 1H), 8.82 (d, J = 8.2 Hz, 2H), 8.70-8.66 (m, 3H), 8.31-8.28 (m, 2H), 8.03-7.98 (m, 3H), 7.85 (t, J = 1.5 Hz, 1H), 7.67-7.63 (m, 4H), 7.37-7.35 (m, 3H), 7.09 (d, J = 1.2 Hz, 2H), 5.84 (s, 2H), 5.21 (s, 2H), 3.92 (s, 3H), 3.83 (s, 3H); Anal. Calcd for $C_{35}H_{33}ClF_{18}N_9P_3Ru$ (1151.12): C, 36.52; H, 2.89; N, 10.95. Found: C, 36.96; H, 2.84; N, 10.70.

Synthesis of [Ru_Me](PF_6)

This was prepared by refluxing a solution of $Ru(tpy)Cl_3$ (0.60 g, 1.4 mmol), 5,5'-dimethyl-2,2'-bipyridine (0.64 mg, 3.5 mmol), LiCl (0.94 g, 22 mmol), and triethylamine (2.4 mL, 1.7 g, 17 mmol) in a water-ethanol mixture (3 : 1 v/v, 240 mL) for 4 h. After cooling to room temperature, the reaction mixture was filtered to remove insoluble materials. Then, the solution was concentrated by evaporation in order to remove most of ethanol, resulting in deposition of the product as a deep purple solid. This crude product was redissolved in ethanol (10 mL). Then, this solution was added to toluene (200 mL) in order to re-precipitate the product. The resulting crude product was collected by filtration (0.62 g). This product (0.20 g) was redissolved in water (20 mL) and filtered off, followed by the addition of saturated aqueous NH_4PF_6 (ca. 0.4 mL), resulting in prompt deposition of the product as a deep purple solid. This crude product was redissolved in a water-acetone mixture (1 : 5 v/v, 12 mL). This solution was left at room temperature overnight for the gradual evaporation of acetone. The final product, deposited as a deep purple powder, was collected by filtration and dried in vacuo (yield: 0.13 g, 40 %). ^{1}H NMR (DMSO-d6/TMS, ppm): δ 9.88 (s, 1H), 8.79 (d, J = 8.2 Hz, 2H), 8.75 (d, J = 8.2 Hz, 1H), 8.68 (d, J = 8.2 Hz, 2H), 8.47 (d, J = 8.3 Hz, 1H), 8.21 (t, J = 8.2 Hz, 1H), 8.17 (dd, J = 8.4, 1.2 Hz, 1H), 7.98 (td, J = 8.4, 1.2 Hz, 2H), 7.62 (d, J = 5.5 Hz, 2H), 7.59 (d, J = 7.6 Hz, 1H), 7.38 (m, 2H), 7.05 (d, J = 1.2 Hz, 1H), 2.65 (s, 3H), 1.98 (s, 3H); Anal. Calcd for $C_{35}H_{33}ClF_{18}N_9P_3Ru$ (699.00): C, 46.39; H, 3.32; N, 10.02. Found: C, 46.17; H, 3.23; N, 9.99.

General Methods

UV-Vis spectra were recorded on a Shimadzu UV-2600 spectrophotometer. ^{1}H NMR spectra were acquired on a JEOL JNM-ESA 600 spectrometer. Cyclic voltammograms (CVs) were recorded on a BAS ALS Model 700E electrochemical analyzer, using a three electrode system consisting of a platinum working electrode, a platinum wire counter electrode, and a Ag/Ag^+ reference electrode (0.249 V vs. SCE), where TBAH (tetra(*n*-butyl)ammonium hexafluorophosphate) was used as a supporting

electrolyte and all reported potentials are given relative to the Fc/Fc^+ couple (Fc/Fc^+ = 0.380 vs SCE). The bulk electrolysis was carried out by using a carbon rod working electrode, a platinum mesh counter electrode, and Ag/Ag^+ reference electrode. The working compartment was separated from the counter compartment using a glass filter. The amount of CO evolved during the bulk electrolysis was monitored by a gas chromatograph. A structure of the CO_2-bound **[Ru_Im]$^{3+}$** were optimized by MMFF94 using Spartan Student Edition ver. 3.0.2.

DFT Calculation Methods

Density functional theory (DFT) calculations were performed using Gaussian 9 packages[11] to understand the structural and spin-state candidates. The structures were fully optimized using the B3LYP density functional[12,13] with the effect of solvation in n,n-dimethylformaldehyde (DMF) taken into consideration using the polarizable continuum model (PCM) method.[14-16] The LanL2DZ basis[17-19] set was applied to all atoms. The redox potentials are calculated as described in Scheme 1. As the benchmark of each reduction step, the first oxidation potential of **[Ru_Me]$^+$** are used. A experimental data (i.e., CV) of **[Ru_Me]$^+$**, where the voltammogram shows a reversible oxaidation at 0.33 V vs. Fc/Fc^+ (ΔE_p = 69 mV), is shown in Figure 4.

Scheme 1. Isodesminc reaction methods[20-28] for calculating redox potentials based on the experimentally determined value for the oxidation potential of **[Ru_Me]$^+$** (0.33 V vs. Fc/Fc^+). *F* is Faraday constant, *R* is the gas constant, and *T* is temperature (298.15 K).

$Ox + e^- \rightarrow Red \qquad \Delta G^0 = -FE^0$

[Ru_Me]$^+$ $\rightarrow$ **[Ru_Me]$^{2+}$** $+ e^-$

$\Delta G^0_{ref} = -FE^0_{ref} \qquad E^0_{ref}$ = 0.33 V vs. Fc/Fc^+

$Ox +$ **[Ru_Me]$^+$** $\rightarrow$ $Red +$ **[Ru_Me]$^{2+}$**

$\Delta G^0_r = G(\text{Red})_{solv} + G(\textbf{[Ru\_Me]}^{2+})_{solv} - G(\text{Ox})_{solv} - G(\textbf{[Ru\_Me]}^{+})_{solv}$
$\Delta G^0_r = -\Delta G^0_{ref} + \Delta G^0 = FE^0_{ref} - FE^0$
$E^0 = -\Delta G^0_r / F + E^0_{ref}$

Results and Discussion

Photochemical Properties

[Ru_Me]$^{+}$ shows a characteristic absorption at 500 nm assignable to the metal-to-ligand charge transfer (MLCT) band (Figure 3, blue). As described below, the lowest unoccupied molecular orbital (LUMO) of **[Ru_Me]$^{+}$** mainly locates over the tpy ligand, therefore, the MLCT band is mainly derived from the charge transfer from d(Ru) to π*(tpy). For comparison, **[Ru_Im]$^{3+}$** exhibits the obviously red shifted MLCT band (514 nm, Figure 3, red). Since the LUMO of **[Ru_Im]$^{3+}$** populates dominantly over the bpy ligand having two covalently linked cationic imidazolium moieties (described below), the MLCT band is considered to be mainly derived from the transition from d(Ru) to π*(bpy). Thus, the obvious red shift in the MLCT band indicates that the π* orbital of bpy is largely stabilized to the lower level than that of the tpy ligand by introducing two cationic imidazolium moieties. As mentioned below, these results agree well with those for electochemical measurements. Additionally, according to the absorption characters of [**bpy_Im]$^{2+}$** and tpy ligands (Figure 3 green and brown), the spectral features at 301 nm and 238 nm are attributable to π-π* transitions of the bpy and tpy ligands. The absorption of imidozolium moieties should be included in the band around 200 nm because the free 1-ethyl-3-methylimidazolium (EMIM) shows the characteristic band at 211 nm (Figure 3 purple).

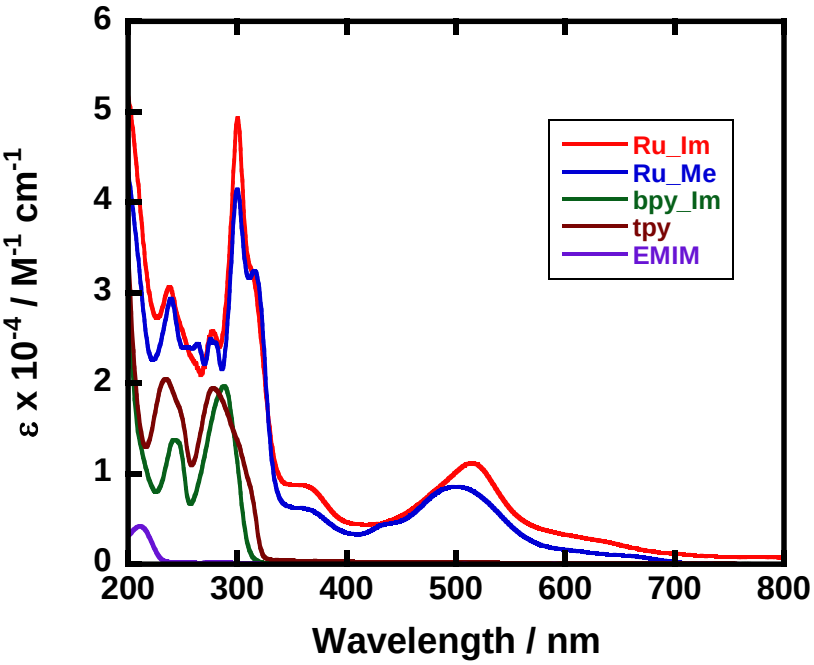

Figure 3. Absorption spectra of (red) **[Ru_Im]**$^{3+}$, (blue) **[Ru_Me]**$^{+}$, (green) **[bpy_Im]**$^{2+}$, (brown) tpy, and (purple) 1-ethyl-3-methylimidazolium (EMIM) in MeCN.

Electrochemical Properties

Cyclic voltammograms of **[Ru_Im]$^{3+}$** and **[Ru_Me]$^{+}$** measured in DMF under Ar atmosphere are shown in Figure 4. One reversible redox wave and two irreversible reduction waves are observed at 0.33, -1.89, and -2.16 V vs. Fc/Fc^{+} for **[Ru_Me]$^{+}$** (see Table 1). Based on the reported assignment for the structural analogue complex ([Ru(tpy)(bpy)Cl]$^{+}$),[8b] the reversible redox wave is assigned as the Ru^{II}/Ru^{III} redox couple, and the irreversible reduction waves correspond to the one electron reduction at the tpy and the dmbpy ligands, respectively. The irreversible character observed for two reduction waves suggests that these reductions proceed coupled with releasing the Cl^{-} ligand the same as previously reported analogue complex ([Ru(tpy)(bpy)Cl]$^{+}$).[8b]

On the other hand, one reversible redox wave and three irreversible reduction waves are observed at 0.38, -1.72, -1.93, and -2.16 V vs. Fc/Fc^{+} for **[Ru_Im]$^{3+}$** (see Table 1). The reversible redox wave is also assignable to the Ru^{II}/Ru^{III} redox couple. As shown by the results of DFT calculations (described below), the LUMO of **[Ru_Im]$^{3+}$** populates dominantly over the bpy ligand having two covalently linked cationic imidazolium moieties, therefore, the first reduction is assignable to the one electron reduction at the bpy ligand. Importantly, compared to **[Ru_Me]$^{+}$**, the first reduction potential for **[Ru_Im]$^{3+}$** largely shifts to the positive direction compared to the potential assignable to the dmbpy ligand of **[Ru_Me]$^{+}$** with the Ru^{II}/Ru^{III} redox wave almost unchanged. This result clearly indicates that the π^* orbital of bpy for **[Ru_Im]$^{3+}$** is stabilized by introducing two cationic imidazolium moieties as described above. This positive shift were also observed in the reported system, **[Re_Im]$^{3+}$**, where the introduction of one **Im** moiety via methylene linker leads to positive shift of first reduction potential compered to non-functionalized *fac*-$ReCl(bpy)(CO)_3$.[5] Currently, assignment of the other two reduction waves still remain unclear.

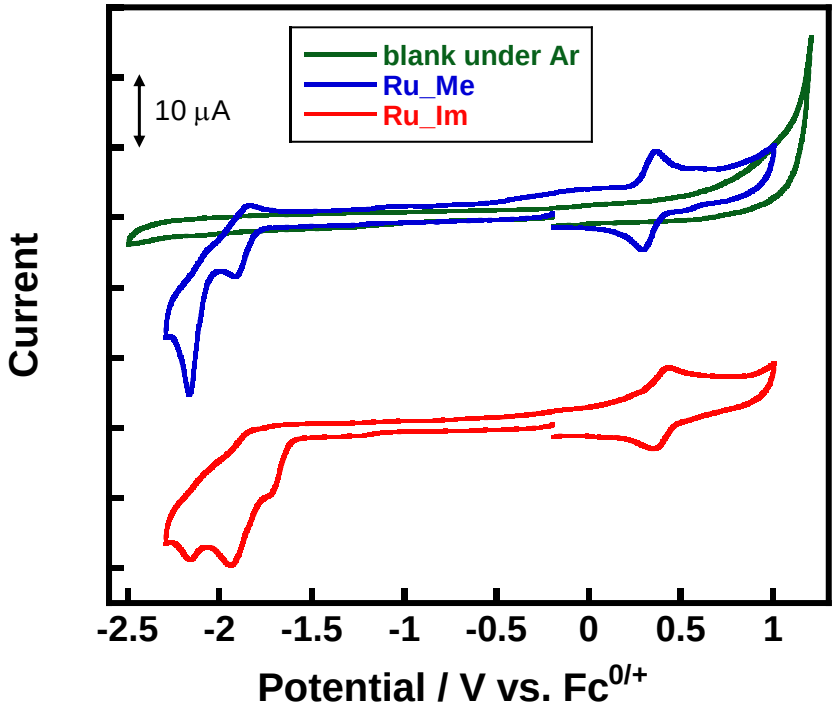

Figure 4. CVs for a DMF solution of (red) **[Ru_Im]**$^{3+}$ and (blue) **[Ru_Me]**$^{+}$. Measurements were carried out for a 0.5 mM solution of the complex in DMF containing 0.1 M tetra(*n*-butyl)ammonium hexafluorophosphate (TBAH) at room temperature under Ar atmosphere, recorded at a sweep rate of 100 mV s^{-1}.

Table 1. Redox potentials for **[Ru_Im]**$^{3+}$ and **[Ru_Me]**$^{+}$. The values in parenthesis are the potentials estimated from DFT results.

Complex		**[Ru_Im]**$^{3+}$	**[Ru_Me]**$^{+}$
Oxidation[a]	$E_{ox,1}$	0.38[b]	0.33[b]
Reduction[a]	$E_{red,1}$	-1.72[c] (-1.46[d])	-1.89[b] (-1.88[d])
	$E_{red,2}$	-1.93[c]	-2.16[c]
	$E_{red,3}$	-2.16[c]	

[a] Potentials are given in volts vs. Fc/Fc^{+} (The voltammograms are shown in Figure 4). [b] A half-wave potential. [c] Estimated for the response of cathodic currents. [d] Potentials estimated from DFT results.

DFT Calculations

In order to obtain important insights into the photo- and electrochemical properties, the ground state and the one-electron reduced species of **[Ru_Im]**$^{3+}$ and **[Ru_Me]**$^{+}$ were computed. In the case of **[Ru_Me]**$^{+}$, the LUMO of the ground state species mainly locates over the tpy ligand and the spin density of the one-electron reduced species largely exists over the tpy ligand (see Figures 5a,c). On the other hand, the LUMO of the ground state species of **[Ru_Im]**$^{3+}$ dominantly populates over the bpy ligand having two covalently linked cationic **Im** moieties, and the spin density of the one-electron reduced species largely exists over the bpy ligand (see Figures 5b,d). These results indicate that the positively charged **Im** moiety has a strong electron-withdrawing ability, and thus the introduction of them decrease the energy level of the π^* orbital of the bpy ligand lower than that of the tpy ligand. Based on these results, the second reduction wave for **[Ru_Im]**$^{3+}$ corresponds to the one electron reduction of the tpy ligand.

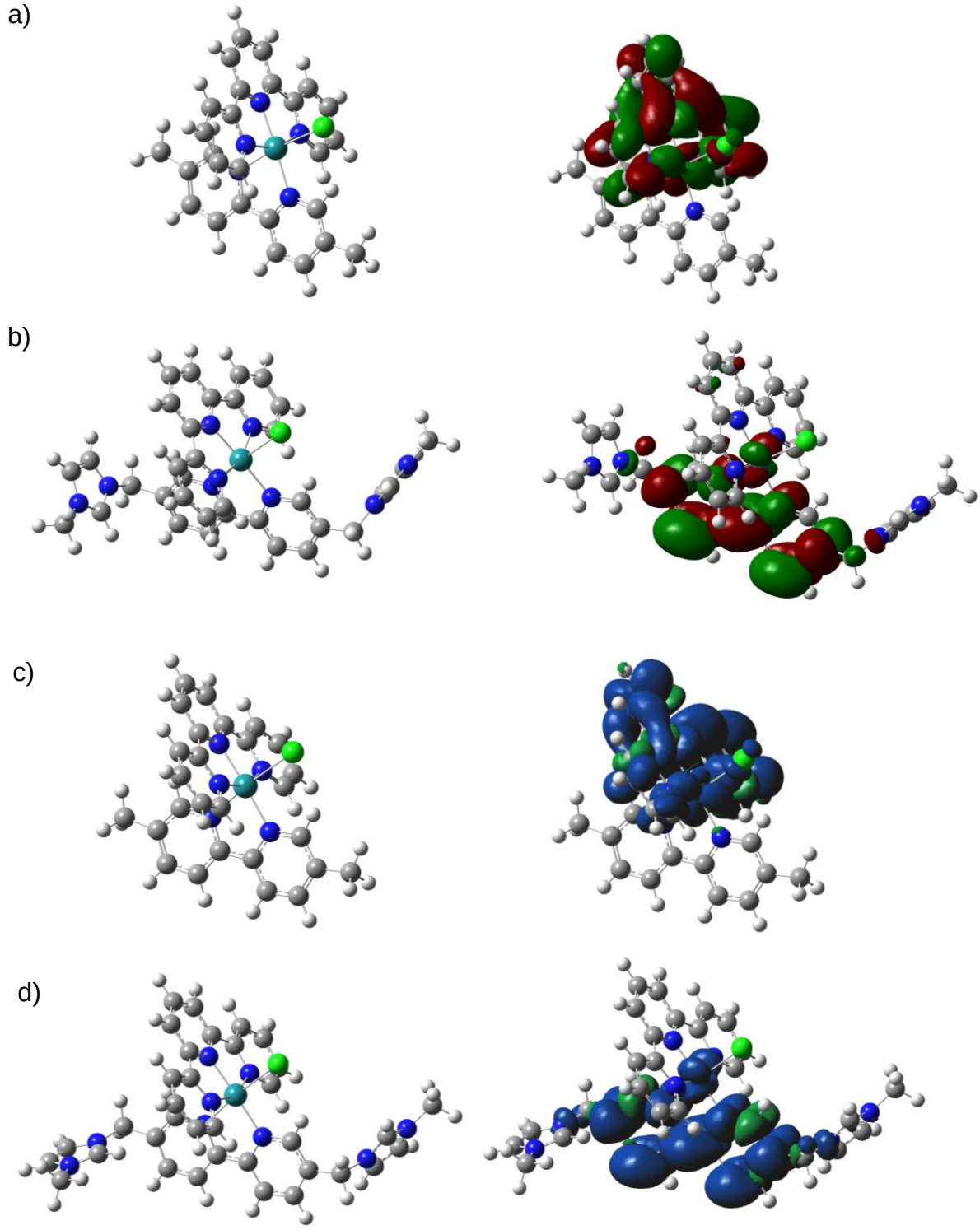

Figure 5. Structures and plots of orbitals obtained for non-reduced a) **[Ru_Im]**$^{3+}$ and b) **[Ru_Me]**$^{+}$ (singlet). Structures and spin density maps obtained for singly-reduced c) **[Ru_Im]**$^{3+}$ and d) **[Ru_Me]**$^{+}$ (doublet). Optimized at the B3LYP or UB3LYP/LanL2DZ level under DMF solvated model (PCM, polarizable continuum model). Other details are supplied in Experimental Section. Geometry is shown in Table 5-8 of the Appendix part in page 163-173.

Electrochemical CO_2 Reduction

Catalytic activity for electrochemical CO_2 reduction of **[Ru_Im]$^{3+}$** and **[Ru_Me]$^{+}$** under CO_2 atmosphere was evaluated using three kinds of electrolyte solutions (DMF, MeCN, and DMSO) in order to investigate the effects of the solvent on the catalytic activity in detail. When DMF is used as an electrolyte solution, in the case of **[Ru_Me]$^{+}$**, catalytic current for CO_2 reduction flows after the first reduction occurs (see Figure 6a). Therefore, CO_2 reduction catalyzed by **[Ru_Me]$^{+}$** is considered to be triggered by the second reduction (i.e., one electron reduction at the dmbpy ligand). For comparison, in the case of **[Ru_Im]$^{3+}$**, catalytic current flows after the second reduction proceeds (see Figure 6b), indicating that CO_2 reduction catalyzed by **[Ru_Im]$^{3+}$** proceeds coupled with the third reduction. This difference is reasonably understood that the two electron reduced species of **[Ru_Im]$^{3+}$** does not possess a sufficient driving force for CO_2 reduction due to the positive shift of the first and the second reduction waves. Importantly, CO evolved could be detected by gas phase analysis during the controlled potential electrolysis of **[Ru_Im]$^{3+}$** at -2.33 V vs. Fc/Fc^{+} in DMF (see Experimental Section for details). Because the solution does not include proton source and the reaction eq. 1 can be ruled out in the present system, it is concluded that the reaction eq. 2 proceeds at this potential.

$$CO_2 + 2H^{+} + 2e^{-} \rightarrow CO + H_2O \quad (1)$$

$$2CO_2 + 2e^{-} \rightarrow CO + CO_3^{2-} \quad (2)$$

In the reaction eq. 2, a second CO_2 acts as oxide acceptor and form CO_3^{2-} as observed in previous studies.[8b,29] The i_{cat}/i_p value, which is the ratio between the catalytic peak current under CO_2 (i_{cat}) and the one-electron reduction peak current under Ar (i_p), for **[Ru_Im]$^{3+}$** (3.3) is almost same to that for **[Ru_Me]$^{+}$** (2.9), indicating that these two complexes exhibit comparable catalytic activity under these conditions.

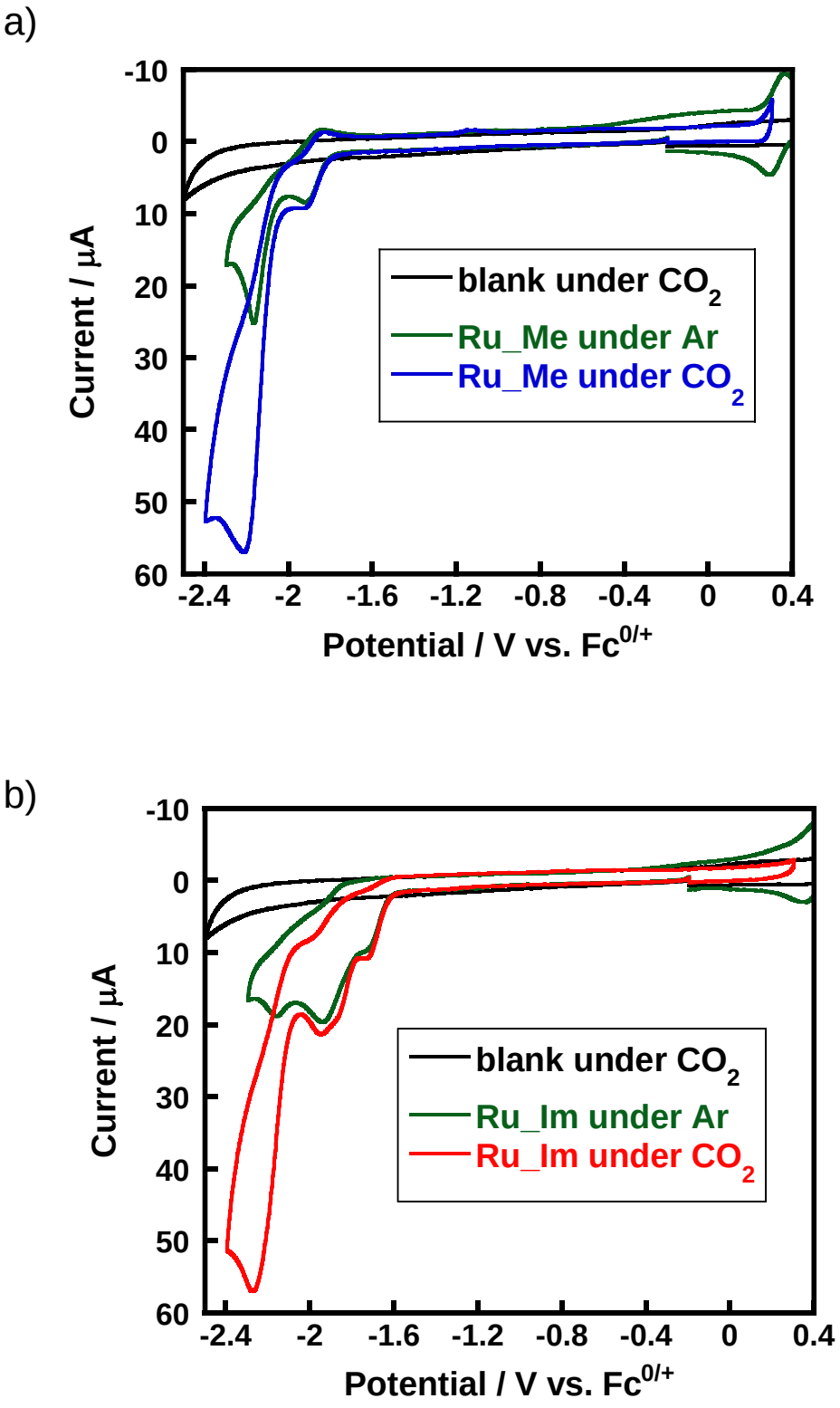

Figure 6. CVs for a DMF solution of a) **[Ru_Me]**$^{+}$ and b) **[Ru_Im]**$^{3+}$. Measurements were carried out for a 0.5 mM solution of the complex in DMF containing 0.1 M tetra(*n*-butyl)ammonium hexafluorophosphate (TBAH) at room temperature under Ar or CO_2 atmosphere, recorded at a sweep rate of 100 mV s^{-1}.

On the other hand, when MeCN is used as an electrolyte solution, **[Ru_Im]$^{3+}$** shows opposite trends to **[Ru_Me]$^{+}$** (see Figure 7). As listed in Table 2, the i_{cat}/i_p value of **[Ru_Me]$^{+}$** in acetonitrile (9.2) is about 3 times larger than that in DMF (2.9) while that of **[Ru_Im]$^{3+}$** in MeCN (1.8) is about 1.5 times lower compared to that in DMF (3.3). These results indicate that the introduction of **Im** moieties changes solvent effects on the reaction. Moreover, when DMSO is used, **[Ru_Im]$^{3+}$** exhibits similar catalytic activity compared to that in DMF (see Figure 8). The i_{cat}/i_p value of **[Ru_Im]$^{3+}$** in DMSO (2.9) is similar to that in DMF (3.3).

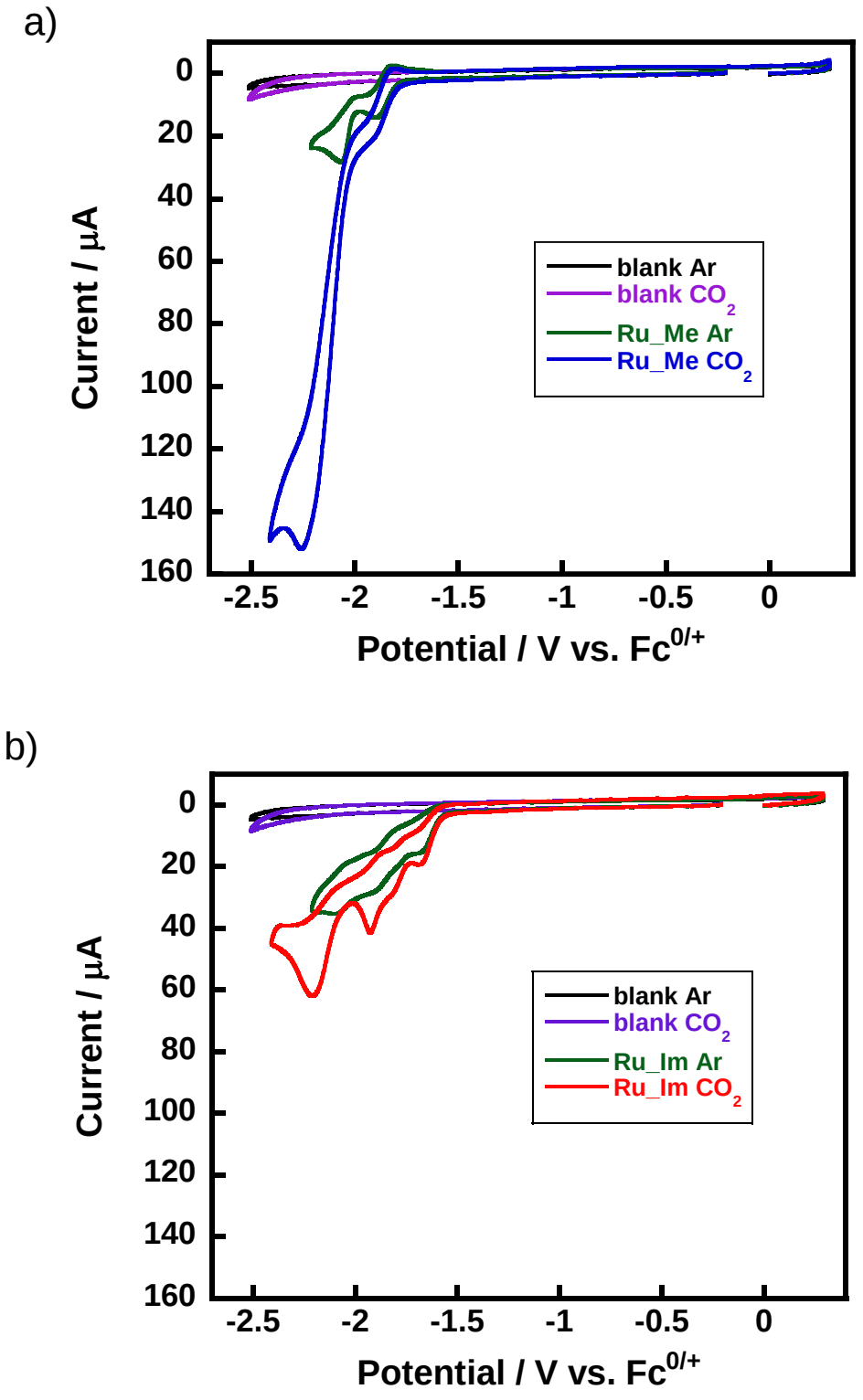

Figure 7. CVs for a MeCN solution of a) **[Ru_Me]**$^{+}$ and b) **[Ru_Im]**$^{3+}$. Measurements were carried out for a 0.5 mM solution of the complex in MeCN containing 0.1 M tetra(*n*-butyl)ammonium hexafluorophosphate (TBAH) at room temperature under Ar or CO_2 atmosphere, recorded at a sweep rate of 100 mV s^{-1}.

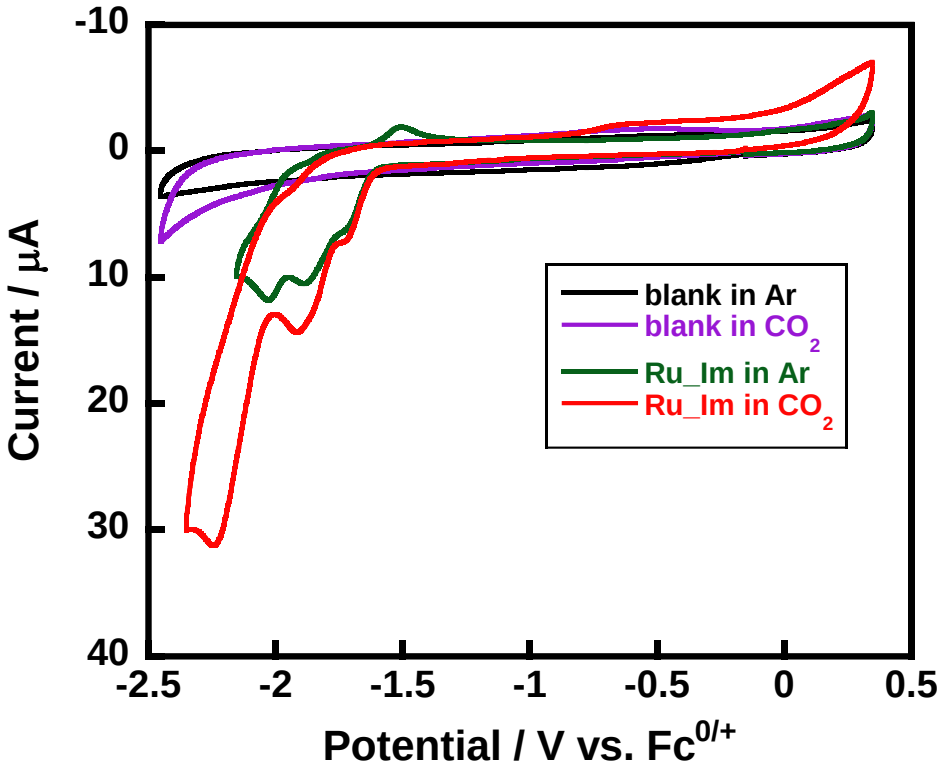

Figure 8. CVs for a DMSO solution of **[Ru_Im]**$^{3+}$. Measurements were carried out for a 0.5 mM solution of the complex in DMSO containing 0.1 M tetra(*n*-butyl)ammonium hexafluorophosphate (TBAH) at room temperature under Ar or CO_2 atmosphere, recorded at a sweep rate of 100 mV s^{-1}.

Table 2. Selected donor number (DN) and acceptor number (AN) parameters[30] and i_{cat}/i_p values for **[Ru_Im]**$^{3+}$ and **[Ru_Me]**$^{+}$.

	DN	**AN**	i_{cat}/i_p for **[Ru_Im]**$^{3+}$	i_{cat}/i_p for **[Ru_Me]**$^{+}$
H_2O	33	54.8		
MeCN	14.1	19.3	1.8	9.2
DMF	26.6	16.0	3.3	2.9
DMSO	29.8	19.3	2.9	

This unexpected solvent dependence on the catalytic activity is considered to be derived from the Lewis basicity and the acidity of the solvent, which are defined as the donor number (DN) and the acceptor number (AN).[30] In the case of **[Ru_Me]**$^{+}$, catalytic activity in MeCN is higher than those in DMF. As summarized in Table 2, because the AN of MeCN (19.3) is higher than that for DMF (16.0), MeCN is a stronger Lewis acid. Therefore, when MeCN is used as an electrolyte solution, formation of the hydrogen bond between hydrogen atoms of MeCN and CO_2 activated on the metal ion possibly stabilize CO_2-bound intermediates (see Figure 9). The similar tendency was reported in the previous study, where a Re complex shows higher activity for electrocatalytic CO_2 reduction in MeCN than that in DMF.[31]

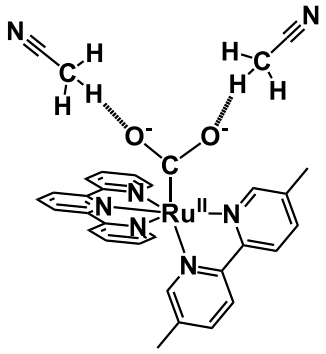

Figure 9. Speculated structure of the CO_2-bound **[Ru_Me]**$^{+}$ forming intermolecular hydrogen bond with MeCN molecules.

For comparison, in the case of **[Ru_Im]$^{3+}$**, Lewis basicity of solvents is likely to strongly affect in catalytic activity. As shown in Table 2, DN values of DMF (26.6) and DMSO (29.8) are higher than that of MeCN (14.1), indicating that DMF and DMSO have higher Lewis basicity. As with the **Fe_OH** system (see Figure 1b) mentioned in Introduction part,[7] solvents can form hydrogen bonds with **Im** moieties of **[Ru_Im]$^{3+}$**. Figure 10 shows speculated structures of CO_2-bound **[Ru_Im]$^{3+}$** forming intramolecular hydrogen-bond interactions between the CO_2 molecule and an **Im** moiety (A in Figure 10) which is in equilibrium with the solvent-related B state. In consideration of eq. 2, the A state is probably unfavorable because an **Im** group shields an activated CO_2 from another CO_2 (A in Figure 10). It is important to emphasize that the reaction of eq. 2 should have much slower kinetics than that coupled with protons (eq. 1) for usual CO_2 reduction systems.[2c,32] On the other hand, the reaction of eq. 2 can more easily proceed in the B state because of the reduced steric hindrance around an activated CO_2 compared to the A state (see Figure 10).

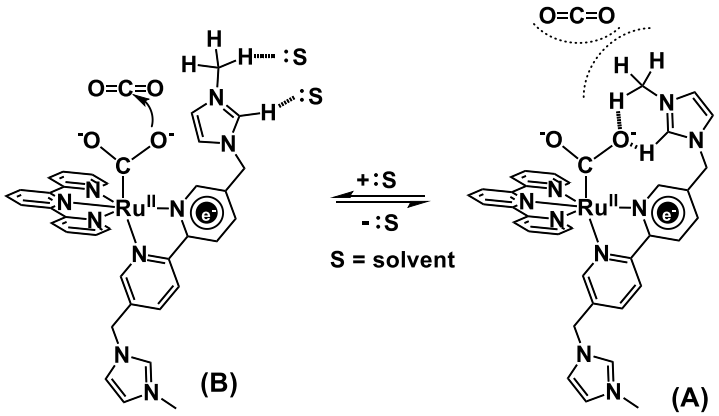

Figure 10. Speculated structures of CO_2-bound **[Ru_Im]$^{3+}$** forming (A) intra or (B) intermolecular hydrogen bonds.

Figure 11 shows a speculated catalytic cycle of CO_2 reduction by **[Ru_Im]$^{3+}$**. In this reaction, it is considered that CO formation by oxide transfer can only proceed from the 3B state (3B to 4 in Figure 11) due to slower kinetics of that from the 3A state. Therefore, it is assumed that the population of the 3B state is higher in DMF having a higher ability to form hydrogen bond with **Im** sites compared to that in MeCN, resulting in the much higher catalytic activity in DMF. Importantly, this indicates that the introduction of **Im** moieties has possibility to inhibit catalytic reactions depending on the situation.

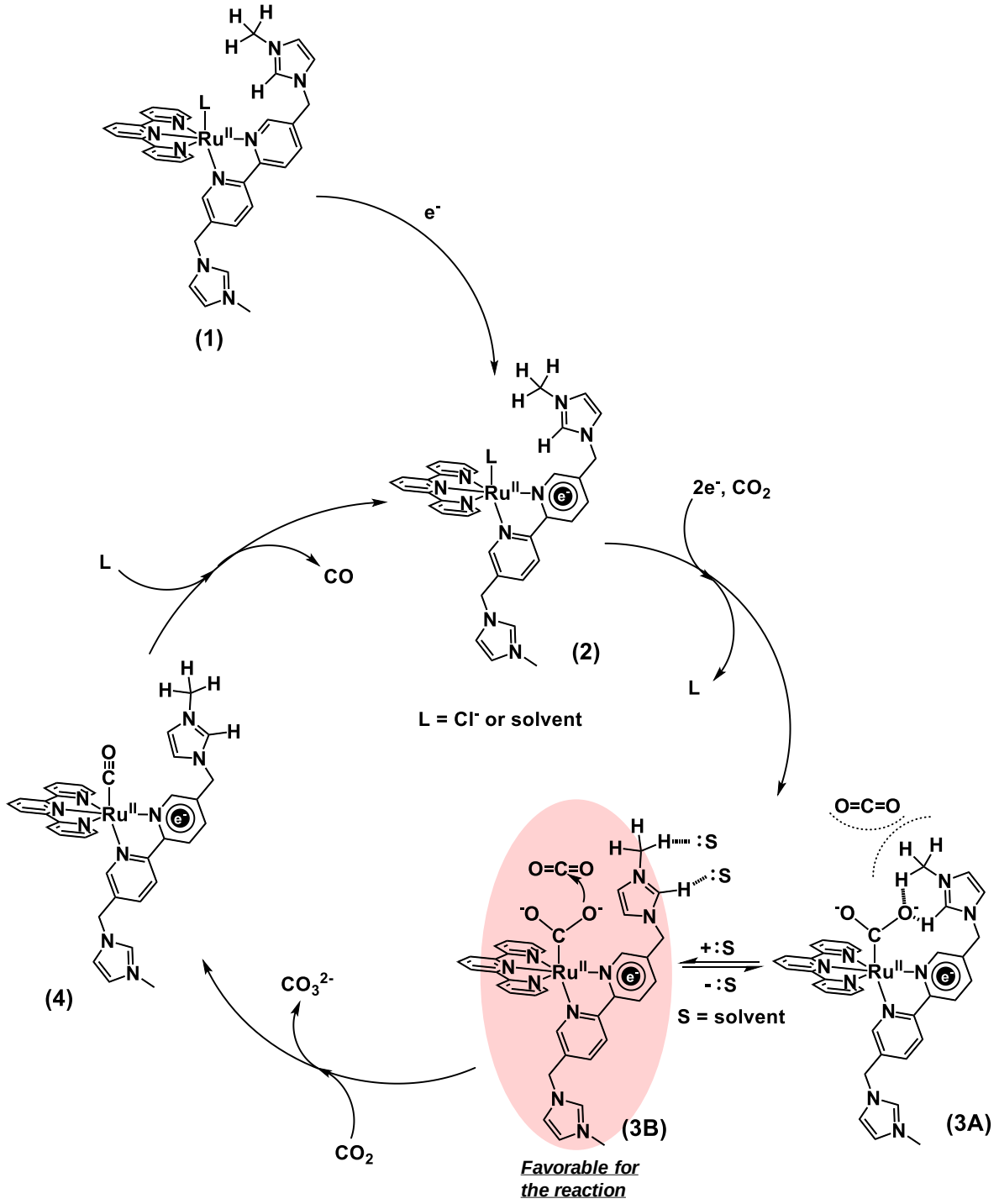

Figure 11. A speculated catalytic cycle for **[Ru_Im]**$^{3+}$.

Conclusions

In this study, properties of a new Ru complex having **Im** moieties, **[Ru_Im]**$^{3+}$, were investigated using experimental and theoretical methods. The investigation of electrochemical behaviors by CVs and DFT calculation reveals the very strong stabilization of π* orbital of the ligand by introducing **Im** moieties even via the methylene linker. Furthermore, it is revealed that catalytic activities of **[Ru_Im]**$^{3+}$ for CO_2 reduction strongly depends on Lewis basicity of the solvent (see Figure 12), which is probably derived from inhibition of the reaction by **Im** moieties. Some new insights obtained in this study should give benefits to develop new CO_2-reducing systems using not only **Im** species but also some other cationic species.

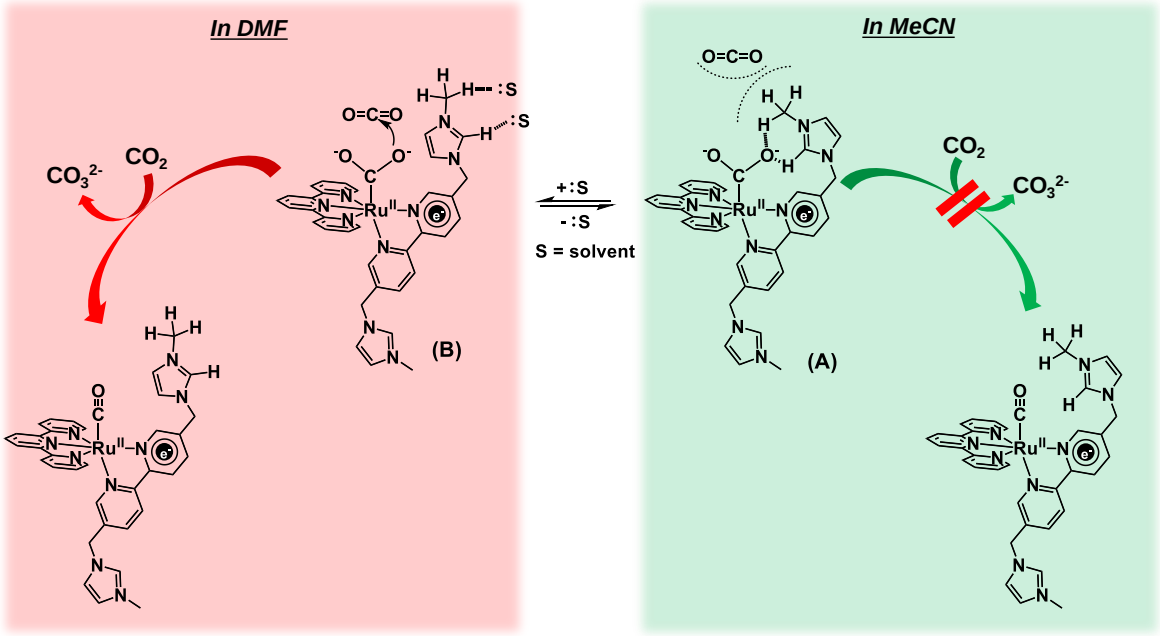

Figure 12. Schematic representation of CO_2 reduction by **[Ru_Im]**$^{3+}$.

References

1. H. B. Gray, *Nat. Chem.*, 2009, **1**, 7.
2. (a) H. Takeda, C. Cometto, O. Ishitani and M. Robert, *ACS Catal.*, 2017, **7**, 70.

   (b) N. Elgrishi, M. B. Chambers, X. Wang and M. Fontecave, *Chem. Soc. Rev.*, 2017, **46**, 761.

   (c) R. Francke, B. Schille and M. Roemelt, *Chem. Rev.*, 2018, **118**, 4631.
3. Q. Lu and F. Jiao, *Nano Energy*, 2016, **29**, 439.
4. (a) C. Costentin, S. Drouet, M. Robert and J.-M. Savéant, *Science*, 2012, **338**, 90.

   (b) F. Franco, C. Cometto, L. Nencini, C. Barolo, F. Sordello, C. Minero, J. Fiedler, M. Robert, R. Gobetto and C. Nervi, *Chem. Eur. J.*, 2017, **23**, 4782.

   (c) A. Chapovetsky, T. H. Do, R. Haiges, M. K. Takase and S. C. Marinescu, *J. Am. Chem. Soc.*, 2016, **138**, 5765.

   (d) H. Sheng and H. Frei, *J. Am. Chem. Soc.*, 2016, **138**, 9959.

   (e) I. Azcarate, C. Costentin, M. Robert and J.-M. Savéant, *J. Am. Chem. Soc.*, 2016, **138**, 16639.
5. S. Sung, D. Kumar, M. Gil-Sepulcre, and M. Nippe, *J. Am. Chem. Soc.*, 2017, **139**, 13993.
6. A. Khadhraoui, P. Gotico, B. Boitrel, W. Leibl, Z. Halime and A. Aukauloo, *Chem. Commun.*, 2018, **54**, 11630.
7. S. Sinha and J. J. Warren, *Inorg. Chem.*, 2018, **57**, 12650.
8. (a) H. Nagao, T. Mizukawa and K. Tanaka, *Inorg. Chem.*, 1994, **33**, 3415.

   (b) Z. Chen, C. Chen, D. R. Weinberg, P. Kang, J. J. Concepcion, D. P. Harrison, M. S. Brookhart and T. J. Meyer, *Chem. Commun.*, 2011, **47**, 12607.
9. S. Park, S.-H. Moon, T. H. Kima and K.-M. Park, *Acta Cryst.*, 2011, E67, o2392.
10. B. P. Sullivan, J. M. Calvert and T. J. Meyer, *Inorg. Chem.*, 1980, **19**, 1404.
11. M. J. Frisch *et al*., Gaussian 09 Revision C.01 (Gaussian Inc., Wallingford CT, 2009).
12. A. D. Becke, *J. Chem. Phys.*, 1993, **98**, 5648.

13. C. Lee, W. Yang and R. G. Parr, *Phys. Rev. B*, 1988, **37**, 785.
14. V. Barone, M. Cossi and J. Tomasi, *J. Comp. Chem.*, 1998, **19**, 404.
15. M. Cossi, G. Scalmani, N. Rega and V. Barone, *J. Chem. Phys.*, 2002, **117**, 43.
16. J. Tomasi, B. Mennucci and R. Cammi, *Chem. Rev.*, 2005, **105**, 2999.
17. T. H. Dunning and P. J. Hay, in *Modern Theoretical Chemistry*, ed. H. F. Schaefer III, Plenum, New York, NY, USA, 1976, p. 1.
18. P. J. Hay and W. R. Wadt, *J. Chem. Phys.*, 1985, **82**, 270.
19. P. J. Hay and W. R. Wadt, *J. Chem. Phys.*, 1985, **82**, 299.
20. M. T. Huynh, W. Wang, T. B. Rauchfuss and S. Hammes-Schiffer, *Inorg. Chem.*, 2014, **53**, 10301.
21. D. K. Bediako, B. H. Solis, D. K. Dogutan, M. M. Roubelakis, A. G. Maher, C. H. Lee, M. B. Chambers, S. Hammes-Schiffer and D. G. Nocera, *Proc. Natl. Acad. Sci. USA*, 2014, **111**, 15001.
22. B. H. Solis and S. Hammes-Schiffer, *Inorg. Chem.*, 2014, **53**, 6427.
23. B. H. Solis, A. G. Maher, D. K. Dogutan, D. G. Nocera and S. Hammes-Schiffer, *Proc. Nat. Acad. Sci. USA*, 2016, **113**, 485.
24. B. H. Solis and S. Hammes-Schiffer, *J. Am. Chem. Soc.*, 2011, **133**, 19036.
25. B. H. Solis and S. Hammes-Schiffer, *Inorg. Chem.*, 2011, **50**, 11252.
26. S. Chen, R. Rousseau, S. Raugei, M. Dupuis, D. L. DuBois and R. M. Bullock, *Organometallics*, 2011, **30**, 6108.
27. B. H. Solis, A. G. Maher, T. Honda, D. C. Powers, D. G. Nocera and S. Hammes-Shiffer, *ACS Catal.*, 2014, **4**, 4516.
28. B. A. Anjali, F. B. Sayyed, C. H. Suresh, *J. Phys. Chem. A*, 2016, **120**, 1112.
29. (a) B. A. Johnson, S. Maji, H. Agarwala, T. A. White, E. Mijangos and S. Ott, *Angew. Chem. Int. Ed.*, 2016, **55**, 1825.

(b) S. Ramakrishnan and C. E. D. Chidsey, *Inorg. Chem.*, 2017, **56**, 8326.

30. V. Gutmann, *Electrochim. Acta*, 1976, **21**, 661.
31. J. K. Nganga, C. R. Samanamu, J. M. Tanski, C. Pacheco, C. Saucedo, V. S. Batista, K. A. Grice, M. Z. Ertem and A. M. Angeles-Boza, *Inorg. Chem.*, 2017, **56**, 3214.
32. (a) C. W. Machan, J. Yin, S. A. Chabolla, M. K. Gilson and C. P. Kubiak, *J. Am. Chem. Soc.*, 2016, **138**, 8184.

(b) A. Nakada and O. Ishitani, *ACS Catal.*, 2018, **8**, 354.

(c) C. Cometto, L. Chen, P.-K. Lo, Z. Guo, K.-C. Lau, E. Anxolabéhère-Mallart, C. Fave, T.-C. Lau and M. Robert, *ACS Catal.*, 2018, **8**, 3411.

Concluding Remarks

Artificial photosynthesis is one of the most promising way to solve some crucial problems in the modern society, such as shortage of natural resources, environment pollution, and climate changes. Therefore, many efforts have been made to develop catalysts promoting reactions related to artificial photosynthesis, water splitting and CO_2 reduction. On the other hand, researchers have paid attention to natural enzymes which can efficiently promote H_2 evolution, water oxidation, and CO_2 reduction in order to make guidelines to develop efficient artificial systems. Importantly, high efficiencies of these enzymes strongly depend on sophisticated reaction fields around substrate-binding sites, where functional sites, such as electron and proton mediators, are placed on suitable positions. In this context, many efforts have been made to construct efficient reaction fields like natural systems within single molecular architectures by introducing some functional moieties into catalysts based on metal complexes. Among these systems, metal complexes having cationic functional sites recently have been attracted attention and shown high efficiencies of catalysis and unique properties. For example, Pt(II) complexes having methylviologen (MV^{2+}) moieties were reported as highly efficient **PHEMD**s (photo-hydrogen-evolving molecular devices) acting as a photosensitizer and a catalyst for photochemical H_2 evolution. Additionally, some studies showed that some Ru(II) complexes covalently linked multiple MV^{2+} moieties demonstrate unique photo-driven multi-electron storage within single molecular architectures as photo-charge-separators (**PCS**s), leading to H_2 evolution in the presence of catalyst. Furthermore, it was reported that the introduction of imidazolium sites into structures of metal complexes leads to enhancement of catalytic activities compared to those without functionalization. However, in spite of these efforts, detailed effects of introduction of cationic moieties are still unclear and required to be investigated. In this thesis, the author investigated these effects for polypyridyl Pt(II) and Ru(II) complexes having cationic functional moieties.

Chapter 1 and 2 focus on structural effects on catalytic behaviors of Pt-MV^{2+} type **PHEMD**s and Ru-MV^{2+} type multi-electron storage systems. As a result, the author succeeded in fine control of electron transfer processes and catalytic processes for these photocatalytic systems.

In Chapter 1, a new **PHEMD**, **$[PtCl_2(bpyMV2)]^{4+}$**, was synthesized and characterized to investigate effects of distances between functional sites for Pt(II)-MV^{2+} type **PHEMD**s. In **$[PtCl_2(bpyMV2)]^{4+}$**, MV^{2+} moieties are connected to Pt(II) complex site with shorter linkers than those of the previous systems. In this study, it is revealed that **$[PtCl_2(bpyMV2)]^{4+}$** drives photocatalytic H_2 evolution only via formation of triply-reduced species while the previous systems conduct H_2 evolution via formation of doubly-reduced species. It was assumed this difference of catalytic mechanisms is derived from the faster intramolecular electron transfer from the Pt(II) complex site to MV^{2+} sites in the present system compared to those in the previous systems. Importantly, this study also shows that the reduced bipyridine site is required to promote H_2 evolution in photocatalytic systems using Pt-MV^{2+} type **PHEMD**s. The study in Chapter 1 showed not only the strong impact of the distance of functional sites on catalytic mechanisms but also a key factor for Pt-MV^{2+} type **PHEMD**s.

In Chapter 2, with ligand used in Chapter 1, a new **PCS** having MV^{2+} acceptors, **$[Ru(bpyMV2)_3]^{14+}$**, was synthesized and its application in photocatalytic H_2 evolution was reported. The present **PCS** possesses shorter linkers in connecting a Ru chromophore and MV^{2+} acceptors in comparison with previous **PCS**s and shows consecutive photo-driven electron transfer in the presence of a sacrificial electron donor (EDTA), leading to multi-electron storage over the **PCS**. Importantly, while almost all electrons were stored in the form of the MV^{2+} radical dimer, $(MV^{+})_2$, which is formed from two radical monomers ($MV^{+\bullet}$) in the previous **PCS**s, partial electrons were stored in the form of $MV^{+\bullet}$ in the **$[Ru(bpyMV2)_3]^{14+}$** system. This resulted in more efficient H_2 evolution of the present system in the presence of colloidal Pt as a catalyst than that of the previous system because $MV^{+\bullet}$ has higher driving force for H_2 evolution compared to $(MV^{+})_2$. Furthermore, this efficient consumption of stored electrons in the present system inhibited undesired side reactions and elongated the stability of

the catalytic system, resulting in evolution of a higher amount of H_2 compared to the previous system. In this study, it was revealed that storage of $MV^{+\bullet}$ moieties is a key factor to develop efficient H_2-evolving systems based on **PCS**s.

In Chapter 3, a new Ru(II) complex having imidazolium moieties, **[Ru_Im]$^{3+}$**, was synthesized and its behavior as a electrocatalyst for CO_2 reduction was investigated. In this study, experimental and theoretical studies revealed the strong stabilization of π^* orbital of ligands by the electron-withdrawing effect of imidazolium groups even via methylene linkers. Furthermore, it is revealed that catalytic activity of **[Ru_Im]$^{3+}$** is affected by Lewis basicity of the solvent derived from the inhibition effect of imidazolium moieties. This study showed unique properties of imidazolium moieties and a possibility to lower catalytic activity by introducing these functional groups.

These results provide useful information for development of highly efficient cation-functionalized catalysts for artificial photosynthesis. The author expects that these studies contribute to the global projects tackling the problems in the Earth.

Appendix

Tables for results of DFT and TDDFT calculations in Chapter 1

Table 1. Geometry optimized by DFT for the closed-shell singlet state of the two-electron-reduced form of **$[PtCl_2(bpyMV2)]^{4+}$**, i.e., **$[PtCl_2(bpy)\text{-}(MV^+)_2]^{2+}$**. Optimized at the M06/SDD(Pt)/6-31G**(HCNOCl) level using PCM.[a]

Atom	X	Y	Z
Pt1	-5.249545	0.228408	0.201542
N2	-3.542235	1.261716	-0.293436
C3	-1.102116	2.417406	-0.916936
C4	-2.436754	0.484640	-0.426765
C5	-3.450680	2.584815	-0.482337
C6	-2.246031	3.200367	-0.788690
C7	-1.211133	1.042046	-0.755438
H8	-4.376560	3.142772	-0.373572
H9	-2.218195	4.276226	-0.934150
H10	-0.326874	0.425648	-0.887134
N11	-3.926446	-1.330054	0.006783
C12	-1.941355	-3.241449	-0.276308
C13	-4.225969	-2.635580	0.095807
C14	-2.649084	-0.949614	-0.241214
C15	-1.635468	-1.888552	-0.350821
C16	-3.264355	-3.618227	-0.070665

H17	-5.268965	-2.865971	0.295146
H18	-0.615794	-1.562670	-0.532307
H19	-3.540451	-4.667227	-0.038607
Cl20	-6.620087	2.138628	0.361161
Cl21	-7.086147	-1.125046	0.793697
C22	0.236004	2.966253	-1.322535
C23	-0.903180	-4.285572	-0.552521
O24	0.869947	2.405067	-2.210544
O25	-1.191904	-5.301681	-1.168229
N26	0.663082	4.090645	-0.698170
H27	1.528015	4.461066	-1.080117
N28	0.354217	-3.987409	-0.135296
H29	0.499149	-3.230096	0.518255
C30	0.290095	4.536328	0.633196
H31	-0.550313	3.933429	0.986874
H32	-0.062407	5.573726	0.615503
C33	1.454263	4.456920	1.611828
H34	2.186595	5.238698	1.388581
H35	1.080424	4.639161	2.626532
C36	1.472917	-4.828348	-0.508183
H37	2.221536	-4.806834	0.290486
H38	1.115346	-5.857978	-0.609781
C39	2.085042	-4.387699	-1.832360
H40	2.818028	-5.122962	-2.177313
H41	1.305843	-4.309504	-2.598035

N42	2.175749	3.180532	1.566808
C43	3.609028	0.736601	1.615592
C44	1.517038	1.978976	1.525085
C45	3.539461	3.170105	1.598949
C46	4.250036	2.008042	1.644175
C47	2.181803	0.790818	1.523477
H48	0.432251	2.025607	1.523173
H49	4.026502	4.140683	1.616210
H50	5.330088	2.098665	1.697041
H51	1.576840	-0.110832	1.489154
C52	4.336968	-0.482606	1.737513
N53	5.778807	-2.888551	2.087604
C54	3.703820	-1.757466	1.774662
C55	5.759439	-0.514822	1.884854
C56	6.430812	-1.690676	2.037298
C57	4.423399	-2.904663	1.939361
H58	2.627428	-1.860553	1.680976
H59	6.351951	0.393185	1.894777
H60	7.509823	-1.731768	2.145981
H61	3.955154	-3.883320	1.986920
N62	2.760640	-3.091438	-1.725625
C63	4.068626	-0.608168	-1.394519
C64	2.087709	-1.915480	-1.922491
C65	4.069232	-3.040184	-1.345914
C66	4.728783	-1.854509	-1.209001

C67	2.688622	-0.702082	-1.755967
H68	1.064384	-2.010709	-2.273831
H69	4.561892	-3.997361	-1.194368
H70	5.779681	-1.905171	-0.945873
H71	2.090626	0.182983	-1.964795
C72	4.766024	0.637070	-1.298242
N73	6.167775	3.081714	-1.177018
C74	4.125230	1.890539	-1.497575
C75	6.168030	0.705820	-1.035342
C76	6.818968	1.902344	-0.970919
C77	4.827537	3.059708	-1.422025
H78	3.062278	1.967854	-1.717944
H79	6.767729	-0.186173	-0.894031
H80	7.883409	1.973125	-0.771503
H81	4.360875	4.028996	-1.571073
C82	6.854366	4.359222	-1.010633
H83	6.676780	4.754878	-0.004773
H84	6.483276	5.071443	-1.750398
H85	7.925598	4.217797	-1.159795
C86	6.515760	-4.145738	2.166768
H87	7.496359	-3.964950	2.609210
H88	6.641530	-4.575275	1.166982
H89	5.967889	-4.849958	2.796414

---

[a]Part of the Gaussian output file:

SCF Done: E(RM06) = -3097.51161660 A.U. after 6 cycles

	1	2	3
	A	A	A
Frequencies --	23.3941	35.1806	41.5035
Red. masses --	7.6593	5.8555	7.0154

Zero-point correction= 0.717285 (Hartree/Particle)

Thermal correction to Energy= 0.762366

Thermal correction to Enthalpy= 0.763310

Thermal correction to Gibbs Free Energy= 0.641062

Sum of electronic and zero-point Energies= -3096.794332

Sum of electronic and thermal Energies= -3096.749250

Sum of electronic and thermal Enthalpies= -3096.748306

Sum of electronic and thermal Free Energies= -3096.870554

Item	Value	Threshold	Converged?
Maximum Force	0.000414	0.000450	YES
RMS Force	0.000056	0.000300	YES

Table 2. Geometry optimized by DFT for the open-shell singlet state of the two-electron-reduced form of **$[PtCl_2(bpyMV2)]^{4+}$**, i.e., **$[PtCl_2(bpy)\text{-}(MV^{+})_2]^{2+}$**. Optimized at the UM06/SDD(Pt)/6-31G**(HCNOCl) level of broken symmetry approach using PCM.[a]

Atom	X	Y	Z	Spin Density
Pt1	-5.272313	0.227367	0.189126	0.000000
N2	-3.547715	1.269015	-0.219298	0.000003
C3	-1.106439	2.426963	-0.833064	-0.000004
C4	-2.442930	0.491751	-0.356777	-0.000004
C5	-3.452869	2.594521	-0.389175	-0.000003
C6	-2.247281	3.211467	-0.689031	0.000004
C7	-1.217036	1.050732	-0.680656	0.000004
H8	-4.378712	3.152063	-0.277798	0.000000
H9	-2.218136	4.288612	-0.824473	0.000000
H10	-0.334337	0.434955	-0.824071	0.000000
N11	-3.940610	-1.327754	0.025013	-0.000002
C12	-1.945760	-3.234947	-0.225394	0.000002
C13	-4.238948	-2.634201	0.103299	0.000002
C14	-2.657830	-0.944269	-0.189357	0.000002
C15	-1.640356	-1.881094	-0.283592	-0.000003
C16	-3.272037	-3.614117	-0.046626	-0.000003
H17	-5.285600	-2.868242	0.277389	0.000000
H18	-0.617776	-1.551111	-0.440918	0.000000
H19	-3.547119	-4.663634	-0.025100	0.000000
Cl20	-6.642581	2.140434	0.340110	0.000000

Cl21	-7.144680	-1.139864	0.625737	0.000000
C22	0.225783	2.973078	-1.260827	0.000001
C23	-0.905757	-4.279190	-0.495078	0.000000
O24	0.843896	2.407168	-2.156926	0.000000
O25	-1.193891	-5.296027	-1.110154	0.000000
N26	0.661841	4.102507	-0.652083	0.000000
H27	1.518044	4.473422	-1.052750	0.000000
N28	0.351950	-3.983078	-0.077322	0.000000
H29	0.500676	-3.226370	0.576190	0.000000
C30	0.321745	4.543045	0.689953	0.000000
H31	-0.507666	3.936793	1.063583	0.000000
H32	-0.033813	5.579502	0.684521	0.000000
C33	1.512039	4.464614	1.636029	0.000000
H34	2.239089	5.244001	1.388103	0.000000
H35	1.167485	4.651869	2.660176	0.000000
C36	1.467558	-4.827531	-0.452601	0.000000
H37	2.224027	-4.796405	0.338146	0.000000
H38	1.110363	-5.858659	-0.539400	0.000000
C39	2.066927	-4.401672	-1.787596	0.000000
H40	2.795740	-5.141624	-2.131127	0.000000
H41	1.281058	-4.331063	-2.547100	0.000000
N42	2.230017	3.186449	1.575761	0.000000
C43	3.661551	0.740585	1.603094	0.000001
C44	1.570201	1.985351	1.536158	0.000001
C45	3.594073	3.174466	1.591974	0.000001

C46	4.304052	2.011584	1.625239	-0.000002
C47	2.233346	0.796318	1.526252	-0.000001
H48	0.485642	2.032448	1.543989	0.000000
H49	4.082217	4.144649	1.604987	0.000000
H50	5.384861	2.100715	1.663672	0.000000
H51	1.626113	-0.104222	1.495797	0.000000
C52	4.389956	-0.479005	1.714974	0.000001
N53	5.833368	-2.886303	2.047980	0.000000
C54	3.755279	-1.752513	1.767740	-0.000002
C55	5.814962	-0.513263	1.835689	-0.000001
C56	6.486621	-1.689819	1.980612	0.000001
C57	4.475491	-2.900403	1.924087	0.000002
H58	2.677047	-1.852742	1.693502	0.000000
H59	6.409493	0.393502	1.830018	0.000000
H60	7.567383	-1.732675	2.069284	0.000000
H61	4.006450	-3.878034	1.983455	0.000000
N62	2.744966	-3.105238	-1.701881	0.000000
C63	4.055381	-0.619222	-1.404802	0.000001
C64	2.067289	-1.931140	-1.892042	0.000001
C65	4.060560	-3.050901	-1.347959	0.000001
C66	4.721162	-1.863706	-1.229047	-0.000001
C67	2.669197	-0.716310	-1.739931	-0.000001
H68	1.038599	-2.027852	-2.226468	0.000000
H69	4.557375	-4.006760	-1.201788	0.000000
H70	5.776762	-1.911715	-0.985046	0.000000

H71	2.067226	0.167259	-1.942992	0.000000
C72	4.751582	0.628070	-1.325397	0.000000
N73	6.149014	3.075979	-1.249109	0.000000
C74	4.100240	1.879471	-1.500203	-0.000001
C75	6.160570	0.700274	-1.104861	0.000000
C76	6.809769	1.898727	-1.062522	0.000000
C77	4.801081	3.050686	-1.447296	0.000001
H78	3.028307	1.952689	-1.673399	0.000000
H79	6.766772	-0.190014	-0.981621	0.000000
H80	7.879826	1.972849	-0.897703	0.000000
H81	4.326828	4.019165	-1.576965	0.000000
C82	6.837994	4.355171	-1.108229	0.000000
H83	6.688599	4.754820	-0.099347	0.000000
H84	6.445318	5.063642	-1.840474	0.000000
H85	7.904747	4.214322	-1.287194	0.000000
C86	6.569937	-4.144245	2.117913	0.000000
H87	7.556796	-3.964178	2.546573	0.000000
H88	6.681443	-4.575008	1.116973	0.000000
H89	6.030261	-4.847405	2.755702	0.000000

---

[a]Part of the Gaussian output file:

SCF Done: E(UM06) = -3097.51162153 A.U. after 29 cycles

Annihilation of the first spin contaminant:

S**2 before annihilation 0.0000, after 0.0000

	1	2	3
	A	A	A
Frequencies --	18.4220	34.2255	36.9745
Red. masses --	7.6063	5.8037	6.6053

Zero-point correction= 0.716808 (Hartree/Particle)

Thermal correction to Energy= 0.762144

Thermal correction to Enthalpy= 0.763088

Thermal correction to Gibbs Free Energy= 0.639537

Sum of electronic and zero-point Energies= -3096.794814

Sum of electronic and thermal Energies= -3096.749477

Sum of electronic and thermal Enthalpies= -3096.748533

Sum of electronic and thermal Free Energies= -3096.872084

Item	Value	Threshold	Converged?
Maximum Force	0.000096	0.000450	YES
RMS Force	0.000014	0.000300	YES

Table 3. Electronic transitions computed by TD-DFT for the closed-shell singlet state of **[PtCl$_2$(bpy)-(MV$^+$)$_2$]$^{2+}$**, for which part of the Gaussian output is shown. Relevant MO's are shown below:

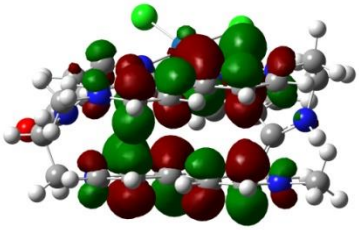

MO203 (LUMO+8)

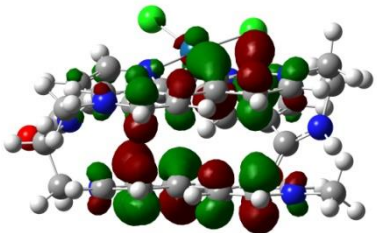

MO202(LUMO+7)

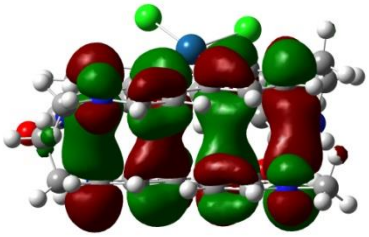

MO200 (LUMO+5)

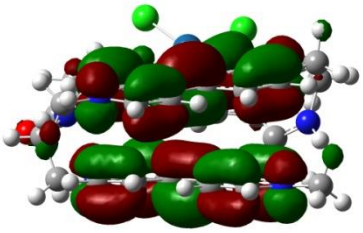

MO196 (LUMO+1)

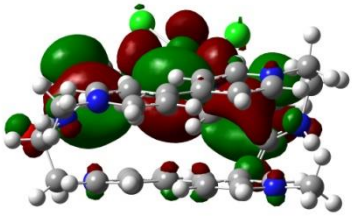

MO195 (LUMO)

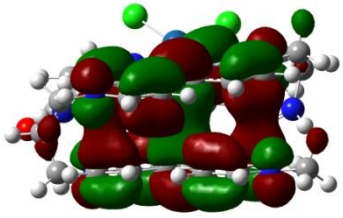

MO194 (HOMO)

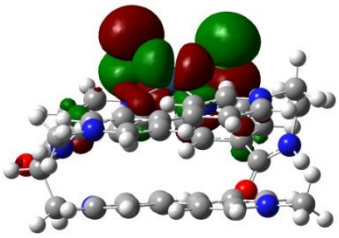

MO193 (HOMO-1)

Excitation energies and oscillator strengths (λ > 210 nm, f > 0.02 only):

Excited State 2: Singlet-A 1.4502 eV 854.92 nm f=0.1872 <S**2>=0.000

194 ->195 0.13260

194 ->196 0.72995

194 <-196 -0.22548

Excited State 7: Singlet-A 2.4345 eV 509.27 nm f=0.0812 <S**2>=0.000

194 ->200 0.56687

194 ->202 0.25317

194 ->203 -0.31311

Excited State 10: Singlet-A 2.8913 eV 428.82 nm f=0.2370 <S**2>=0.000

189 ->196 0.15735

193 ->195 0.24646

194 ->200 0.35302

194 ->202 -0.33652

194 ->203 0.38995

Excited State 14: Singlet-A 3.1946 eV 388.10 nm f=0.0470 <S**2>=0.000

192 ->195 0.27404

192 ->199 -0.23522

194 ->205 0.16930

194 ->206 0.14194

194 ->207 0.53957

Excited State 15: Singlet-A 3.1976 eV 387.75 nm f=0.0427 <S**2>=0.000

192 ->195 0.39556

192 ->198 0.12800

192 ->199 -0.37003

194 ->206 -0.10244

194 ->207 -0.36886

Excited State 17: Singlet-A 3.2522 eV 381.24 nm f=0.0991 <S**2>=0.000

190 ->199 0.21045

192 ->195 0.44169

192 ->198 -0.10408

192 ->199 0.44818

Excited State 20: Singlet-A 3.3043 eV 375.23 nm f=0.1525 <S**2>=0.000

192 ->195 -0.10441

194 ->201 0.11715

194 ->202 0.10759

194 ->205 0.62780

194 ->207 -0.16714

Excited State 25: Singlet-A 3.9412 eV 314.59 nm f=0.0302 <S**2>=0.000

185 ->195 0.11139

186 ->195 0.19199

187 ->195 0.39525

188 ->195 0.21718

189 ->196 0.33561

192 ->197 0.12963

193 ->198 0.24315

Excited State 26: Singlet-A 3.9546 eV 313.52 nm f=0.0637 <S**2>=0.000

188 ->195 0.60891

188 ->196 -0.12150

189 ->196 -0.25207

190 ->196 0.11914

Excited State 27: Singlet-A 3.9736 eV 312.02 nm f=0.4776 <S**2>=0.000

186 ->195 -0.13235

187 ->195 -0.22591

188 ->195 0.17568

189 ->195 0.15132

189 ->196 0.48473

192 ->197 -0.16174

193 ->198 -0.22791

194 ->200 -0.11578

Excited State 29: Singlet-A 4.0494 eV 306.18 nm f=0.0601 <S**2>=0.000

187 ->195 -0.11836

192 ->197 -0.35889

193 ->197 0.50389

193 ->198 0.20574

193 ->199 0.13360

Excited State 30: Singlet-A 4.0965 eV 302.66 nm f=0.0480 <S**2>=0.000

189 ->195 0.19166

191 ->197 -0.32121

192 ->197 0.28757

192 ->198 -0.13613

193 ->197 0.33331

193 ->198 -0.31736

Excited State 31: Singlet-A 4.1072 eV 301.87 nm f=0.0264 <S**2>=0.000

183 ->195 -0.13460

189 ->195 0.58461

189 ->196 -0.13342

192 ->197 -0.13296

193 ->197 -0.11032

193 ->198 0.20900

Excited State 36: Singlet-A 4.1796 eV 296.64 nm f=0.1873 <S**2>=0.000

185 ->196 -0.25707

186 ->195 0.14450

186 ->196 0.54293

187 ->196 -0.22079

194 ->209 0.14285

Excited State 37: Singlet-A 4.2056 eV 294.81 nm f=0.1564 <S**2>=0.000

181 ->195 0.17382

182 ->195 -0.16219

184 ->195 0.43959

184 ->197 -0.11246

187 ->195 -0.22495

192 ->197 0.19270

193 ->198 0.22864

Excited State 38: Singlet-A 4.2359 eV 292.70 nm f=0.1022 <S**2>=0.000

182 ->196 0.11883

185 ->195 0.15382

185 ->196 0.53940

187 ->195 -0.10857

187 ->196 -0.33732

Excited State 40: Singlet-A 4.2568 eV 291.26 nm f=0.0225 <S**2>=0.000

183 ->195 -0.16639

191 ->198 0.21499

192 ->198 0.56101

192 ->199 0.16712

193 ->197 0.14992

Excited State 41: Singlet-A 4.3157 eV 287.29 nm f=0.2479 <S**2>=0.000

181 ->195 0.13261

183 ->195 0.10941

184 ->195 0.34748

185 ->195 -0.12275

186 ->195 -0.15338

187 ->195 0.37315

187 ->196 -0.11302

192 ->197 -0.23052

192 ->198 0.10932

193 ->198 -0.17625

Excited State 43: Singlet-A 4.3381 eV 285.80 nm f=0.0228 <S**2>=0.000

185 ->195 -0.19773

186 ->195 -0.19731

190 ->197 0.59230

Excited State 44: Singlet-A 4.3454 eV 285.32 nm f=0.2207 <S**2>=0.000

183 ->195 0.14940

184 ->195 0.11182

185 ->195 0.33909

186 ->195 0.33139

190 ->197 0.32244

192 ->197 -0.20296

192 ->198 0.11105

193 ->198 -0.17303

Excited State 53: Singlet-A 4.5689 eV 271.37 nm f=0.0204 <S**2>=0.000

180 ->196 -0.22806

182 ->195 0.12242

182 ->196 0.54285

183 ->196 -0.13978

184 ->196 -0.10979

185 ->196 -0.14179

186 ->196 -0.12017

188 ->196 0.19163

Excited State 71: Singlet-A 5.1208 eV 242.12 nm f=0.0273 <S**2>=0.000

182 ->198 -0.10203

184 ->198 -0.10748

186 ->197 -0.10896

187 ->198 -0.28767

189 ->198 0.54854

189 ->199 0.10717

Excited State 73: Singlet-A 5.1443 eV 241.01 nm f=0.0449 <S**2>=0.000

171 ->195 0.11634

175 ->195 0.10039

176 ->195 -0.10811

177 ->199 -0.16046

183 ->197 -0.12701

183 ->198 0.25207

184 ->197 0.13654

185 ->198 0.17003

186 ->198 0.22471

187 ->198 0.28791

187 ->199 0.10989

189 ->198 0.25693

Excited State 79: Singlet-A 5.2095 eV 238.00 nm f=0.0520 <S**2>=0.000

175 ->195 -0.11632

176 ->195 0.51695

176 ->196 -0.10518

178 ->195 -0.13269

187 ->197 -0.13295

193 ->200 -0.28662

Excited State 81: Singlet-A 5.2547 eV 235.95 nm f=0.0264 <S**2>=0.000

175 ->195 0.61121

175 ->196 -0.12671

176 ->195 0.13361

187 ->198 -0.11328

Excited State 100: Singlet-A 5.4936 eV 225.69 nm f=0.0233 <S**2>=0.000

176 ->198 -0.10559

176 ->199 0.35573

184 ->197 -0.19889

184 ->198 0.27638

184 ->199 0.12284

185 ->198 0.12195

190 ->202 -0.28469

190 ->203 -0.20308

191 ->202 -0.10727

Excited State 122: Singlet-A 5.7474 eV 215.72 nm f=0.0262 <S**2>=0.000

170 ->195 0.17534

171 ->195 -0.17895

183 ->199 -0.22606

184 ->199 -0.12980

185 ->199 0.44845

186 ->199 -0.30688

Excited State 123: Singlet-A 5.7557 eV 215.41 nm f=0.0323 <S**2>=0.000

169 ->195 -0.11551

170 ->195 0.50766

170 ->196 -0.10625

171 ->195 -0.17786

177 ->197 0.13263

183 ->199 0.20068

185 ->199 -0.15670

193 ->204 0.16807

Excited State 127: Singlet-A 5.8140 eV 213.25 nm f=0.0502 <S**2>=0.000

169 ->195 -0.11762

170 ->195 0.27072

171 ->195 0.35159

174 ->195 -0.11681

177 ->197 -0.22213

181 ->197 0.14709

181 ->198 -0.18132

183 ->199 -0.14439

192 ->203 -0.12740

Excited State 128: Singlet-A 5.8304 eV 212.65 nm f=0.0267 <S**2>=0.000

177 ->197 0.10133

185 ->201 -0.10137

186 ->201 0.29988

187 ->201 -0.15365

189 ->202 0.22556

189 ->203 -0.27059

192 ->202 0.12745

192 ->203 -0.17889

192 ->206 -0.14323

194 ->220 0.11467

194 ->222 -0.14318

Excited State 129: Singlet-A 5.8325 eV 212.58 nm f=0.0646 <S**2>=0.000

169 ->195 0.13767

177 ->197 0.29226

181 ->197 -0.11582

181 ->198 0.11556

186 ->201 -0.15764

189 ->202 -0.12256

189 ->203 0.14726

192 ->202 0.20115

192 ->203 -0.27739

192 ->206 -0.22415

193 ->208 0.13232

Excited State 132: Singlet-A 5.8491 eV 211.97 nm f=0.0516 <S**2>=0.000

169 ->195 0.17319

171 ->195 0.16331

174 ->195 -0.10835

177 ->197 0.29027

179 ->197 0.18366

180 ->197 0.29529

192 ->202 -0.12612

192 ->203 0.17836

192 ->206 0.17316

193 ->208 -0.21806

Table 4. Electronic transitions computed by TD-DFT for the open-shell singlet state of **[PtCl$_2$(bpy)-(MV$^+$)$_2$]$^{2+}$**, for which part of the Gaussian output is shown.

Relevant MO's (only α orbitals) are shown below:

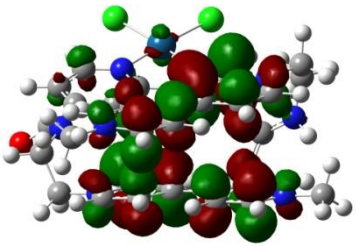

MO203α (LUMO+8)

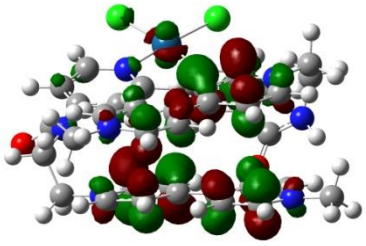

MO202α(LUMO+7)

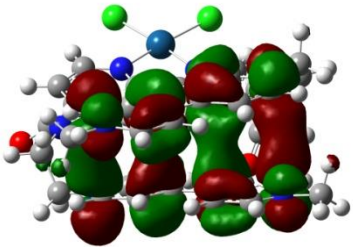

MO200α (LUMO+5)

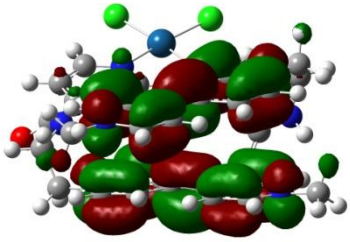

MO196α (LUMO+1)

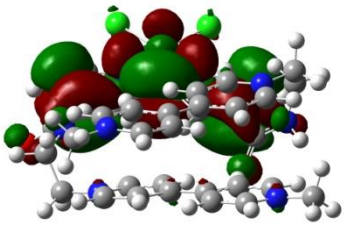

MO195α (LUMO)

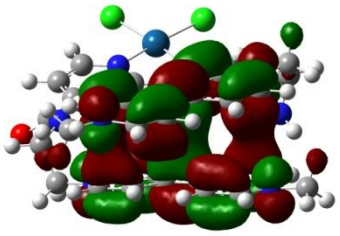

MO194α (HOMO)

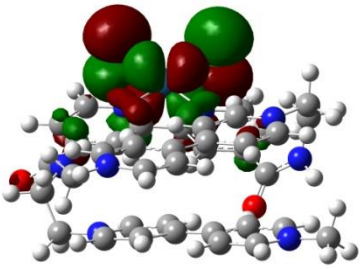

MO193α (HOMO-1)

Excitation energies and oscillator strengths (λ > 210 nm, f > 0.02 only):

Excited State 4: 1.000-A 1.4570 eV 850.94 nm f=0.1882 <S**2>=0.000

194A ->195A 0.10123

194A ->196A 0.73438

194B ->195B 0.10123

194B ->196B 0.73438

194A <-196A -0.22590

194B <-196B -0.22590

Excited State 16: 1.000-A 2.4340 eV 509.38 nm f=0.0832 <S**2>=0.000

194A ->200A 0.56867

194A ->202A 0.23914

194A ->203A -0.31837

194B ->200B 0.56867

194B ->202B 0.23914

194B ->203B -0.31836

Excited State 26: 1.000-A 2.8942 eV 428.40 nm f=0.2422 <S**2>=0.000

189A ->196A 0.16276

193A ->195A 0.20679

194A ->200A 0.35625

194A ->202A -0.33168

194A ->203A 0.41449

189B ->196B 0.16276

193B ->195B 0.20679

194B ->200B 0.35625

194B ->202B -0.33168

194B ->203B 0.41449

Excited State 34: 1.000-A 3.1891 eV 388.78 nm f=0.0749 <S**2>=0.000

192A ->195A 0.46399

192A ->198A 0.19114

192A ->199A -0.45986

192B ->195B 0.46399

192B ->198B 0.19113

192B ->199B -0.45986

Excited State 38: 1.000-A 3.2590 eV 380.43 nm f=0.1149 <S**2>=0.000

190A ->199A 0.10266

192A ->195A 0.47571

192A ->198A -0.13260

192A ->199A 0.44705

194A ->205A 0.10474

190B ->199B 0.10266

192B ->195B 0.47571

192B ->198B -0.13260

192B ->199B 0.44705

194B ->205B 0.10474

Excited State 42: 1.000-A 3.3099 eV 374.58 nm f=0.1555 <S**2>=0.000

194A ->201A 0.11732

194A ->202A 0.12050

194A ->205A 0.62929

194A ->207A -0.17246

194B ->201B 0.11732

194B ->202B 0.12050

194B ->205B 0.62929

194B ->207B -0.17246

Excited State 57: 1.000-A 3.9398 eV 314.70 nm f=0.0427 <S**2>=0.000

185A ->195A 0.12225

186A ->195A 0.17620

187A ->195A 0.43183

189A ->196A 0.37682

192A ->197A 0.12765

193A ->198A 0.23525

185B ->195B 0.12225

186B ->195B 0.17620

187B ->195B 0.43183

189B ->196B 0.37682

192B ->197B 0.12765

193B ->198B 0.23525

Excited State 61: 1.000-A 3.9713 eV 312.20 nm f=0.5187 <S**2>=0.000

186A ->195A -0.11337

187A ->195A -0.22005

188A ->195A 0.12769

189A ->195A 0.13083

189A ->196A 0.51905

192A ->197A -0.17479

193A ->198A -0.21082

194A ->200A -0.12189

186B ->195B -0.11337

187B ->195B -0.22005

188B ->195B 0.12768

189B ->195B 0.13083

189B ->196B 0.51905

192B ->197B -0.17479

193B ->198B -0.21082

194B ->200B -0.12189

Excited State 66: 1.000-A 4.0491 eV 306.20 nm f=0.0604 <S**2>=0.000

187A ->195A -0.10239

192A ->197A -0.36473

193A ->197A 0.50210

193A ->198A 0.24066

187B ->195B -0.10239

192B ->197B -0.36473

193B ->197B 0.50209

193B ->198B 0.24067

Excited State 70: 1.000-A 4.1022 eV 302.24 nm f=0.0780 <S**2>=0.000

189A ->195A 0.29452

192A ->197A -0.30587

192A ->198A 0.10104

193A ->197A -0.34928

193A ->198A 0.35788

193A ->199A 0.12768

189B ->195B 0.29451

192B ->197B -0.30587

192B ->198B 0.10104

193B ->197B -0.34928

193B ->198B 0.35788

193B ->199B 0.12768

Excited State 81: 1.000-A 4.1827 eV 296.42 nm f=0.1763 <S**2>=0.000

185A ->196A -0.25170

186A ->195A 0.11907

186A ->196A 0.56520

187A ->196A -0.18336

194A ->209A 0.13646

185B ->196B -0.25170

186B ->195B 0.11907

186B ->196B 0.56521

187B ->196B -0.18336

194B ->209B 0.13645

Excited State 82: 1.000-A 4.2030 eV 294.99 nm f=0.1613 <S**2>=0.000

181A ->195A	0.16866
182A ->195A	-0.15878
184A ->195A	0.43280
184A ->197A	-0.11176
187A ->195A	-0.23141
192A ->197A	0.18850
193A ->198A	0.23557
181B ->195B	0.16864
182B ->195B	-0.15879
184B ->195B	0.43281
184B ->197B	-0.11177
187B ->195B	-0.23140
192B ->197B	0.18847
193B ->198B	0.23560

Excited State 86: 1.000-A 4.2392 eV 292.47 nm f=0.1136 <S**2>=0.000

182A ->196A	0.12078
185A ->195A	0.12587
185A ->196A	0.54163
186A ->196A	0.10774
187A ->196A	-0.34258
182B ->196B	0.12078
185B ->195B	0.12587

185B ->196B 0.54163

186B ->196B 0.10774

187B ->196B -0.34258

Excited State 92: 1.000-A 4.3136 eV 287.43 nm f=0.2432 <S**2>=0.000

181A ->195A 0.13371

183A ->195A 0.10541

184A ->195A 0.35673

185A ->195A -0.13865

186A ->195A -0.18171

187A ->195A 0.36730

192A ->197A -0.22852

193A ->198A -0.17665

181B ->195B 0.13373

183B ->195B 0.10541

184B ->195B 0.35673

185B ->195B -0.13866

186B ->195B -0.18171

187B ->195B 0.36730

192B ->197B -0.22853

193B ->198B -0.17665

Excited State 98: 1.000-A 4.3439 eV 285.42 nm f=0.2447 <S**2>=0.000

183A ->195A 0.16575

184A ->195A 0.11306

185A ->195A 0.40574

186A ->195A 0.36537

190A ->197A 0.11518

192A ->197A -0.21713

192A ->198A 0.10888

193A ->198A -0.18509

183B ->195B 0.16575

184B ->195B 0.11306

185B ->195B 0.40574

186B ->195B 0.36537

190B ->197B 0.11518

192B ->197B -0.21713

192B ->198B 0.10888

193B ->198B -0.18509

Excited State 151: 1.000-A 5.0139 eV 247.28 nm f=0.0221 <S**2>=0.000

176A ->195A 0.12587

177A ->195A 0.10666

183A ->197A 0.23762

183A ->198A -0.21955

187A ->197A 0.27209

187A ->199A 0.11522

188A ->197A 0.14348

188A ->198A 0.11823

189A ->197A 0.35057

189A ->198A 0.13195

176B ->195B 0.12587

177B ->195B 0.10668

183B ->197B 0.23762

183B ->198B -0.21956

187B ->197B 0.27209

187B ->199B 0.11522

188B ->197B 0.14347

188B ->198B 0.11823

189B ->197B 0.35066

189B ->198B 0.13198

Excited State 156: 1.000-A 5.1131 eV 242.48 nm f=0.0226 <S**2>=0.000

186A ->197A -0.10800

187A ->198A -0.25571

187A ->199A -0.10053

189A ->198A 0.55504

189A ->199A 0.13823

186B ->197B -0.10800

187B ->198B -0.25571

187B ->199B -0.10053

189B ->198B 0.55503

189B ->199B 0.13822

Excited State 160: 1.000-A 5.1409 eV 241.17 nm f=0.0416 <S**2>=0.000

171A ->195A 0.11191

176A ->195A -0.10437

177A ->199A -0.23483

183A ->197A -0.14426

183A ->198A 0.24146

184A ->197A 0.12328

185A ->198A 0.14987

186A ->198A 0.17448

187A ->198A 0.29508

187A ->199A 0.10841

189A ->198A 0.23177

171B ->195B 0.11191

176B ->195B -0.10437

177B ->199B -0.23483

183B ->197B -0.14426

183B ->198B 0.24146

184B ->197B 0.12329

185B ->198B 0.14987

186B ->198B 0.17447

187B ->198B 0.29508

187B ->199B 0.10841

189B ->198B 0.23174

Excited State 171: 1.000-A 5.1990 eV 238.48 nm f=0.0458 <S**2>=0.000

176A ->195A 0.49232

178A ->195A -0.16545

187A ->197A -0.11876

193A ->200A 0.36966

176B ->195B 0.49231

178B ->195B -0.16546

187B ->197B -0.11876

193B ->200B 0.36959

Excited State 173: 1.000-A 5.2064 eV 238.14 nm f=0.0213 <S**2>=0.000

176A ->195A -0.30573

187A ->197A 0.13148

193A ->200A 0.57916

176B ->195B -0.30572

187B ->197B 0.13148

193B ->200B 0.57930

Excited State 174: 1.000-A 5.2231 eV 237.38 nm f=0.0224 <S**2>=0.000

182A ->198A 0.17612

184A ->198A 0.13136

185A ->197A 0.31536

185A ->198A -0.20467

186A ->197A 0.25815

186A ->198A -0.18244

187A ->197A -0.21033

187A ->198A 0.14409

189A ->198A 0.24539

182B ->198B 0.17612

184B ->198B 0.13136

185B ->197B 0.31537

185B ->198B -0.20467

186B ->197B 0.25816

186B ->198B -0.18244

187B ->197B -0.21033

187B ->198B 0.14409

189B ->198B 0.24539

Excited State 215: 1.000-A 5.4947 eV 225.64 nm f=0.0347 <S**2>=0.000

176A ->199A -0.12304

184A ->198A -0.10709

190A ->202A 0.42757

190A ->203A 0.28499

191A ->202A 0.33816

191A ->203A 0.21486

176B ->199B -0.12304

184B ->198B -0.10709

190B ->202B 0.42757

190B ->203B 0.28499

191B ->202B 0.33815

191B ->203B 0.21486

Excited State 255: 1.000-A 5.7077 eV 217.22 nm f=0.0219 <S**2>=0.000

171A ->195A 0.12321

183A ->198A -0.14586

183A ->199A 0.50709

184A ->199A -0.12237

185A ->199A 0.22688

186A ->199A -0.28658

171B ->195B 0.12321

183B ->198B -0.14586

183B ->199B 0.50709

184B ->199B -0.12237

185B ->199B 0.22688

186B ->199B -0.28658

Excited State 263: 1.000-A 5.7488 eV 215.67 nm f=0.0254 <S**2>=0.000

169A ->195A -0.11964

170A ->195A 0.61061

170A ->196A -0.10015

177A ->197A 0.10168

183A ->199A 0.10702

169B ->195B -0.11963

170B ->195B 0.61059

170B ->196B -0.10015

177B ->197B 0.10167

183B ->199B 0.10703

Excited State 269: 1.000-A 5.8005 eV 213.75 nm f=0.0439 <S**2>=0.000

169A ->195A -0.10289

170A ->195A 0.12550

171A ->195A 0.40948

174A ->195A -0.13589

174A ->196A 0.10925

177A ->197A -0.22936

181A ->198A 0.19696

183A ->199A -0.16531

186A ->200A -0.12016

187A ->198A -0.11608

169B ->195B -0.10289

170B ->195B 0.12550

171B ->195B 0.40948

174B ->195B -0.13589

174B ->196B 0.10925

177B ->197B -0.22936

181B ->198B 0.19695

183B ->199B -0.16531

186B ->200B -0.12016

187B ->198B -0.11608

Excited State 270: 1.000-A 5.8085 eV 213.45 nm f=0.0342 <S**2>=0.000

171A ->195A -0.13321

177A ->197A 0.15739

177A ->198A -0.10177

180A ->198A -0.11093

181A ->197A -0.30973

181A ->198A 0.42219

181A ->199A 0.13669

192A ->202A -0.12035

192A ->203A 0.17897

171B ->195B -0.13321

177B ->197B 0.15740

177B ->198B -0.10176

180B ->198B -0.11094

181B ->197B -0.30974

181B ->198B 0.42222

181B ->199B 0.13669

192B ->202B -0.12035

192B ->203B 0.17897

Excited State 273: 1.000-A 5.8302 eV 212.66 nm f=0.0955 <S**2>=0.000

169A ->195A 0.18624

171A ->195A 0.18618

177A ->197A 0.36444

180A ->197A 0.13712

186A ->201A -0.14046

189A ->203A 0.12336

192A ->202A 0.14806

192A ->203A -0.21813

192A ->206A -0.14414

193A ->208A 0.10326

169B ->195B 0.18624

171B ->195B 0.18618

177B ->197B 0.36444

180B ->197B 0.13712

186B ->201B -0.14046

189B ->203B 0.12336

192B ->202B 0.14805

192B ->203B -0.21812

192B ->206B -0.14414

193B ->208B 0.10326

Excited State 274: 1.000-A 5.8305 eV 212.65 nm f=0.0269 <S**2>=0.000

177A ->197A 0.11743

185A ->201A -0.10834

186A ->200A 0.10043

186A ->201A 0.33479

187A ->201A -0.14298

189A ->202A 0.21829

189A ->203A -0.28204

192A ->203A -0.14360

194A ->220A 0.11901

194A ->222A	-0.14291
177B ->197B	0.11743
185B ->201B	-0.10834
186B ->200B	0.10043
186B ->201B	0.33479
187B ->201B	-0.14298
189B ->202B	0.21829
189B ->203B	-0.28204
192B ->203B	-0.14360
194B ->220B	0.11902
194B ->222B	-0.14291

Tables for the results of DFT calculations in Chapter 3

Table 5. Geometry optimized by DFT for the closed-shell singlet state of **[Ru_Im]$^{3+}$**. Optimized at the B3LYP level of DFT using the LanL2DZ basis set with solvation in DMF taken into consideration (PCM).[a]

Atom	X	Y	Z
C	1.88960604	2.62694401	-3.15739506
C	1.14130524	3.81672267	-3.09443479
C	0.17277284	3.96082132	-2.08707932
C	-0.03124473	2.92065100	-1.16544103
C	1.64683766	1.62048273	-2.21078093
C	-1.01842005	2.97859851	-0.06553876
C	-1.86808984	4.05254244	0.25215919
C	-2.72449210	3.93484537	1.36364116
H	-3.38566308	4.75469802	1.62350724
C	-2.71852064	2.76550611	2.14824310
C	-1.85359267	1.71510146	1.79409675
H	2.64698138	2.47511622	-3.91843649
H	1.30778416	4.61448393	-3.81080697
H	2.20592770	0.69287653	-2.22228501
H	-3.36638017	2.68782882	3.01313227
N	0.71268141	1.75405640	-1.23443367
N	-1.04838397	1.84459344	0.69711894
H	-0.41172908	4.87111092	-2.02064050
H	-1.86484711	4.96033623	-0.33939669
C	-1.68127581	0.42700786	2.50058996
C	-2.40891133	0.06096054	3.64496708
C	-0.49949740	-1.62233051	2.55670737
C	-2.16823415	-1.18190484	4.25403859
H	-3.15075402	0.73404301	4.05895612
C	-1.19794757	-2.03724309	3.70055140

H	0.25828167	-2.24980975	2.10405942
H	-2.72382198	-1.47324327	5.13936086
H	-0.98023293	-3.00432353	4.14000871
N	-0.72698262	-0.42229550	1.96367674
Ru	0.23339492	0.37751412	0.27550889
N	1.51575772	-1.21083301	-0.21521452
C	0.99489019	-2.14403607	-1.08708149
C	2.77513901	-1.37999806	0.26756717
C	1.74931838	-3.26232252	-1.48034584
C	-0.37686613	-1.86256842	-1.54066749
C	3.57830157	-2.47594593	-0.09053299
H	3.11242349	-0.60841767	0.95136249
C	3.04860435	-3.43084393	-0.98053661
H	1.33737981	-3.99401779	-2.16405027
C	-1.09085713	-2.66747941	-2.44427860
N	-0.94612112	-0.71787668	-1.01742328
H	3.63699563	-4.29250973	-1.28070749
C	-2.39350875	-2.31020816	-2.81814234
H	-0.63992089	-3.56195557	-2.85564375
C	-2.20881477	-0.37605297	-1.38643342
H	-2.94642668	-2.92839303	-3.51847097
C	-2.97233180	-1.14428185	-2.28024438
H	-2.60430507	0.53535984	-0.95501719
Cl	1.89955160	1.51665032	1.80010195
C	-4.37153639	-0.70702442	-2.68057805
H	-4.36733162	0.31746126	-3.06196810
H	-4.75761097	-1.35576406	-3.47131604
C	4.96639006	-2.64680262	0.50468623
H	4.91228206	-2.73976773	1.59350030
H	5.43570378	-3.55440024	0.11545783
N	-5.33791294	-0.73049099	-1.54591233
N	-6.58698524	-1.45443449	0.10946532
N	5.86719459	-1.50073053	0.20977929
N	7.25882915	0.17548338	0.49286763
C	8.11547499	1.19620520	1.13411489
H	7.83337727	2.18663339	0.76968486
H	7.97705355	1.15674753	2.21564974
H	9.16270258	0.99788317	0.89304399

C	-7.19485723	-2.33721009	1.12795303
H	-7.00665810	-1.92737980	2.12310186
H	-8.27133378	-2.40542169	0.95432960
H	-6.75213141	-3.33169550	1.05548205
C	7.10992683	-0.00730396	-0.88674469
C	6.23892182	-1.05738988	-1.06469980
C	-6.12282816	0.34787621	-1.12184593
C	-6.90436433	-0.10578539	-0.08352645
C	-5.63973384	-1.81183483	-0.78551002
C	6.49950547	-0.73910890	1.13549767
H	6.41273278	-0.84586911	2.20363623
H	7.62172447	0.60624807	-1.60878204
H	5.86746167	-1.50967506	-1.96830090
H	-6.06482944	1.32156330	-1.57841579
H	-7.63747749	0.40592636	0.51659466
H	-5.20206850	-2.79119133	-0.87807683

[a]Part of the Gaussian output file:

SCF Done: E(RB3LYP) = -1954.65219947 a.u. after 1 cycles

	1	2	3
	A	A	A
Frequencies --	6.7091	20.2934	21.9455
Red. masses --	4.9865	5.1613	5.5454

Zero-point correction= 0.642299 (Hartree/Particle)
Thermal correction to Energy= 0.681026
Thermal correction to Enthalpy= 0.681971
Thermal correction to Gibbs Free Energy= 0.567437
Sum of electronic and zero-point Energies= -1954.009901
Sum of electronic and thermal Energies= -1953.971173
Sum of electronic and thermal Enthalpies= -1953.970229
Sum of electronic and thermal Free Energies= -1954.084763

Item	Value	Threshold	Converged?
Maximum Force	0.000004	0.000450	YES
RMS Force	0.000001	0.000300	YES

Table 6. Geometry optimized by DFT for the closed-shell singlet state of **[Ru_Me]**$^{+}$. Optimized at the B3LYP level of DFT using the LanL2DZ basis set with solvation in DMF taken into consideration (PCM).[a]

Atom	X	Y	Z
C	0.18054810	-4.42198307	-0.44916798
C	-1.18754627	-4.74250163	-0.52890329
C	-2.12992432	-3.70207294	-0.58526522
C	-1.69347985	-2.36686988	-0.56136711
C	0.56200645	-3.07219764	-0.42745034
C	-2.60266605	-1.20173212	-0.61984834
C	-4.00258080	-1.22521686	-0.74717005
C	-4.70034209	-0.00338586	-0.80677125
H	-5.78068168	-0.00407553	-0.90589357
C	-4.00386381	1.21930495	-0.74994012
C	-2.60393036	1.19754195	-0.62253638
H	0.94038271	-5.19442730	-0.40499719
H	-1.51389210	-5.77723927	-0.54730650
H	1.60403464	-2.78161839	-0.36987519
H	-4.54387683	2.15680867	-0.81160847
N	-0.34396009	-2.06217296	-0.48196023
N	-1.95051186	-0.00167065	-0.54963732
H	-3.18818170	-3.92864449	-0.64632775
H	-4.54165286	-2.16340364	-0.80667751
C	-1.69599711	2.36377998	-0.56650077
C	-2.13393283	3.69844993	-0.59319400
C	0.55869894	3.07185545	-0.43396681
C	-1.19270237	4.74002088	-0.53896933
H	-3.19244665	3.92369255	-0.65471736
C	0.17575151	4.42116045	-0.45850833
H	1.60103119	2.78250574	-0.37573166
H	-1.52015958	5.77436584	-0.55954116
H	0.93472863	5.19453532	-0.41589535
N	-0.34617304	2.06072368	-0.48642127

Ru	0.03719969	-0.00048327	-0.46568623
N	2.13347850	0.00074912	-0.27541178
C	2.60317369	0.00210603	1.01772811
C	3.02058023	-0.00016349	-1.30966335
C	3.98730642	0.00209989	1.27676202
C	1.55923178	0.00333974	2.05476714
C	4.41412238	0.00000737	-1.12343123
H	2.57796895	-0.00110597	-2.29941501
C	4.89207596	0.00104570	0.20822199
H	4.35596291	0.00277418	2.29563918
C	1.81378414	0.00571997	3.43966626
N	0.26367237	0.00212009	1.58803467
H	5.96084732	0.00101173	0.40309995
C	0.74813777	0.00657889	4.34644713
H	2.83328989	0.00695785	3.80602929
C	-0.76814677	0.00291578	2.47797945
H	0.94437608	0.00838779	5.41479212
C	-0.58367286	0.00508510	3.87008147
H	-1.76629571	0.00175917	2.05768403
Cl	0.05435339	-0.00307923	-3.00276876
C	-1.76710088	0.00579691	4.81138361
H	-1.74821767	-0.87648830	5.46372155
H	-1.74897306	0.88975955	5.46146344
C	5.35542632	-0.00092684	-2.30710363
H	4.80763374	-0.00242785	-3.25478669
H	6.00641726	0.88262031	-2.29095562
H	6.00750790	-0.88361675	-2.28874493
H	-2.71588254	0.00468304	4.26540085

[a]Part of the Gaussian output file:

SCF Done: E(RB3LYP) = -1425.19309875 a.u. after 1 cycles

	1	2	3
	A	A	A
Frequencies --	21.0233	39.4597	39.5289
Red. masses --	5.1002	5.1091	5.1975

Zero-point correction= 0.451727 (Hartree/Particle)

Thermal correction to Energy=	0.480308
Thermal correction to Enthalpy=	0.481252
Thermal correction to Gibbs Free Energy=	0.392048
Sum of electronic and zero-point Energies=	-1424.741371
Sum of electronic and thermal Energies=	-1424.712791
Sum of electronic and thermal Enthalpies=	-1424.711847
Sum of electronic and thermal Free Energies=	-1424.801051

Item	Value	Threshold	Converged?
Maximum Force	0.000008	0.000450	YES
RMS Force	0.000001	0.000300	YES

Table 7. Geometry optimized by DFT for the doublet state of singly-reduced **[Ru_Im]$^{3+}$**. Optimized at the UB3LYP level of DFT using the LanL2DZ basis set with solvation in DMF taken into consideration (PCM).[a]

Atom	X	Y	Z
C	2.08693902	1.87256629	-3.52096736
C	1.44128720	3.09915682	-3.77041417
C	0.50048044	3.57526563	-2.84269324
C	0.21961974	2.82462059	-1.68770694
C	1.77093904	1.16353536	-2.35289841
C	-0.74894112	3.23841584	-0.65022970
C	-1.50551162	4.42318672	-0.61764831
C	-2.36646040	4.65184645	0.47364190
H	-2.95608031	5.56181095	0.51367498
C	-2.45975250	3.71063846	1.51783982
C	-1.68680087	2.53817096	1.44694851
H	2.81918790	1.46944242	-4.21215441
H	1.66503638	3.67111307	-4.66516536
H	2.24493383	0.21795232	-2.11786507
H	-3.11513823	3.89599394	2.36092660
N	0.86232845	1.61817477	-1.45052018

N	-0.86780489	2.33080856	0.36880671
H	-0.00680874	4.51756369	-3.01661993
H	-1.42830109	5.15610795	-1.41257923
C	-1.63333228	1.44171497	2.43746060
C	-2.39619911	1.41283462	3.61784792
C	-0.64972759	-0.64165882	2.98544082
C	-2.27543736	0.32485314	4.49804692
H	-3.07430434	2.22672889	3.84884198
C	-1.38816152	-0.72034388	4.17522177
H	0.04819415	-1.41887974	2.69735882
H	-2.85890927	0.29387644	5.41258101
H	-1.26595126	-1.57859426	4.82708069
N	-0.75902232	0.40922605	2.13097194
Ru	0.27065889	0.70703686	0.33586434
N	1.41350103	-1.06677144	0.24949108
C	0.78740944	-2.11594546	-0.45223428
C	2.64163150	-1.26253493	0.78763133
C	1.47301220	-3.36683551	-0.59099257
C	-0.51545946	-1.83033200	-0.95776651
C	3.35495021	-2.46692972	0.67454441
H	3.05072773	-0.40992329	1.32245355
C	2.73478996	-3.54032260	-0.04030785
H	0.99904447	-4.18414921	-1.12352828
C	-1.32974104	-2.74693993	-1.70155993
N	-1.02203294	-0.53857369	-0.68747598
H	3.24623583	-4.49499778	-0.14155791
C	-2.59483996	-2.38588590	-2.13141327
H	-0.94302241	-3.73407324	-1.93119215
C	-2.26837374	-0.20837648	-1.11126825
H	-3.20121493	-3.08749627	-2.69908333
C	-3.10195940	-1.07600004	-1.82630623
H	-2.60537301	0.79521933	-0.87056528
Cl	2.06834499	2.02176043	1.59706702
C	-4.46597815	-0.62900575	-2.27573561
H	-4.59512769	0.44842559	-2.13051791
H	-4.64129929	-0.85502461	-3.33297858
C	4.72249276	-2.61209854	1.29556710
H	4.77738360	-2.13419636	2.27802852

H	4.98348329	-3.66795325	1.41792817
N	-5.58522392	-1.31485516	-1.53118418
N	-6.74516521	-2.27783185	0.06788539
N	5.81506767	-1.98675276	0.47060124
N	7.51326424	-0.72041977	-0.11834527
C	8.59615738	0.28381376	-0.06971614
H	8.40386992	1.06709257	-0.80702293
H	8.63264039	0.72586083	0.92726717
H	9.55204639	-0.19942695	-0.28573156
C	-7.10242092	-2.89353756	1.36292411
H	-7.92942961	-2.34068611	1.81501232
H	-7.39758716	-3.93370482	1.20493660
H	-6.23818975	-2.85950384	2.02864038
C	7.18749135	-1.51243628	-1.22465677
C	6.12297887	-2.30441128	-0.85557886
C	-6.87430812	-1.52610557	-2.02902213
C	-7.60231943	-2.13023847	-1.02768856
C	-5.53098765	-1.77654674	-0.26094393
C	6.66813108	-1.02606164	0.89466860
H	6.67380730	-0.57518044	1.87267854
H	7.72436443	-1.45096592	-2.15626350
H	5.57711407	-3.04318179	-1.41681498
H	-7.16322402	-1.24135911	-3.02670586
H	-8.62712012	-2.46120574	-1.00928197
H	-4.66581742	-1.75570214	0.37822481

[a]Part of the Gaussian output file:

SCF Done: E(UB3LYP) = -1954.77181259 a.u. after 1 cycles

	1	2	3
	A	A	A
Frequencies --	10.0147	16.6793	19.6853
Red. masses --	5.3921	5.8436	5.1289

Zero-point correction= 0.637536 (Hartree/Particle)
Thermal correction to Energy= 0.677063

Thermal correction to Enthalpy=	0.678007
Thermal correction to Gibbs Free Energy=	0.559795
Sum of electronic and zero-point Energies=	-1954.134277
Sum of electronic and thermal Energies=	-1954.094749
Sum of electronic and thermal Enthalpies=	-1954.093805
Sum of electronic and thermal Free Energies=	-1954.212017

Item	Value	Threshold	Converged?
Maximum Force	0.000003	0.000450	YES
RMS Force	0.000001	0.000300	YES

Table 8. Geometry optimized by DFT for the doublet state of singly-reduced **[Ru_Me]**$^{+}$. Optimized at the UB3LYP level of DFT using the LanL2DZ basis set with solvation in DMF taken into consideration (PCM).[a]

Atom	X	Y	Z
C	0.26189699	-4.38579652	-0.71762853
C	-1.12494770	-4.72262868	-0.80305979
C	-2.07313113	-3.70398229	-0.79702452
C	-1.67176913	-2.33876452	-0.70860100
C	0.61663601	-3.03862377	-0.63059484
C	-2.57408643	-1.21365744	-0.70087545
C	-3.98593509	-1.22285415	-0.81714405
C	-4.69633293	-0.01273301	-0.81408244
H	-5.77836102	-0.02125453	-0.90610205
C	-4.00864639	1.23212057	-0.70308771
C	-2.61495715	1.21798597	-0.58674379
H	1.03192854	-5.15015713	-0.71993716
H	-1.43537002	-5.76159521	-0.87154710
H	1.65813746	-2.73943419	-0.56544865
H	-4.56283169	2.16431890	-0.71629964
N	-0.29333343	-2.02249934	-0.62604955
N	-1.93492694	0.02246964	-0.57238525

H	-3.13064733	-3.94310444	-0.85912973
H	-4.52078728	-2.16255583	-0.91755588
C	-1.72355886	2.38449391	-0.46947284
C	-2.16684629	3.72269818	-0.42956827
C	0.52931192	3.11359368	-0.27947634
C	-1.24045269	4.76768253	-0.31401442
H	-3.22825994	3.93858279	-0.48891898
C	0.13755160	4.45518344	-0.23685713
H	1.57458091	2.83032125	-0.22753796
H	-1.57688711	5.79945953	-0.28475302
H	0.88908589	5.23258441	-0.14767472
N	-0.36286635	2.08822584	-0.39457849
Ru	0.06203004	0.03508106	-0.47382951
N	2.14610324	0.03677579	-0.22500277
C	2.57590165	-0.05627095	1.08130875
C	3.07276519	0.11495466	-1.22420759
C	3.95178940	-0.07272130	1.38618967
C	1.49835355	-0.12772402	2.07775470
C	4.45797531	0.10411332	-0.99126798
H	2.66193778	0.18460350	-2.22567609
C	4.89289608	0.00690531	0.35320157
H	4.28482579	-0.14624672	2.41515319
C	1.70335110	-0.22034021	3.46871870
N	0.21830659	-0.09315931	1.56316168
H	5.95483005	-0.00630830	0.58309016
C	0.60727397	-0.27771733	4.33611268
H	2.71038529	-0.24674599	3.86825183
C	-0.84448284	-0.15017315	2.41817372
H	0.76472448	-0.34885621	5.40872288
C	-0.70734501	-0.24253437	3.81159159
H	-1.82433494	-0.12082500	1.95788913
Cl	0.15616151	0.21851491	-3.05246485
C	-1.92346665	-0.30284088	4.70955890
H	-1.92950488	-1.22794439	5.30034447
H	-1.92872491	0.53455035	5.41920800
C	5.43956286	0.19146731	-2.13942835
H	4.92344105	0.25443779	-3.10297938
H	6.08375795	1.07486718	-2.04004169

H	6.09716889	-0.68726863	-2.16225404
H	-2.85198809	-0.26345524	4.13072643

[a]Part of the Gaussian output file:

SCF Done: E(UB3LYP) = -1425.29842979 a.u. after 1 cycles

	1	2	3
	A	A	A
Frequencies --	24.9720	32.7084	39.2632
Red. masses --	4.9528	5.0614	5.1271

Zero-point correction=	0.446325 (Hartree/Particle)
Thermal correction to Energy=	0.475405
Thermal correction to Enthalpy=	0.476349
Thermal correction to Gibbs Free Energy=	0.385648
Sum of electronic and zero-point Energies=	-1424.852105
Sum of electronic and thermal Energies=	-1424.823024
Sum of electronic and thermal Enthalpies=	-1424.822080
Sum of electronic and thermal Free Energies=	-1424.912782

Item	Value	Threshold	Converged?
Maximum Force	0.000028	0.000450	YES
RMS Force	0.000003	0.000300	YES

Acknowledgements

This doctoral thesis is the summary of the author's studies from April 2013 to March 2019 at the Department of Chemistry, Faculty of Science, Kyushu University under the direction of Professor Ken Sakai.

The author expresses his deepest gratitude to Professor Dr. Ken Sakai for his significant guidance, continuous encouragement, and valuable discussion. The author could learn much from him not only chemistry but also attitude toward research. The author really appreciates Associate Professor Dr. Hironobu Ozawa for his instructive direction. The author is also deeply grateful to Assistant Professor Dr. Kosei Yamauchi for his valuable suggestion and discussion about research. The author appreciates Assistant Professor Dr. Alexander Rene Parent in University of North Dakota in USA for his valuable suggestion. The author is equally grateful to Dr. Kyoji Kitamoto for his kindness and valuable discussion. The author appreciates Dr. Arnau Call and Dr. Mihaela Cibian for their encouragement and valuable advises.

The author is grateful to Associate Professor Dr. Motonori Watanabe in Kyushu University for the measurement of ESI-TOF-MS.

Acknowledge is made to all members of Sakai Laboratory for their valuable suggestion, heartfelt encouragement and friendship during his time in the Lab.

The author deeply appreciates 'International Institute for Carbon Neutral Energy' for the financial support as a research assistant.

Finally, the author wishes to offer thank for his family for their continuous, warmhearted encouragement and financial support.

Keiya Yamamoto

March 2019

List of Publications

Chapter 1.

"Pt(II)-Catalyzed Photosynthesis for H_2 Evolution Cycling Between Singly and Triply Reduced Species"
Keiya Yamamoto, Kyoji Kitamoto, Kosei Yamauchi and Ken Sakai
Chem. Commun., **2015**, *51*, 14516-14519.

Chapter 2.

"Photocatalytic H_2 Evolution Using a Ru Chromophore Tethered to Six Viologen Acceptors"
Keiya Yamamoto, Arnau Call and Ken Sakai
Chem. Eur. J., **2018**, *24*, 16620-16629 (*Selected as a Very Important Paper*).

Chapter 3.

"CO_2 Reduction Catalyzed by a Ru Complex Having Imidazolium Moieties"
Keiya Yamamoto and Ken Sakai
Manuscript in preparation.

Other Publications

1. "Near-Infrared Light-Driven Hydrogen Evolution from Water Using a Polypyridyl Triruthenium Photosensitizer"
   Yutaro Tsuji, Keiya Yamamoto, Kosei Yamauchi and Ken Sakai
   Angew. Chem. Int. Ed., **2018**, *57*, 208-212.